ABSTRACT

Title of Dissertation: MATHEMATICAL MODELS AND NOVEL BIOMARKERS TOWARD OPTIMIZATION OF BURN INJURY RESUSCITATION

Ghazal Arabidarrehdor, Doctor of Philosophy, 2022

Dissertation directed by: Dr. Jin-Oh Hahn, Associate Professor, Department of Mechanical Engineering

Extensive burn injury is not only devastating but also a significant challenge for healthcare providers. Following a chain of inflammatory responses post-burn, significant amounts of plasma shift from the vascular compartment into the tissues, simultaneously posing the risks of hypovolemic shock and edema. Standard burn resuscitation protocols aim to replace the lost blood volume while not exacerbating the edema through hourly-titrated intravenous fluid infusion. Due to the significant variability in treatment efficacy, there is a substantial ongoing effort to optimize and individualize the burn resuscitation protocols. In this work, we aim to contribute to this effort by (i) developing a platform for the virtual evaluation of burn resuscitation protocols and (ii) identifying biomarkers to guide fluid resuscitation effectively.

The first part of this work presents a mathematical model of burn injury and resuscitation, which can be used for the development and non-clinical testing of burn resuscitation protocols and algorithms, as well as to garner knowledge and intuition into this complex pathophysiology. Our mathematical model consists of a multi-compartmental model of blood volume kinetics, a hybrid

mechanistic-phenomenological model of kidney function, and novel lumped-parameter models of burn-induced perturbations in volume kinetics and renal function. We examined our mathematical model's prediction accuracy and reliability using a rich dataset from 16 sheep with extensive burn injuries and clinical data from 233 real-world burn patients.

The second part of this work presents the expansion of the mathematical model to incorporate the cardiovascular and renin-angiotensin-aldosterone systems, as well as detailed descriptions of the kidney's mechanisms, particularly regarding its blood volume and blood pressure regulation roles. This expansion was motivated by the importance of cardiovascular monitoring in the critical care of burn injury patients. We trained and validated the expanded mathematical model for three species: nine sheep subjects and 15 swine subjects with rich cardiovascular and volume kinetics data, and 233 human subjects with demographic and urinary output (UO) data. To the best of our knowledge, our mathematical model may be the first of its kind which is extensively validated for use as a digital twin to replicate realistic burn patients and replace standard large animal pre-clinical testing of burn resuscitation protocols.

The third part of this work presents the identification of biomarkers capable of guiding, optimizing, and individualizing burn resuscitation. The UO, the most common endpoint used to titrate burn resuscitation fluid doses, has many limitations as a single variable. Hence, this work aimed to find convenient and reliable biomarkers from arterial blood pressure (ABP) waveform to complement UO in guiding burn resuscitation. Pulse pressure variation (PPV), systolic pressure variation (SPV), and stroke volume variation (SVV) are dynamic indices derived from ABP that have shown promise in hemorrhage resuscitation but are not investigated for different resuscitation paradigms for burn injury. We observed the longitudinal behavior of PPV, SPV, and SVV for 21 porcine subjects with 40% burn injury, which were each either under-resuscitated, adequately resuscitated,

or deliberately over-resuscitated. We investigated the features' potential in tracking reference cardiac output (CO) and stroke volume (SV) via linear regression and correlation analysis. PPV, SPV, and SVV showed plausible and statistically different trends for different paradigms. While they performed just as well as UO in tracking CO and SV, their inherent advantage of being available in real-time and their disagreement with UO in determining the subject status suggest that they may potentially complement UO in the hemodynamic assessment of burn patients.

MATHEMATICAL MODELS AND NOVEL BIOMARKERS TOWARD OPTIMIZATION OF BURN INJURY RESUSCITATION

by

Ghazal ArabiDarrehDor

Dissertation submitted to the Faculty of the Graduate School of the
University of Maryland, College Park, in partial fulfillment
of the requirements for the degree of
Doctor of Philosophy
2022

Advisory Committee:
Professor Jin-Oh Hahn, Chair
Professor Daniel Butts, Dean's Representative
Professor Nikhil Chopra
Professor Hosam Fathy
Professor Yancy Diaz-Mercado
Professor Eleonora Tubaldi

Dedication

To my sister, my little star, Soha, and to my mom, Rosa. You're the meaning behind everything I do.

Acknowledgements

There are so many people that have made this work possible. First and foremost, I am eternally thankful to my advisor, Professor Jin-Oh Hahn, for his continued support, trust, understanding, and inspiration. I have learned so much from his enthusiasm for research, integrity, sense of responsibility, and openness to new ideas. His guidance was critical to shaping my academic mind, the becoming of this work, and perhaps every other work I will do in the future. It was an absolute honor to be his research assistant.

I'm grateful to Professor George Kramer for providing priceless experimental and clinical data that were pivotal to this work, as well as his kindness, eagerness to help, and offering clinical insight that I could not find in any other resources. I equally thank Professor David Burmeister for giving me the opportunity to work on the exciting biomarker project and providing the experimental dataset that made it possible.

I would also like to thank Professor Daniel Butts, Professor Nikhil Chopra, Professor Hosam Fathy, Professor Yancy Diaz-Mercado, and Professor Eleonora Tubaldi for their time, insightful comments, and thought-provoking feedback. It was an honor to have you on my committee.

My deepest thanks to my intelligent and hard-working lab mates who were always helpful and supportive: Azin, Ali, Mohammad, Ramin, Yekanth, Richard, Drew, Jessie, Peyman, Zahra, Weidi, Xin, Yuanyuan, Peyman, and Parham.

I gratefully acknowledge the funding sources that supported this work and made it possible. My research was funded by the U.S. Army SBIR Program under Grant W81XWH-16-C-0179, the Congressionally Directed Medical Research Programs under Grant W81XWH-19-1-0322, the U.S. National Science Foundation CAREER Award under Grant 1748762, and by CDMRP under Grants W81XWH-19-2-0004 and W81XWH-19-1-0322.

I cannot even begin to thank my boyfriend, Ramin, for taking care of me, motivating me, and supporting me every step of the way for the past five years. I couldn't have done it without you. And I want to express my heartfelt thanks to my best friend, Farnoosh, for her love, support, and for what I can only describe as everything.

Finally, no words could describe how thankful I am to my amazing family and how lucky I am to have them by my side, even from thousands of miles away. My superhero of a mother, Rosa. My amazing, funny sisters, Asal, Soha, and Hana, and my patient, kind brother, Masoud. Thank you for your unconditional love and for believing in me more than I ever could. I look forward to being right next to you and making you happy every single day of my life.

List of Figures

List of Tables

Chapter 1: An Introduction to Burn Resuscitation Challenges, and the History of Mathematical Modeling of Burn Injury and Resuscitation

1.1 Background: What is Burn Resuscitation

Burn injury is a leading cause of unintentional injury and death in the United States. According to a recent fact sheet from the American Burn Association, burn injury is the 8th leading cause of death in adults >65 years old, 3rd in children 5-9 years old, and 5th in children 1-4 years old [1]. Each year, there are nearly 500,000 burn injury incidences only across the United States, among which 40,000 are hospitalized. While severe burn injury is devastating, immensely painful, and affects the patients for a very long time, it is also a major clinical challenge for healthcare providers.

Everyone is familiar with the dermal effects of burn injury, and when they see the term "burn treatment", most people are automatically reminded of wound healing and infection prevention. While the importance of attending to wounds cannot be emphasized enough, the first 24-48 hours post-injury is also about keeping the patient alive and stabilizing them for potential surgery. This is done by "fluid resuscitation", which, simply put, means intravenous fluid infusion.

To understand why, we have to know what happens to the body on a systemic level: severe burn injury, i.e., thermal injury affecting more than 20% of total body surface (TBSA), results in intense inflammatory responses in the body that lead to increased

leakage of intravascular water and protein into the tissues. This is detrimental on two levels: first, the depletion of water and protein from the intravascular space compromises the circulation to and from organs, and second, the excessive fluid in the tissues causes massive edema. If not treated, this imbalance engenders fatal consequences such as hypovolemic shock, ischemia, multiple organ failure, and generalized edema [2], [3]. Fluid resuscitation, or intravenous infusion, is done to replace the lost plasma volume in the intravascular compartment, but since there is inflammation, the fluid dose must be chosen such that it does not exacerbate the edema. The majority of burn patients treated in burn centers survive, but many of them suffer from complications [4], [5].

1.2 Problem Statement: Why is Burn Resuscitation Challenging?

As briefly stated above, the gold-standard treatment for burn injury patients involves intravenous fluid resuscitation with the goal of replacing the lost intravascular fluid and averting hypovolemia. The fluid types used for this purpose mainly include crystalloids and colloids. Crystalloids contain small molecules such as electrolytes and might be isotonic (in electrolyte balance with plasma, e.g., similar sodium concentration), or hypertonic (higher tonicity). Colloids contain larger molecules such as albumin (protein) and might be iso-oncotic (same protein concentration as plasma) or hyper-oncotic (higher protein concentration).

There is a complete lack of consensus over the optimal burn resuscitation strategy in terms of the timing, amount, and type of fluids to be administered [6]–[9]. Among the most famous resuscitation algorithms are Evans formula, Brooke (and Modified Brooke) formula, and the most widely used, Parkland (and Modified Parkland)

formula. These formulas suggest the amount and type of fluid to be given to the patient as adjusted by the patient's weight (W) and TBSA. For instance, the Modified Parkland formula suggests using 4 ml/kg/%TBSA of Lactated Ringer's (LR, an isotonic crystalloid) in the first 24 hours post-injury, where half of this amount is to be given during the first 8 hours, and half during the remaining 16 hours. For a patient of 70 kg weight and 40% TBSA, this translates into an infusion dose of 700 ml/hr in the first 8 hours post-injury, and 350 ml/hr of infusion in the next 16 hours.

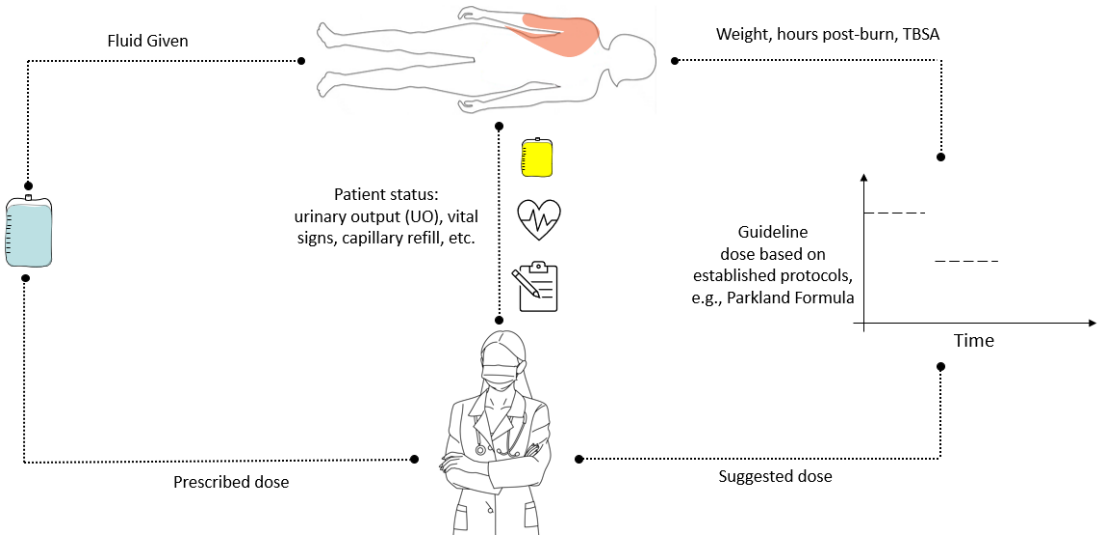

Fig. 1.1: the gold-standard protocol for burn resuscitation starts by a generic suggestion from established formulas, and frequently titrated based on patient responses.

It should be emphasized that the existing resuscitation protocols exhibit a large variability in treatment efficacy, due to many factors such as the inter-patient differences in response to burn injury and resuscitation as well as the incomplete knowledge of the pathophysiology underlying burn injury. Hence, burn resuscitation protocols must be individualized, often by way of choosing one or multiple clinical end-points and adjusting the infusion dose around achieving them. That is why in

today's practice, burn resuscitation often starts with an established burn resuscitation protocol such as Parkland formula, using it merely as a guideline, but is frequently titrated in an ad-hoc fashion to the clinical end-points of choice. The most common end-point in this context is the urinary output (UO) response as a proxy for intravascular replacement, with the end-point of maintaining the UO in the therapeutic target range of 30-50 ml/hr or 0.5-1.0 ml/kg·hr [10], [11]. This process is illustrated in Fig. 1.1.

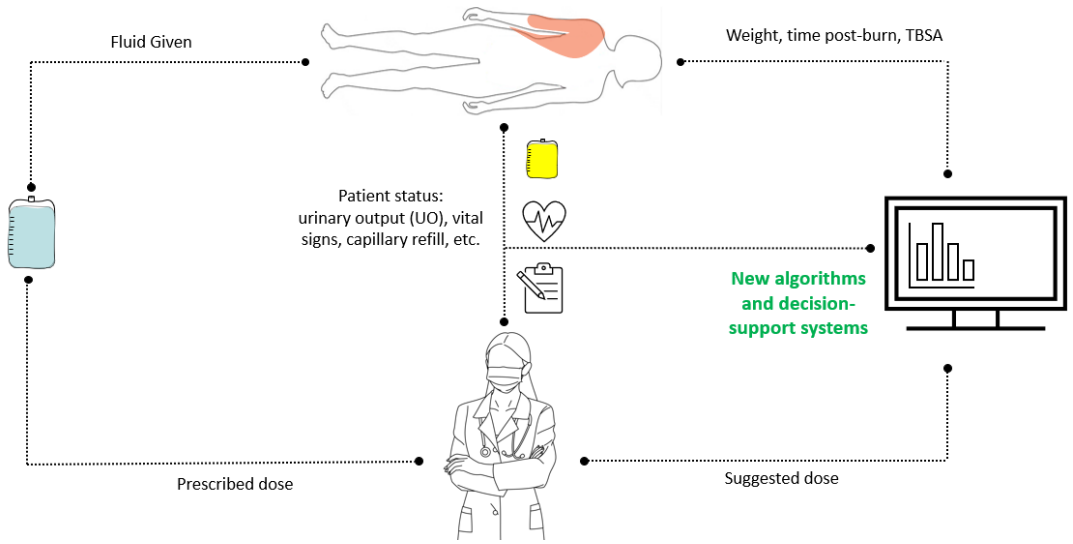

Fig. 1.2: there is an ongoing effort to design new algorithms and decision support systems to optimize and individualize burn resuscitation.

Starting the use of these protocols over the past decades reduced the incidence of burn shock, mortality rate, early post-burn renal failure, and tissue loss [12], but numerous resuscitation complications emerged along with those benefits. Studies show that burn units tend to conservatively over-resuscitate patients with an excessive amount of fluid up to twice as much as recommended, as explained famously by Basil Pruitt "...in the apparent belief that if some fluid is good, lots of fluid will be even better'' [12], [13]. On the contrary, this excessive fluid is catastrophic, since it exacerbates edema and

exposes the patients to an elevated risk of side effects, e.g., pulmonary edema, limb and abdominal compartment syndrome, necrosis, and death, due to the accumulation of resuscitation fluid (known as “fluid creep”) [14], [15]. In general, trying to manually titrate the doses based on patient response is a difficult task that requires a lot of time, expertise, and training, which is not always available.

Hence, there is an ongoing effort to develop new algorithms that optimize as well as individualize burn resuscitation regimens to best maintain organ functions while minimizing adverse complications and also to embed them in decision-support systems that make decision-making easier, [12], [16]–[18] (Fig. 1.2).

Development such burn resuscitation protocols and devices is a challenging task in three aspects:

(i) Design: there are two major obstacles when designing algorithms that could effectively individualize burn resuscitation protocols: (1) there are still gaps in the burn pathophysiology knowledge which must be the basis of developing effective treatment protocols. One example is the significant difference in mortality rate between patients of different genders, ages, and comorbidities, the cause of which are still not fully unraveled. And (2), to titrate the fluid dose given to patients, we need reliable, multifaceted end-points (aka biomarkers) to guide the resuscitation. UO, which is currently the most commonly used end-point, has well-known limitations, and the search for other biomarkers that complement UO continues.

(ii) Evaluation: needless to say, each protocol must be thoroughly evaluated before being used, and it is unethical to test a new treatment protocol with

unproven efficacy and safety in critically ill burn patients. Additionally, large-scale pre-clinical tests on large mammals, such as sheep and pigs, pose financial and ethical costs.

(iii) Practice: as stated above, finding the optimal fluid doses is a difficult task that requires expertise and training, and training is hampered by the small number of burn injuries compared to other forms of trauma.

1.3 Proposed Research: How Do We Contribute?

In this work, we contribute to this effort via two approaches:

1- Mathematical modeling of burn injury and resuscitation

In recent years, both the U.S. and European regulatory agencies have expressed interest in using mathematical models of physiological systems as powerful non-clinical tools for developing and testing clinical therapies [19]–[22], AKA in-silico testing. A mathematical model that can replicate physiological responses to burn injury and resuscitation in diverse burn patients, can serve as an attractive basis to perform non-clinical testing of emerging burn resuscitation protocols as a medical digital twin. In addition to their use for in-silico testing, mathematical models could be valuable tools to deepen our understanding of a physiological phenomenon and have been shown to improve learning when used for educational purposes for medical experts and healthcare providers [23], [24]. Similarly, a reliable mathematical model of burn injury and resuscitation has the potential to be used to train and educate the healthcare providers by visualizing and solidifying the current knowledge around the pathophysiology of burn injury and predicting the standard responses to different levels

of burn severities and resuscitation protocols. This is a significant advantage considering the complicated decisions that burn injury healthcare providers have to make in real-time, i.e., regulating the infusion rates to maintain perfusion while avoiding under- or over- resuscitation. Mathematical models are also being increasingly used to make discoveries and resolve mysteries in biology [25], [26]. A credible and interpretable mathematical model of burn injury could provide new insight into the complex phenomenon of burn pathophysiology by predicting what seemingly happens to the variables that are immeasurable or rarely measured. Thus, it can facilitate the design, evaluation, and implementation (practice) of new resuscitation protocols and devices. Chapters 1-5 of this dissertation are dedicated to this effort.

2- In the second part of this work, we further contribute to facilitating the design of these protocols by finding novel biomarkers that could help determine the status and fluid needs of patients. Chapter 6 of this dissertation is dedicated to this effort.

1.3 Previous Work: Our Criteria, and Current Gaps in Brun Modeling

To be relevant for knowledge expansion, evaluation, and training purposes, a mathematical model must be equipped with a number of desirable characteristics. First, the model must predict the volume kinetics of the body, i.e., the water and protein distribution and dynamics throughout the body, particularly plasma volume (PV), to be able to report the hemodynamic status of the patient in response to burn injury and resuscitation. It is also necessary to be able to predict the UO, since most burn

resuscitation algorithms receive UO as the biological feedback of the patients to update the fluid recommendations. Second, mechanistic transparency is needed for straightforward interpretation of the model and its results. Third, the model needs to be parsimonious so that it is suitable for real-time computation and virtual patient generation. Finally, the model must be rigorously validated by a diverse and large real-world dataset to make sure the virtual patients generated by the model are good representatives of physical patients.

Prior work on mathematical modeling of burn injury and resuscitation is primarily limited to three groups.

Arturson et al. [27]–[29] developed an extensive and complex phenomenological model containing modules describing the systemic circulation, microcirculation of water and protein, the dynamics of a number of electrolytes in the extracellular and intracellular components, the renal function and the regulation of relevant hormones. The states of the model such as the volume and protein distributions throughout the body are described using ordinary differential equations (ODEs). Most of the functions describing the model, particularly the time-dependent burn-induced perturbations on microcirculation, are statistical derivations based on data from previous studies. The parameters of the model were estimated or guessed at using datasets collected from a small number of burn patients (n=4).

Roa et al. [30]–[32] developed a hybrid mechanistic-phenomenological model with modules similar to that of Arturson et al., except for hormone regulation which is lacking in this model. They use the dynamic systems approach, i.e., causal diagram and Forrester diagram construction. Similar to Arturson, they use fixed, statistically-

derived functions to describe the important burn-induced perturbations in microcirculation. They used a relatively large dataset of burn patients (n=90) to estimate the unknown parameter values of their model.

Bert et al. [33]–[37] also developed a hybrid mechanistic-phenomenological model, weighing more on the mechanistic side, describing the microcirculation of water and protein between the intravascular and interstitial compartments, using ODEs to estimate the states of the model and tunable, time-dependent functions to describe the burn-induced perturbations. They estimated the parameters using datasets collected from rats, and a relatively large human dataset (n=105).

These models provide very good insights into the complicated physiology and pathophysiology associated with burn injury and resuscitation. However, they are not yet ideal for the purposes mentioned above for at least three reasons. First, a subset of these mathematical models cannot predict UO [33]-[37]. Such a limitation directly disqualifies a mathematical model in the development and testing of burn resuscitation regimen based on UO feedback. Second, the ability of the existing mathematical models to predict PV and UO was evaluated or reported in a prohibitively small number of patients [27]-[32] or only at the population level [33]-[37]. In addition, the ability of these mathematical models to predict responses other than PV and UO are not reported in detail. Such lack of validation evidence weakens the reliability of these mathematical models as a basis for reproducing individualized hemodynamic and renal responses of diverse burn patients. Third, some mathematical models (especially those reported earlier) [27]-[32] do not reflect up-to-date knowledge of burn-related physiology and pathophysiology gained in recent experimental and clinical

investigations, regarding in particular the burn-induced perturbations in volume kinetics, kidney function, lymphatic flow, and tissue pressure-volume relationships, which will elaborate on later [2], [38], [39].

Closing these gaps may lead us to an enhanced mathematical model of burn injury and resuscitation ideally suited to the development and testing of emerging burn resuscitation protocols and algorithms, as well as to the expansion of our knowledge of burn pathophysiology and its use for training.

1.4 An Introduction to Proposed Models and the Following Chapters

In chapter 2, we present a mathematical model of blood volume kinetics and renal function in response to burn injury and resuscitation, which is applicable to the development and non-clinical testing of burn resuscitation protocols and algorithms. This mathematical model (which we call our original model) consists of an established multi-compartmental model of BV kinetics, a hybrid mechanistic-phenomenological model of renal function, and novel lumped-parameter models of burn-induced perturbations in volume kinetics and renal function equipped with contemporary knowledge on burn-related physiology and pathophysiology. In chapter 3, we examined the efficacy of our mathematical model in predicting volume kinetic and renal function responses to burn injury and resuscitation using the dataset collected from 16 sheep [40]. Further we moved on to develop, extensively validate, and analyze our model for real-world burn patients in chapter 4. By leveraging clinical datasets collected from 233 real burn patients receiving resuscitation, we modified the mathematical model so that it is suited to computer-aided in-human burn resuscitation

trials and knowledge expansion, by expanding our prior work and utilizing a systematic parametric sensitivity analysis and regularization [41]. We investigated the validity of the mathematical model by testing its physiological plausibility in a dedicated test dataset. Using the validated mathematical model, we examined possible mechanisms responsible for the cohort-dependent differences in burn pathophysiology by comparing the mathematical models fitted exclusively to younger versus older patients, female versus male patients, and patients with versus without inhalational injury.

In chapter five, we expanded our mathematical model by adding a cardiovascular model, a detailed renal function model which was more transparent than the original renal function model, and a renin-angiotensin-aldosterone model. This expansion enabled the model to predict clinically significant variables such as blood pressure and cardiac output, and also in-silico testing of algorithms that are designed based on these vital signs. We validated the expanded model in nine sheep, 15 pig subjects, and 233 human subjects. To the best of our knowledge, our mathematical model may be the first mathematical model extensively validated for use as a digital twin of real-world burn patients and large mammal pre-clinical testing.

Chapter six is dedicated to an independent effort to find biomarkers hidden in the arterial blood pressure waveform that could be used to guide fluid resuscitation for burn injury.

Chapter 2: Model Development: Volume Kinetics, Kidney Function, and Burn Perturbations

2.1 Background and Model Schematics

The mathematical model consists of (i) volume kinetics to replicate water volume and protein concentration dynamics in the intravascular and the tissue compartments ("Volume Kinetics" in Fig. 2.1(a); see section 2.2), (ii) kidney functions to replicate UO response to changes in intravascular water and protein volumes ("Kidneys" in Fig. 2.1(a); see section 2.3), and (iii) transient perturbations in volume kinetics induced by burn as a chain of biochemical, molecular, and mechanical events ("Burn Perturbations to Volume Kinetics" in Fig. 2.1(b); see section 2.4).

The volume kinetics was represented using a three-compartmental model with intravascular space (including arterial and venous vessels, shown as "Plasma" in Fig. 2.1), intact tissues, and burnt tissues as separate compartments. These compartments describe the volumes of water (V_P, V_{IT}, V_{BT}; whose dynamics is governed by Eq. (2.1)) and protein therein (A_P, A_{IT}, A_{BT}; whose dynamics is governed by Eq. (2.2)) as functions of time. It was assumed that albumin serves as the surrogate of all the protein contributing to capillary filtration and colloid oncotic balance [37]. As shown in Fig. 2.1, the change in these volumes are dictated by (i) inter-compartmental flows of the lymphatic drainage (water J_L and protein Q_L; Eq. (2.5)-(2.6)) and capillary filtration (J_C and Q_C; Eq. (2.3) and Eq. (2.7)); (ii) external inputs representing the gain via burn

resuscitation (J_F and Q_F); and (iii) outputs representing the kidneys' net filtration and reabsorption of renal plasma flow (i.e., UO J_U; Eq. (2.12) and Eq. (2.27)), as well as burn-induced evaporation (J_{EV}; Eq. (2.32)) and exudation (J_{EX} and Q_{EX}; Eq. (2.33)). The kidney function is represented by a lumped-parameter model developed which includes a hybrid combination of first-principles and phenomenological elements that describe UO control governed by the kidneys, including the glomerular filtration rate (GFR; J_{GFR} in Fig. 2.1 and Eq. (2.13)-(2.19)) modulated by the Starling forces due to the change in the intravascular water and protein volumes (i.e., plasma volume), the reabsorption by the glomerulotubular balance ($J_{RR,GT}$ in Fig. 2.1 and Eq. (2.20)-(2.21)), and the reabsorption and sodium osmosis modulated by the Antidiuretic hormone ($J_{RR,ADH}$, ADH in Fig. 2.1 and Eq. (2.22)-(2.26)). The transient perturbations in volume kinetics and kidney function triggered by burn injury were represented by an array of time-varying phenomenological models acting on various parameters and variables in the mathematical model of volume kinetics to replicate local and systemic pathophysiological changes caused by burn injury, including (i) partial destruction of capillaries in burnt tissues (a in Fig. 2.1; Eq. (2.34)-(2.35)), (ii) denaturation of protein in burnt tissues (b in Fig. 2.1; Eq. (2.29)), (iii) transient negative hydrostatic pressure in burnt tissues (c in Fig. 2.1; Eq. (2.30)), (iv) increased dermal fluid loss (d in Fig. 2.1; Eq. (2.32)-(2.33)), (v) time-dependent changes in capillary filtration and albumin permeability (e in Fig. 2.1; Eq. (2.34)-(2.36)), and (vi) vasodilation (f in Fig. 2.1; Eq. 2.37)). The disruption of the kidney function was the consequence of the perturbations occurring in volume kinetics as governed by Eq. (2.12)-(2.27).

We should note that since burn resuscitation is usually performed in the first 24-48 hours post-burn, and the status of patients is assessed hourly, we have only considered the relevant mechanisms that function in our target time-scale of “hours” and compatible with our time step of 6 minutes. Any mechanism that is either too fast (acts and settles withing seconds, such as the CNS), or too slow (effective only after days, such as some hormonal mechanisms) is not considered here.

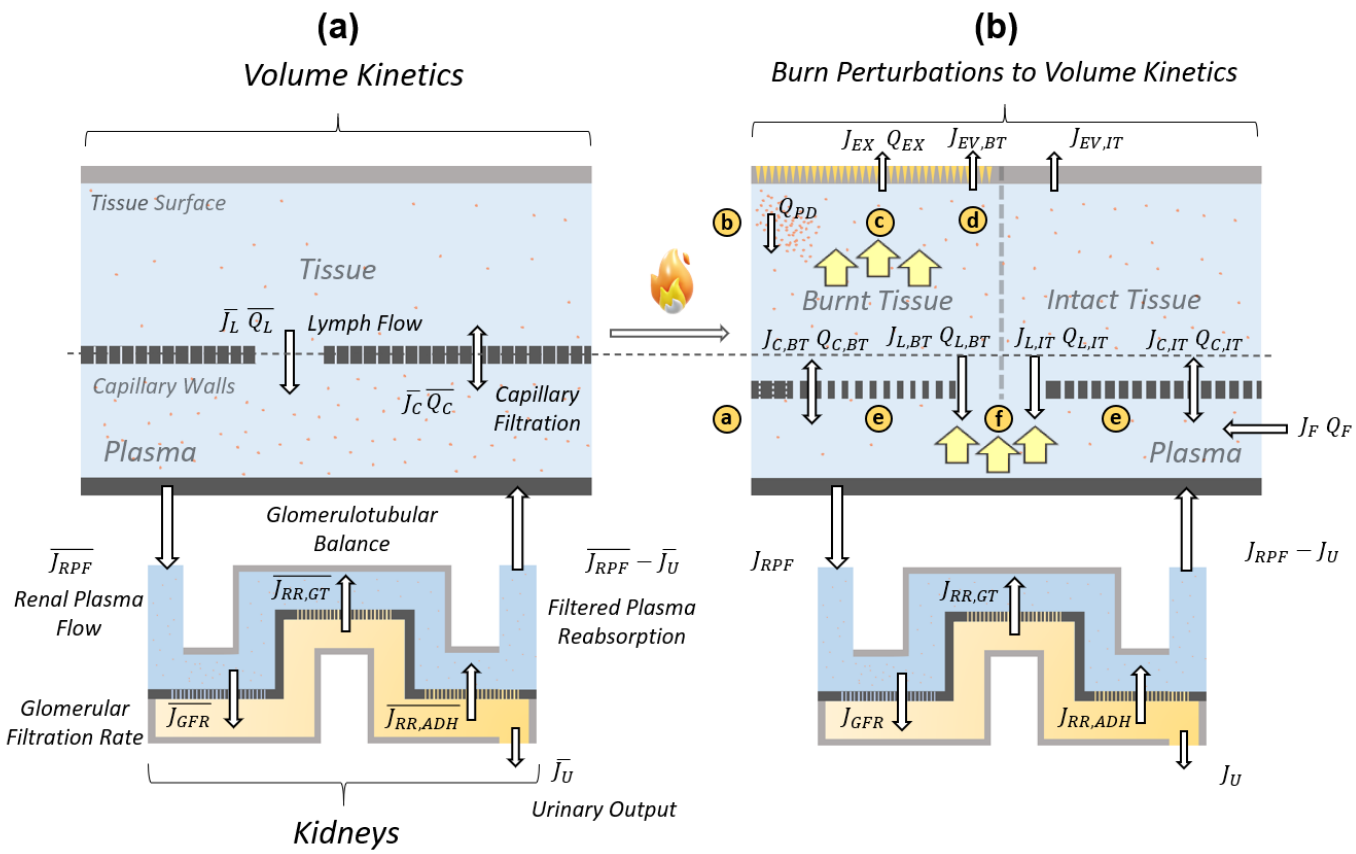

Fig. 2.1: Mathematical model capable of predicting volume kinetic and kidney function responses to burn injury and resuscitation. Fig. 2.1(a) shows normal state, where the water (blue background) and protein (pink dots) balance between the intravascular compartment ("Plasma") and the tissue is preserved by the capillary filtration through the capillary pores (thin rectangles in the capillary wall) and lymph flow. Plasma is filtered by the renal plasma flow into the kidney where its filtration and reabsorption are being controlled by way of the renal regulatory mechanisms including the glomerulotubular balance and the Antidiuretic hormone. Upon the onset of burn injury, the water and protein volumes in the plasma decrease, while tissue compartment is divided into intact and burnt tissue compartments associated with water and protein content higher than normal state ("Burnt Tissue" and "Intact Tissue") (Fig 2.1(b)). J: water flow. Q: albumin flow. Subscripts: C (capillary filtration); L (lymph flow); F (fluid infusion); U (UO); RPF (renal plasma flow); GFR (glomerular filtration rate); RR,GT (reabsorption rate by glomerulotubular balance); RR,ADH (reabsorption rate by Antidiuretic hormone); EX (exudation); EV (evaporation); PD (protein denaturation); BT (burnt tissues); IT (intact tissues). The yellow circles represent the perturbations that lead to the redistribution of water and protein. a: Partial destruction of capillaries in burnt tissues (shown as occluded capillary pores). b: Denaturation of protein in burnt tissues. c Transient negative hydrostatic pressure in burnt tissues, which draws water into the burnt tissues. d: Increased dermal fluid loss. e: Time-varying changes in capillary filtration and albumin permeability (shown as enlarged capillary pores). [f]: Vasodilation, which pushes water out of plasma. $\overline{X}$ represents X in normal (pre-burn) state.

2.2 Volume Kinetics

The volume kinetics (VK) is the backbone of the model and describes the water and distribution in the intravascular compartment because we want to know how much fluid is lost/replaced, as well as in the burnt and intact tissues, because we want predictions of potential edema and fluid accumulation. We also need the protein distribution in these compartments, because protein concentration plays a major role in water balance and filtration in the body.

The VK was represented by a classical multi-compartmental model consisting of vasculature, intact tissues, and burnt tissues. It describes the water and protein balance in these compartments and homeostasis via capillary filtration and lymphatic flow as well as water gain (e.g., burn resuscitation) and loss (e.g., UO, evaporation, and exudation). The water and protein balance in each compartment was formulated based on the mass conservation principle:

$$\frac{d(V_P)}{dt} = -J_{C,BT} - J_{C,IT} + J_{L,BT} + J_{L,IT} + J_F - J_U, \tag{2.1a}$$

$$\frac{d(V_{BT})}{dt} = J_{C,BT} - J_{L,BT} - J_{EX} - J_{EV,BT}, \tag{2.1b}$$

$$\frac{d(V_{IT})}{dt} = J_{C,IT} - J_{L,IT} - J_{EV,IT}, \tag{2.1c}$$

$$\frac{d(A_P)}{dt} = -Q_{C,BT} - Q_{C,IT} + Q_{L,BT} + Q_{L,IT} + Q_F, \tag{2.2a}$$

$$\frac{d(A_{BT})}{dt} = Q_{C,BT} - Q_{L,BT} - Q_{EX} + Q_{PD}, \tag{2.2b}$$

$$\frac{d(A_{IT})}{dt} = Q_{C,IT} - Q_{L,IT}, \tag{2.2c}$$

where V is water volume, A is albumin content, J is water flow, and Q is albumin flow. The subscripts C, L, F, U, EV, EX, and PD denote capillary filtration, lymphatic flow, fluid infusion, UO, evaporation, exudation, and protein influx due to burn-induced denaturation (see section 2.3), respectively, while the subscripts P, BT, IT denote plasma, burnt tissues, and intact tissues, respectively. Note that we assumed that albumin content represents the protein content similarly to prior work [36], [37].

The capillary filtration of water across the capillary wall was expressed using the Starling equation:

$$J_{C,X} = K_{C,X}[P_C - P_X - \sigma_X(\pi_C - \pi_X)], \tag{2.3}$$

where $X \in \{BT, IT\}$, P_C and P_X are the capillary and tissue hydrostatic pressures, π_C and π_X are the plasma and tissue colloid oncotic pressures associated with burnt, ($X = BT$) and intact ($X = IT$) tissues, respectively. $K_{C,X}$ is the capillary filtration coefficient and represents the surface area available for filtration, and σ_X is the albumin reflection coefficient representing the level of impermeability of the capillary wall to albumin (see Eq. (2.34)). This widely-used equation is based on the fact that the filtration from a compartment (e.g., plasma) across a semipermeable membrane (e.g., capillary wall), into another compartment (e.g., tissue), has a driving force that depends on the pressure gradient between the sides. While the capillary hydrostatic pressure pushes the fluid out, the tissue hydrostatic pressure resists the inward flow. On the other hand, the plasma colloid oncotic pressure promotes the retention of water in the plasma, while the tissue colloid oncotic pressure draws the fluid inward. It is important to note that this filtration is bi-directional, but under normal circumstances the net water filtration

direction is from plasma into the tissues, and therefore we define this direction as positive, and the flow from tissue to plasma as negative.

The colloid oncotic pressure was expressed as a linear function of albumin concentration [37]:

$$\pi_C = C_O[A]_P,\ \pi_X = C_O[A]_X,\ [A]_P = \frac{A_P}{V_P},\ [A]_X = \frac{A_X}{V_X} \tag{2.4}$$

where C_O is a constant relating albumin concentration to colloid oncotic pressure, and $[A]_P$ and $[A]_X$ are the plasma and tissue albumin concentrations, respectively.

The lymphatic flow normally collects the excess fluid in the tissues (from capillary filtration) and returns it back to the circulation. It was expressed by a phenomenological model in the form of a sigmoidal curve:

$$J_{L,X} = \frac{\bar{J}_{L,X}}{C_L + (1 - C_L)e^{-S_L(P_X - \bar{P}_X)}}, \tag{2.5}$$

where $\bar{J}_{L,X}$ is the nominal lymphatic flow at the nominal tissue hydrostatic pressure of $\bar{P}_X$, and C_L and S_L are constants representing the inverse of the maximal degree of increase in the lymphatic flow and its sensitivity to the change in the tissue hydrostatic pressure, respectively. Note that this phenomenological model can reproduce the real-world behavior of the lymphatic flow despite its simplicity, i.e.,: (i) it primarily depends on the tissue hydrostatic pressure [42]; (ii) it is proportional to the tissue hydrostatic pressure but eventually saturates; and (iii) it reduces to zero at very low tissue hydrostatic pressure [43]. The albumin transport associated with the lymphatic flow from each interstitial compartment depends both on the lymphatic flow and the albumin concentration in the corresponding tissues:

$$Q_{L,X} = J_{L,X}[A]_X. \tag{2.6}$$

The albumin transport across the capillary wall was expressed based on the coupled diffusion-convection equation [37], [44]:

$$Q_{C,X} = J_{C,X}(1-\sigma_X)\left\{\frac{[A]_P - [A]_X e^{-\frac{(1-\sigma_X)J_{C,X}}{PS_X}}}{1-e^{-\frac{(1-\sigma_X)J_{C,X}}{PS_X}}}\right\}, \tag{2.7}$$

where $X \in \{BT, IT\}$, and PS is the permeability-surface area coefficient, representing the area available for albumin to cross the capillary wall.

The evaporation flow ($J_{EV,X}$, $X \in \{BT, IT\}$ in Eq. (2.1b)-(2.1c)) and the exudation flow (J_{EX} in Eq. (2.1b) and Q_{EX} in Eq. (2.2b)) were expressed as phenomenological models based on prior work (see Section 2.3). The burn resuscitation (J_F in Eq. (2.1a) and Q_F in Eq. (2.2a)) is the input provided to the mathematical model.

The capillary (P_C) and tissue (P_X) hydrostatic pressures in Eq. (2.3) and Eq. (2.5) were expressed as functions of the corresponding water volumes (V_P and V_X). We assumed a linear phenomenological relationship between P_C and V_P:

$$P_C = \bar{P}_C + E_C(V_P - \bar{V}_P), \tag{2.8}$$

where $\bar{P}_C$ is the nominal capillary hydrostatic pressure associated with the nominal PV $\bar{V}_P$, and E_C is the capillary elastance. We used a nonlinear mechanistic hydrostatic pressure-volume relationship associated with the interstitial tissues at the microscopic level developed by Øien and Wiig [45], and extended it for use with macroscopic measurements. The original model by Øien and Wiig expresses the tissue hydrostatic pressure as a function of the radius R of the spherical glycosaminoglycans (GAG's) therein:

$$P_X = -\frac{\alpha}{R} + \gamma, \tag{2.9}$$

where α and γ are constant coefficients representing the impact of electrostatic pressure and tissue tension pressure [45] on P_X and

$$R = R(y_X) = \hat{R}\left[1 - (1-\beta)\left(\frac{y_X - \hat{y}}{\check{y} - \hat{y}}\right)\right]^n, \tag{2.10}$$

Expressing R as a function of y_X, the half-thickness of the extracellular matrix building block (which is a measure of hydration in the tissue X at the microscopic level), $\hat{y}$ and $\check{y}$ are the maximum and minimum values of y_X, $\hat{R}$ is the maximum value of R, β is the ratio between maximum R and nominal R, and n is an exponent describing the GAG response to hydration [45]. We extended Eq. (2.9)-(2.10) to compute P_X from macroscopic rather than microscopic (i.e., y_X) measurement by assuming that y_X is proportional to the water volume in the tissues:

$$y_X = 0.75\left(1 + \overline{W}_X \frac{V_X}{\overline{V}_X}\right), \tag{2.11}$$

where $\overline{W}_X$ is the nominal hydration level defined as the ratio of the water volume in X and its dry weight [46], and the coefficient 0.75 was derived from the assumptions used in prior work of Øien and Wiig [46].

2.3 Kidney Function

As blood circulates in the body, the renal plasma flow (J_{RPF}) flows into the kidneys for its perfusion as well as to be filtered. The glomerular filtration rate (J_{GFR}) is the fraction of J_{RPF} that is filtered into the Bowman's capsule to flow along the nephron tubules, the majority of which is reabsorbed back into the circulation, cleared from waste material. Fig. 2.2 shows the schematic of the kidney function model.

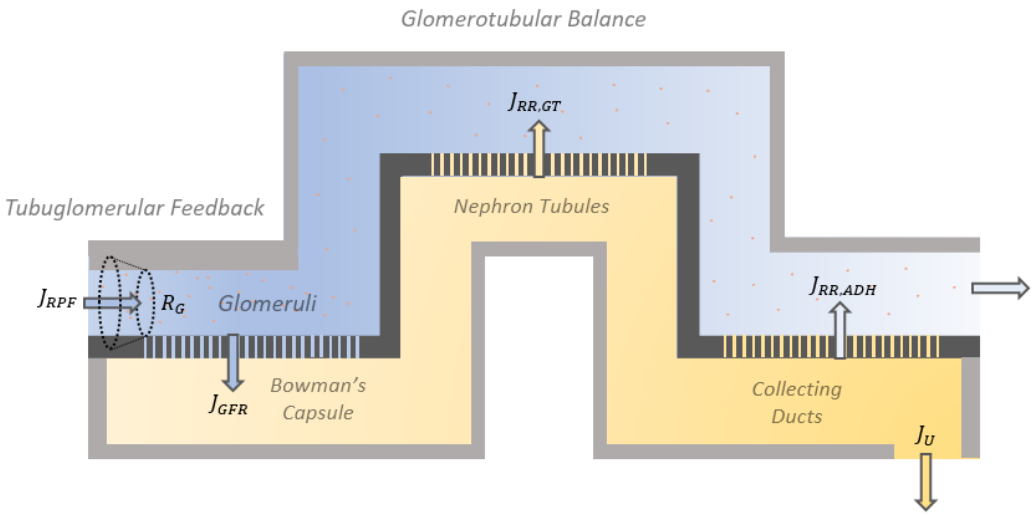

Fig. 2.2: Schematic of renal function model. J_{RPF}: renal plasma flow. J_{GFR}: glomerular filtration rate (GFR). $J_{RR,GT}$: reabsorption rate due to modulation of glomerulotubular balance. $J_{RR,ADH}$: reabsorption rate due to modulation of ADH. J_U: UO. R_G: hypothetical glomerular resistance modulating J_{RPF} against perturbations in plasma volume.

UO is given by the difference between the GFR (J_{GFR}) and the reabsorption rate (RR; J_{RR}):

$$J_U = J_{GFR} - J_{RR}. \tag{2.12}$$

This function was represented by a novel lumped-parameter, hybrid mechanistic-phenomenological model we developed in this work (Fig. 2.2). It consists of hybrid mechanistic-phenomenological components to describe UO control by the kidneys, including the glomerular filtration rate (see section 2.3.1.) modulated by the Starling forces in response to the change in BV as well as the reabsorption and sodium osmosis (see section 2.3.2.) modulated by the antidiuretic hormone (ADH).

2.3.1 Glomerular Filtration Rate

GFR is dictated by the Starling forces:

$$J_{GFR} = K_G[P_G - P_B - \sigma_G(\pi_G - \pi_B)] \approx K_G[P_G - P_B - \pi_G], \tag{2.13}$$

where P_G and P_B are the hydrostatic pressures associated with the glomerular capillaries and the Bowman's capsules, π_G and π_B are the colloid oncotic pressures associated with the glomerular capillaries and the Bowman's capsules, K_G is the glomerular filtration coefficient, and σ_G is the glomerular albumin reflection coefficient. Noting that the membranes in the glomerular capillaries do not allow the passage of albumin, we assumed $\sigma_G = 1$ and $\pi_B = 0$ in Eq. (2.13). We assumed that P_B is constant. Indeed, P_B hardly varies except in rare cases, e.g., when the urinary tract is obstructed [47]. P_G depends on the renal plasma flow (RPF), a fraction of CO, which is perturbed by the fluctuations in PV [48]. Assuming that CO is proportional to PV:

$$J_{RPF} = \bar{J}_{RPF} \frac{V_P}{\bar{V}_P}, \tag{2.14}$$

where J_{RPF} is RPF, and $\bar{J}_{RPF}$ is its nominal value corresponding to the nominal PV, that is $\bar{V}_P$. The perturbations in J_{RPF} due to the fluctuations in PV induced by burn injury and resuscitation are strictly compensated for with the modulation of the renal capillary resistance (called the glomerular resistance [49]), regulated by the tubuloglomerular feedback (TGF) . We expressed TGF as a simple phenomenological dynamic modulation of a hypothetical glomerular resistance, called R_G:

$$\tau_{TGF} \frac{d\Delta R_G}{dt} = -\Delta R_G + \frac{K_{TGF}}{\bar{J}_{GFR}} (J_{GFR} - \bar{J}_{GFR}), \tag{2.15}$$

where $\Delta R_G = R_G - \bar{R}_G$ is the deviation of R_G from its nominal value $\bar{R}_G$ enforced by TGF, τ_{TGF} and K_{TGF} are the time constant and the sensitivity associated with TGF, and $\bar{J}_{GFR}$ is the nominal value of GFR. Noting that P_G is proportional to RPF and inversely proportional to R_G (since an increase in R_G results in a decrease in RPF, therefore

decreased P_G), we expressed P_G as a simple phenomenological function of J_{RPF} and R_G:

$$P_G = \lambda_G \frac{J_{RPF}}{R_G}, \tag{2.16}$$

where λ_G is a constant coefficient representing the sensitivity of P_G to J_{RPF} and R_G. We expressed π_G as a function of π_C (see Eq. (2.3)) based on the idealistic assumption that albumin content is conserved in the renal arteries and in the glomerular capillaries, meaning that it will not pass to the Bowman's capsule:

$$[A]_C J_{RPF} = [A]_G (J_{RPF} - J_{GFR}) \rightarrow [A]_G = \frac{J_{RPF}}{J_{RPF} - J_{GFR}} [A]_C = \frac{1}{1-\varepsilon_{GFR}} [A]_C, \tag{2.17}$$

where $[A]_G$ is the glomerular albumin concentration and $\varepsilon_{GFR} = \frac{J_{GFR}}{J_{RPF}}$ is the filtration fraction [50]. Hence, since ε_{GFR} is naturally always less than one, and based on the assumption that $C_{O,G} = C_O$, i.e., the relationship between albumin concentration and colloid oncotic pressure is the same in the renal capillaries and in the glomerular capillaries, π_G can be expressed by the following:

$$\pi_G = \frac{1}{1-\varepsilon_{GFR}} \pi_C \approx (1 + \varepsilon_{GFR}) \pi_C. \tag{2.18}$$

Plugging Eq. (2.16) and Eq. (2.18) into Eq. (2.13) yields the following expression for GFR:

$$J_{GFR} \approx \frac{K_G J_{RPF}}{J_{RPF} + K_G \pi_C} \left[\lambda_G \frac{J_{RPF}}{R_G} - P_B - \pi_C \right]. \tag{2.19}$$

Note that GFR is now expressed in terms of PV (J_{RPF}; see Eq. (2.14)) and plasma albumin content (π_C; see Eq. (2.4)). Hence, our hybrid mechanistic-phenomenological model of GFR allows us to represent GFR using macroscopic volume kinetics.

2.3.2 Reabsorption Rate

Reabsorption rate (J_{RR}) is dictated by the modulation of glomerulotubular balance (GT; $J_{RR,GT}$) and the pure water reabsorption in the collecting ducts governed by the Antidiuretic hormone level (ADH; $J_{RR,ADH}$):

$$J_{RR} = J_{RR,GT} + J_{RR,ADH}. \tag{2.20}$$

GT modulates the proximal tubules so that approximately 20% of GFR reaches the collecting ducts [51], [52].

$$J_{RR,GT} \approx 0.8 J_{GFR}. \tag{2.21}$$

The ADH content is modulated by baroreceptors (inversely related to the changes in PV) and osmoreceptor (directly related to the changes in sodium concentration ($[Na^+]$) in the blood) signals and affects the pure water reabsorption rate at the collecting ducts [50], [53]. This means that when PV is reduced, the ADH is increased to raise the pure water reabsorption and retain more water in the body to compensate for that. An increased plasma sodium concentration would have similar effects [50]. We expressed the dynamics of the ADH content by the following phenomenological model:

$$\frac{d(ADH)}{dt} = K_{ADH} e^{\left(-\lambda_{V_P} \Delta V_P + \lambda_{[Na^+]} \Delta [Na^+]\right)} - 0.27 K_{ADH} [ADH] \frac{J_{GFR}}{\bar{J}_{GFR}} - 0.73 K_{ADH} [ADH] \frac{V_P}{\bar{V}_P}, \tag{2.22}$$

where ADH is the ADH content in the extracellular fluid, K_{ADH} is the nominal ADH secretion rate, λ_{V_P} and $\lambda_{[Na^+]}$ are positive constant coefficients representing the sensitivity of ADH secretion on the changes in PV and $[Na^+]$, and $[ADH]$ is ADH concentration in the extracellular fluid:

$$[ADH] = \frac{ADH}{V_P + V_{BT} + V_{IT}}. \tag{2.23}$$

The coefficients 0.27 and 0.73 in Eq. (2.22) come from the fact that approximately 27% of ADH is excreted in the kidneys, proportional to GFR, since it is not reabsorbed in the kidneys [54], and the remaining 73% are metabolized in the liver, proportional to hepatic blood flow, and therefore, to PV [55]). Then as mentioned earlier, ADH modulates the reabsorption fraction of pure water at the collecting ducts (ε_{RR}). We adopted the Michaelis-Menten equation to express the relationship between $[ADH]$ and the ε_{RR} [53]:

$$\varepsilon_{RR} = K_{RR}\frac{[ADH]}{[ADH]_{50}+[ADH]}, \tag{2.24}$$

$$J_{RR,ADH} = \varepsilon_{RR}(J_{GFR} - J_{RR,GT}), \tag{2.25}$$

where K_{RR} is the maximum RF, and $[ADH]_{50}$ is the ADH concentration corresponding to $\varepsilon_{RR} = \frac{1}{2}K_{RR}$. We computed $[Na^+]$, used in Eq. (2.22), based on the idealistic assumption that the sodium content (mass) is conserved in the body (including the collecting ducts) after burn injury and resuscitation, and is just diluted as the pure water reabsorption increases in the collecting ducts:

$$[Na^+] = \frac{\bar{J}_{RR,ADH}}{J_{RR,ADH}}\overline{[Na^+]}, \tag{2.26}$$

where $\overline{[Na^+]}$ is the nominal sodium concentration corresponding to the nominal RR $\bar{J}_{RR,ADH}$. That the change in $[Na^+]$ primarily depends on $J_{RR,ADH}$ may be justified to an extent because $J_{RR,ADH}$ consists of pure water diluting the plasma [53], while the sodium content remained the same.

Combining Eq. (2.12)-(2.26), we come to the following expression for UO:

$$J_U = J_{GFR} - J_{RR} = J_{GFR} - J_{RR,GT} - J_{RR,ADH}$$

$$\approx 0.2\frac{K_G J_{RPF}(V_P)}{J_{RPF}+K_G\pi_C}\left[\lambda_G\frac{J_{RPF}(V_P)}{R_G} - P_B - \pi_C\right](1-\varepsilon_{RR}). \tag{2.27}$$

Note that UO is now expressed in terms of PV (J_{RPF}; see Eq. (2.14)) and plasma albumin content (π_C; see Eq. (2.4)), and ADH concentration. Hence, our hybrid mechanistic-phenomenological model of UO allows us to represent UO using macroscopic VK and ADH dynamics.

2.4 Burn-Induced Pathophysiology in Volume Kinetics

The burn-induced pathophysiological perturbations in VK and kidney functions were represented by an array of phenomenological models, which describe local and systemic pathophysiological changes induced by burn injury in the form of time-varying perturbations acting on the parameters and variables associated with VK and kidney function. Local perturbations, restricted to burnt tissues, include: (i) partial destruction of capillaries in burnt tissues [2], (ii) denaturation of protein in burnt tissues [39], [56], [57], (iii) transient negative hydrostatic pressure in burnt tissues [56], [58], and (iv) dermal fluid loss [59], [60]. Systemic perturbations include: (i) time-varying changes in capillary filtration and albumin transport [38] and (ii) vasodilation [61].

We devised a universal function, $\phi(t)$, to represent the time-varying perturbations in all the VK and renal function parameters and variables:

$$\phi\left(M_W, \lambda_{1,W}, \lambda_{2,W}, t\right) = M_W\left(e^{-\lambda_{1,W}t} - e^{-\lambda_{2,W}t}\right), \tag{2.28}$$

where M_W is the maximum perturbation, $\lambda_{1,W}$ and $\lambda_{2,W}$ are the slow time constant and fast time constant associated with the decay of the perturbation, all corresponding to a specific perturbation $W \in \{\alpha_{BT}, \alpha_{IT}, P_C, P_{BT}\}$, where α_{BT} and α_{IT} are pore ratios associated with burnt and intact tissues, P_C represents the change in capillary

hydrostatic pressure caused by post-burn vasodilation, and P_{BT} the negative hydrostatic pressure in burnt tissues (see below for details). Eq. (2.28) describes an intensifying perturbation post-burn, which reaches its maximum at a varying time post-injury and then starts to decline.

2.4.1 Local Pathophysiology

We expressed the partial destruction of capillaries in burnt tissues as a decrease in the capillary filtration coefficient $K_{C,BT}$ and permeability surface area coefficient PS_{BT} (see Eq. (2.34)) [2]. This is in fact the only pathophysiology caused by burn that actually reduces the amount of water and protein filtered from the vascular space to the tissues. The protein denaturation is expressed as a protein influx Q_{PD} into the burnt tissues [39], [56], [57] (see Eq. 2.2b):

$$Q_{PD} = \hat{Q}_{PD} e^{-\lambda_{PD} t}, \tag{2.29}$$

where $\hat{Q}_{PD}$ is the protein influx immediately post-burn, decaying with a time constant of λ_{PD}. Considering the Starling equation (Eq. (2.3)), one can see that this excessive protein in the burnt tissue contributes to drawing more fluid into the burnt tissue (increasing the driving force in the direction of tissues), causing more edema.

We expressed the transient negative hydrostatic pressure in burnt tissues using $\phi(t)$ in Eq. (2.28) as follows:

$$\Delta P_{BT}(t) = -\phi\left(M_{P_{BT}}, \lambda_{1,P_{BT}}, \lambda_{2,P_{BT}}, t\right), \tag{2.30}$$

where $\Delta P_{BT}(t)$ is the burn-induced perturbation in the hydrostatic pressure in burnt tissues. The hydrostatic pressure in burnt tissues is then computed by combining Eq. (2.9) and Eq. (2.30):

$$P_{BT}(t) = -\frac{\alpha}{R(y_{BT})} + \gamma - \phi\left(M_{P_{BT}}, \lambda_{1,P_{BT}}, \lambda_{2,P_{BT}}, t\right). \tag{2.31}$$

Like protein denaturation, an intense negative pressure in the burnt tissue means a larger driving force for the fluid to move from the vascular space into the burnt tissue. We used phenomenological models of evaporation and exudation from literature, where these models were statistically driven from large populations of burn injury patients [62], [63]:

$$J_{EV,BT} = \begin{cases} K_{1,EV}\varepsilon_B S_B e^{\lambda_{1,EV}t}, & t < 6\ hr \\ K_{2,EV}\varepsilon_B S_B e^{\lambda_{2,EV}t}, & t > 6\ hr \end{cases}, \tag{2.32a}$$

$$J_{EV,IT} = K_{1,EV}\,(1 - \varepsilon_B)S_B, \tag{2.32b}$$

$$S_B = \begin{cases} Human, & 0.0242H^{0.396}W^{0.538} \\ Sheep & 1 \end{cases}, \tag{2.32c}$$

$$J_{EX} = K_{EX}\varepsilon_B S_B e^{\lambda_{EX}t}, \tag{2.33a}$$

$$Q_{EX} = J_{EX}\eta_{EX}[A]_{BT}, \tag{2.33b}$$

where $K_{1,EV} > 0$, $K_{2,EV} > 0$ and $K_{EX} > 0$ are constant coefficients, and $\lambda_{2,EV} > 0$, $\lambda_{2,EV} < 0$ and $\lambda_{EX} < 0$ are time constants, ε_B is the fraction of body surface subject to burn, and S_B is total body surface area, which is estimated to be 1 m^2 for sheep, and as we will discuss in chapter 4, is estimated based on the Haycock formula, depending on H (height in cm) and W (weight in kg) for humans. η_{EX} is the ratio between the albumin concentration in the exudate and the albumin concentration in the burnt tissues [36].

2.4.2 Systemic Pathophysiology

We expressed the systemic impact of burn injury as time-varying changes in the capillary filtration, albumin reflection, and permeability-surface area coefficients (representing perturbations in capillary filtration and albumin transport) as well as capillary hydrostatic pressure (representing perturbation in vasodilation). By capitalizing on the pore theory of trans-capillary exchange [64], [65], we expressed the capillary filtration, albumin reflection, and permeability-surface area coefficients associated with burnt and intact tissues as functions of the pore radius ratios α_X, $X \in \{BT, IT\}$, defined as the ratio of the albumin radius to the capillary pore radius:

$$K_{C,X} = \overline{K}_{C,X} k_{PD,X} \frac{\bar{\alpha}_X^4}{\alpha_X^4}, \tag{2.34a}$$

$$\sigma_X = 1 - (1 - \alpha_X)^2, \tag{2.34b}$$

$$PS_X = \overline{PS}_X k_{PD,X} \frac{\bar{\alpha}_X^2 (1 - \alpha_X^2)}{(1 - \bar{\alpha}_X^2)\alpha_X^2}, \tag{2.34c}$$

where $k_{PD,X}$ is the remaining fraction of the capillaries after partial destruction, while $\overline{K}_{C,X}$, $\overline{PS}_X$, and $\bar{\alpha}_X$ are the nominal values of $K_{C,X}$, PS_X, and α_X, adjusted for the water fraction in burnt and intact tissues, weight, and capillary recruitment [36]:

$$\overline{K}_{C,BT} = \overline{K}_C \varepsilon_B r_{FV} \eta_{CR},\ \overline{K}_{C,IT} = \overline{K}_C (1 - \varepsilon_B r_{FV}) \eta_{CR}, \tag{2.35a}$$

$$\overline{PS}_{BT} = \overline{PS} \varepsilon_B r_{FV} \eta_{CR},\ \overline{PS}_{IT} = \overline{PS} (1 - \varepsilon_B r_{FV}) \eta_{CR}, \tag{2.35b}$$

where $\overline{K}_C$ and $\overline{PS}$ are nominal capillary filtration and permeability surface area coefficients in the absence of burn injury, $\eta_{CR} = \left(2\frac{V_P}{\bar{V}_P} - 1\right)$, which shows that the parameters in Eq. (2.35) are extensive and depend on PV), and r_{FV} is the fluid volume ratio between the skin and the total interstitial compartment [36]. Note that $k_{PD} = 1$ if $X = IT$, because capillary destruction does not occur in intact tissues.

We expressed the burn-induced changes in these coefficients by formalizing the burn-induced changes in the capillary pore radius ratios using Eq. (2.28):

$$\alpha_X(t) = \bar{\alpha}_X - \phi(M_{\alpha_X}, \lambda_{1,\alpha_X}, \lambda_{2,\alpha_X}, t). \tag{2.36}$$

This means that after the burn injury, as the pores in the burnt and intact tissue are enlarged due to inflammation, the pore ratio decreases, reducing σ_X (Eq. (2.34b)), and increasing both $K_{C,X}$ and PS_X (Eq. (2.34a) and (2.34c)). All of this leads to an increased surface area for the filtration of water and protein from the intravascular space into the tissues since the driving force was already promoted in that direction.

We likewise expressed the burn-induced change in capillary hydrostatic pressure [61] using Eq. (2.28):

$$\Delta P_C(t) = \phi(M_{P_C}, \lambda_{1,P_C}, \lambda_{2,P_C}, t). \tag{2.37}$$

The overall capillary hydrostatic pressure is computed by combining Eq. (2.8) and Eq. (2.37):

$$P_C = \bar{P}_C + E_C(V_P - \bar{V}_P) + \phi(M_{P_C}, \lambda_{1,P_C}, \lambda_{2,P_C}, t). \tag{2.38}$$

The increased capillary hydrostatic pressure also contributes to the increased driving force in the plasma to tissue direction.

2.5 Two of the Body's Safety Factors Against Edema

As these burn perturbations happen, the plasma is being depleted of water and protein, while the tissues are getting more and more edematous. One of the most important safety factors of the body against this type of edema, is the lymphatic flow that has an incredible ability to increases to up to 50-fold in response to this excessive fluid stored

in the tissue and increased hydrostatic pressure. But as shown in Eq. (2.5), the lymphatic flow has its own limitations and eventually saturates.

Another safety factor against edema is the fact that as plasma volume decreases, the driving force in the Starling equation also does. This puts a stop to the filtration of water and protein when PV is significantly reduced.

Needless to say, these safety factors are not enough to restore the water and protein balance between plasma and the tissues after severe burn injuries, and that is why prompt and sufficient fluid resuscitation is absolutely necessary.

Chapter 3: Model Optimization, Training and Validation in Animals

The validation of our model is done in two phases.

The first phase includes comprehensive validation of both volume kinetics and kidney function predictions in a dataset collected from sheep. The main advantage of this dataset was the availability of measurements that are not usually collected from human subjects and let us evaluate a manifold of our predictions not only by comparing them to literature, but also against real data.

Then once we have some evidence that the predictions of the model are consistent with human physiology and burn pathophysiology, we can move on to our-much more diverse but limited in number of measurements- human dataset in phase 2 of validation.

In this chapter, using the dataset collected from 16 sheep, we showed that our mathematical model can be characterized with physiologically plausible parameter values to accurately predict blood volume kinetic and kidney function responses to burn injury and resuscitation on an individual basis against a wide range of pathophysiological variability [40].

3.1 Experimental Data

Experimental dataset used for the first phase of validation of our mathematical model was formed by combining the two datasets collected from two prior work under the approval of local Institutional Animal Care and Use Committee [66], [67]. One dataset was obtained from a study conducted on adult sheep (N=8) with the median weight of

40kg and full-thickness burn injury of 40% total body surface area (TBSA). Burn resuscitation by Lactated Ringers was initiated 1 hour post burn and continued for 48 hours. Resuscitation was performed to maintain a target UO of 1-2ml/kg/h, which is considered as normal UO in sheep. Key measurements in the dataset used in this work include hourly records of fluid infusion and UO, and more sparse measurements of hematocrit (HCT; N=12 per sheep on the average). The other dataset was obtained from another study conducted on adult sheep (N=8) with the median weight of 50kg and full-thickness burn injury of 30% TBSA. Burn resuscitation by Lactated Ringers was initiated 2 hours post burn and continued for ≥24 hours, while sheep were monitored for 72 hours. Resuscitation was performed to restore and maintain central venous pressure and pulmonary wedge pressure. Key measurements in the dataset used in this work include fluid infusion, UO, and HCT. In a subset of the sheep, measurements of protein concentrations in plasma, burnt tissue, and intact tissue compartments, as well as fractions of lymphatic flow from burnt and intact tissue to vascular compartment at lymph nodes were made. Table 3.1 summarizes the measurements available in our dataset.

We computed PV from HCT using a formula reported in prior work [68], [69] based on the assumption that (i) the baseline BV of sheep is 63.5ml/kg and (ii) no blood loss occurred during the course of burn resuscitation (so that red blood cell volume was preserved).

Table 3.1: Measurement availability in dataset used for validation. N: number of subjects associated with the measurement. PV: plasma volume. UO: urinary output. BT: burnt tissue. IT: intact tissue. Albumin: albumin concentration.

	Fluid Dose	PV	UO	Lymph Flow (BT)	Lymph Flow (IT)	Albumin (Plasma)	Albumin (BT)	Albumin (IT)
N	16	16	16	6	8	5	2	2

3.2 Method: Model Optimization, Training and Validation

We examined the validity of our mathematical model as follows. First, we categorized the parameters in the mathematical model into subject-invariant and subject-specific parameters. Second, we estimated the values of subject-specific parameters by fitting the mathematical model to the measurements in the dataset while fixing subject-invariant parameters to respective pre-specified values. Third, we examined the validity of the mathematical model by analyzing the goodness of fit and estimated parameter values associated with the mathematical model. Details follow.

First, we categorized the parameters in the mathematical model into subject-invariant and subject-specific parameters. Subject-invariant parameters included (i) those (mostly associated with extensive properties and mechanistic components in the mathematical model) whose values appear consistent in multiple prior literatures (e.g., nominal water volume and albumin content in the vascular and tissue compartments and the hydrostatic pressure in Bowman's capsule), and (ii) those whose values must be selected to produce mechanistically relevant physiological responses (e.g., parameters associated with the tissue compliance model, which must be chosen to yield physically relevant tissue hydrostatic pressure for a range of tissue volumes). The values of these subject-invariant parameters were mostly determined based on the

existing literature (see Table 3.4 for the values of these parameters (marked as I) and specific literatures we used to determine them). Subject-specific parameters included (i) those whose values are anticipated to exhibit large inter-subject variability (e.g., burn-induced perturbations and nominal glomerular filtration coefficient), (ii) those whose values have rarely been reported in the existing literature (e.g., capillary elastance and nominal lymphatic flow), and (iii) those associated with phenomenological components in the mathematical model whose values are inherently unknown. After all, a total of 58 parameters were categorized into 34 subject-invariant and 24 subject-specific parameters.

Second, we estimated the values of subject-specific parameters by fitting the mathematical model to the measurements in the dataset while fixing subject-invariant parameters to respective pre-specified values

Before conducting parameter estimation, it is important to evaluate the richness of data against the number of parameters we need to identify. In our dataset, one set [66] had 60 measurements per subject on the average (including 12 PV and 48 UO measurements), while the other dataset [67] had 161 measurements per subject on the average (including 24 PV, 24 UO measurements, 41 lymphatic flow associated with burnt tissues, 50 lymphatic flow associated with intact tissues, 10 plasma albumin concentration, 7 burnt tissue albumin concentration, and 5 intact tissue albumin concentration). The datasets were not deemed too sparse to estimate the subject-specific parameters. However, the number of measurements in the datasets may not be rich enough to robustly estimate all the 24 subject-specific parameters.

Considering this, we selected a small subset of sensitive subject-specific parameters and estimated them while fixing the remaining insensitive subject-specific parameters to respective population-average values. Therefore, there are two main steps in conducting our optimization, first, identifying the sensitive subject-specific parameters and fixing the rest to population average values, and second, estimation of the subject-specific parameters.

3.2.1 Optimization Step 1: Classification of Sensitive and Insensitive Subject-Specific Model Parameters

To classify the subject-specific parameters into sensitive and insensitive categories, we examined and compared the degree of inter-individual variability associated with all the subject-specific parameters using regularized system identification. This approach was chosen particularly because our model is highly nonlinear and complex (large number of parameters before dimension reduction), and many established protocols that are routinely used for sensitivity and identifiability analysis for linear models were not readily applicable to ours.

To do this, we first needed to determine the population-average parameter values, $\bar{\theta}$, by fitting our mathematical model simultaneously to all the measurements in all subjects in the dataset using the pooled approach [70]. This is achieved by fitting our mathematical model to minimize the cost function in Eq. (3.1):

$$\bar{\theta} = \arg\min_{\theta} \bar{J}(\theta) = \arg\min_{\theta} \sum_{i=1}^{N} \sqrt{\sum_{j=1}^{M_i} \left(\sum_{k=1}^{D_{ij}} \frac{\left| y_{ij}^{d}(t_k) - y_{ij}(t_k, \theta) \right|}{Y_{ij}} \right)^2} \quad (3.1)$$

where θ is the vector of subject-specific parameters, N is the number of subjects (=16), M_i is the number of physiological variables measured in the subject i (e.g., M_i=2 if PV and UO were measured), D_{ij} is the number of measurements associated with the physiological variable j in the subject i during the initial 48 hours, $y_{ij}^d(t_k)$ is the value of the physiological variable j associated with the subject i measured at time t_k, $y_{ij}(t_k, \theta)$ is the value of the same physiological variable at time t_k predicted by the mathematical model for a given θ, and Y_{ij} is the normalization factor for the physiological variable j associated with the subject i, which is defined as the range of y_{ij}^d multiplied by D_{ij} (so that the normalized errors associated with all the physiological variables have comparable magnitudes across all subjects).

Second, we estimated all the 24 subject-specific parameters θ_i associated with the subject i by fitting our mathematical model to all the measurements associated with the subject i to minimize the cost function in Eq. (3.2), using a regularized fitting that minimizes the number of parametric deviations from the population-average values [71], [72]:

$$\theta_i = \arg\min_{\theta} J_i(\theta) = \arg\min_{\theta} \sqrt{\sum_{j=1}^{M_i} \left(\sum_{k=1}^{D_{ij}} \frac{\left| y_{ij}^d(t_k) - y_{ij}(t_k, \theta) \right|}{Y_{ij}} \right)^2} + \lambda_p \sum_{l=1}^{24} \left| \frac{\theta(l) - \bar{\theta}(l)}{\Theta_l} \right|, \quad (3.2)$$

where λ_p is the regularization weight and Θ_l is the normalization factor for the l-th element $\theta(l)$ of θ, which is defined so that all the elements in θ are ranged approximately between 0 and 1. λ_p was found in an ad-hoc fashion, by testing different values between 0 and 1. A value of 0.05 was finally chosen, which eliminated the

highest number of parameters without significantly deteriorating the prediction accuracy. Higher values would put too large of a cost on parameter deviation, only allowing a small number of parameters to vary, and eventually led to larger prediction errors. Lower values, however, were too liberal and resulted in many parameters being introduced as sensitive. This analysis was performed on the same training set that we used to derive the population-average model. Another approach we could take here, was to use a subset of test set to find a "global" optimum value for λ_p.

Third, using θ_i thus estimated from all the 16 subjects, we computed the average normalized deviation of each element in θ_i. Then, we selected those elements of θ_i associated with deviations thus computed larger than a threshold value as sensitive subject-specific parameters. We set the threshold deviation as 10% based on empiric trial and error, which yielded 12 sensitive subject-specific parameters. Post-hoc parametric sensitivity analysis indicated that the mathematical model was not actually sensitive to one of them, which was thus removed. This exercise yielded a total of 11 sensitive subject-specific parameters (Table 3.2).

Table 3.2: Sensitive subject-specific parameters and their average normalized deviations from population-average values.

Parameter	τ_{TGF}	$M_{\alpha_{IT}}$	$\bar{J}_C$	$\bar{J}_{RR,ADH}$	λ_{V_P}	M_{P_C}	λ_{1,P_C}	C_L	$\bar{P}_C$	$\hat{Q}_{PD}$	K_G
Deviation[%]	48.2	18.8	16.9	16.7	16.4	15.3	14	13.2	11.6	11.5	10.3

3.2.2 Optimization Step 2: Model Fitting and Estimation of Subject-Specific Model Parameters

We estimated the 11 sensitive subject-specific parameters selected above on the individual basis by fitting our mathematical model to all the available measurements associated with each subject to minimize the cost function in Eq. (3.3), while fixing the remaining 13 insensitive subject-specific parameters to respective population-average values ($\bar{\theta}$ in Eq. (3.1)), and as well, fixing the subject-invariant parameters to respective pre-specified values (see Table 3.4 for the values of these parameters, marked as S):

$$\breve{\theta}_i = \arg\min_{\breve{\theta}} \breve{J}_i(\breve{\theta}) = \arg\min_{\breve{\theta}} \sqrt{\sum_{j=1}^{M_i} \left(\sum_{k=1}^{D_{ij}} \frac{\left| y_{ij}^d(t_k) - y_{ij}(t_k, \breve{\theta}) \right|}{Y_{ij}} \right)^2} \qquad (3.3)$$

where $\breve{\theta}$ is the vector of sensitive subject-specific parameters, and $\breve{\theta}_i$ is $\breve{\theta}$ estimated for the subject i.

In sum, we derived 16 subject-specific mathematical models as well as a population-average mathematical model using the dataset. (See Table 3.4 for the ranges of these parameters across 16 subjects, marked as SS).

3.2.3 Optimization Settings

The complexity and nonlinearity associated with our mathematical model strongly suggests the non-convex nature of the numerical optimization problems in Eq. (3.1)-(3.3). To derive robust estimates of parameters from our numerical optimization problems, we used multiple initial conditions and tight parameter bounds as follows. First, we used a multi-start gradient descent method in MATLAB ("globalsearch" in conjunction with "fmincon" commands). We empirically selected user-configurable

settings (e.g., the number of initial conditions) so that the numerical optimization could yield accurate parameter estimates when simulated measurements associated with the population-average model (i.e., our mathematical model characterized by $\bar{\theta}$ in Eq. (3.1)) are inputted to Eq. (3.3). Second, we enforced tight parameter bounds as constraints in solving the numerical optimization problems to effectively guide the solution into a mechanistically plausible parameter space. We carefully specified many of these bounds by leveraging the prior knowledge on the parameter values (see Table 3.4). It is noted that we intended to also avoid overfitting with these parameter bounds. Since the number of measurements in our datasets may not be sufficiently large to robustly solve our numerical optimization problems, mechanistically plausible parameter bounds are expected to benefit in preventing overfitting against measurement noises and errors by keeping the parameter estimates from assuming mechanistically illegitimate values.

All in all, our approach to solve the model fitting problem in Eq. (3.3) by incorporating (i) a small number of sensitive subject-specific parameters, (ii) multi-start gradient descent, and (iii) parameter bounds appeared to be effective: when Eq. (3.3) was solved using simulated measurements associated with the population-average model repeatedly, NMAE<0.1% was consistently achieved, and all the 11 sensitive subject-specific parameters had very small errors of <3%.

3.2.4 Validation

We examined the validity of the mathematical model by analyzing the goodness of fit and estimated parameter values associated with the mathematical model as follows.

First, we examined the ability of our mathematical model to predict PV and UO responses on the individual basis, in terms of normalized mean absolute error (NMAE), correlation coefficient, and the Bland-Altman statistics between actual PV and UO measurements associated with each sheep in the dataset versus PV and UO predicted by our mathematical model characterized with the corresponding subject-specific parameter values. Second, we examined the ability of our mathematical model to predict physiologically plausible VK and renal function responses by (i) quantitatively analyzing, on the individual basis, NMAE, correlation coefficient, and the Bland-Altman statistics between actual lymphatic flow and albumin concentration associated with (a subset of) each sheep in the dataset (see Table 3.1) versus lymphatic flows and albumin concentrations predicted by our mathematical model characterized with the corresponding subject-specific parameter values, and also (ii) qualitatively comparing VK and renal function responses predicted by our mathematical model characterized by population-average parameters with contemporary knowledge on burn pathophysiology and findings from recent studies. Third, we examined the physiological plausibility of our mathematical model by comparing the subject-specific and population-average parameter values estimated by fitting the mathematical model to the dataset with known typical values and those reported in the literature.

3.3 Results

Table 3.3 summarizes NMAE, correlation coefficient, and the Bland-Altman statistics (i.e., the limits of agreement) associated with PV, UO, lymphatic flow, and albumin concentration predicted by the mathematical model. Fig. 3.1 presents representative

examples of measured versus model-predicted PV and UO responses of two 40kg sheep subject to 40% burn whose PV was resuscitated (a) beyond the pre-burn level and (b) just to the pre-burn level. Fig. 3.2 presents VK and kidney function responses to burn injury and resuscitation predicted by population-average mathematical model in response to population-average burn resuscitation input.

Table 3.3: Normalized mean absolute error (NMAE; reported in median (IQR)), correlation coefficient (r), and Bland-Altman limits of agreement (LoA) associated with plasma volume, urinary output, lymphatic flow, and albumin concentration predicted by the mathematical model. PV: plasma volume. UO: urinary output. P: plasma. BT: burnt tissues. IT: intact tissues. LoA: 95% limits of agreement (bias+/-2×SD).

	PV [ml] (N=16)	UO [ml/h] (N=16)	Lymphatic Flow [ml/h]		Albumin Concentration [g/l]		
			BT (N=6)	IT (N=7)	P (N=4)	BT (N=2)	IT (N=2)
NMAE [%]	16 (3)	17 (3)	17 (7)	17 (6)	19 (10)	7 (6)	17 (11)
r	0.82	0.66	0.92	0.91	0.85	0.98	0.85
LoA	50+/-404	-8+/-70	0.2+/-5.8	4+/-56	0.5+/-8.2	-0.07+/-3.7	2.3+/-4.0

3.4 Discussion

In the lack of consensus on the optimal burn resuscitation regimen and extreme inter-patient physiological variability in burn-induced responses, a credible mathematical model of burn injury and resuscitation may provide a meaningful basis for development and non-clinical testing of burn resuscitation protocols and algorithms in a wide range

of patients. Existing mathematical models are associated with at least one of the following limitations: they are (i) not capable of predicting physiological responses essential in measuring the severity of burn injury and the effectiveness of resuscitation (including PV and UO), (ii) not rigorously validated to demonstrate the ability to capture formidable inter-patient variability in burn- and resuscitation-induced responses, and (iii) often equipped with obsolete knowledge of burn pathophysiology. Our goal was to develop a mathematical model of burn injury and resuscitation ideally suited to in-depth understanding of complex burn-induced VK and renal responses as well as development and non-clinical testing of burn resuscitation protocols and algorithms.

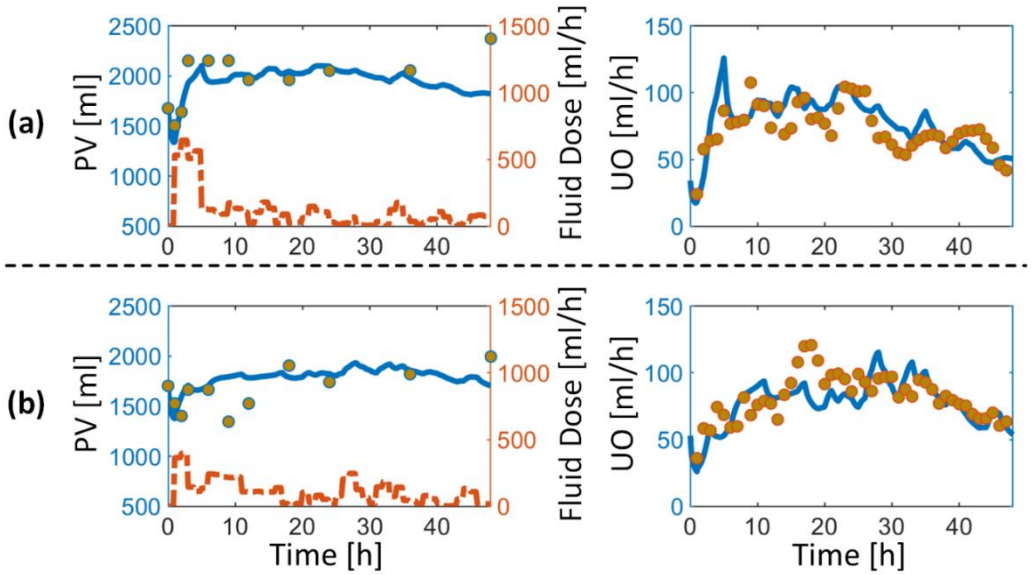

Fig. 3.1: Measured versus model-predicted plasma volume (PV) and urinary output (UO) responses of two 40kg sheep subject to 40% burn. Circles: measured responses. Solid lines: model-predicted responses. Dashed lines: measured fluid dose. (a) Sheep with PV resuscitated 200ml beyond pre-burn level 48 hours post-burn. (b) Sheep with PV resuscitated just up to pre-burn level 48 hours post burn.

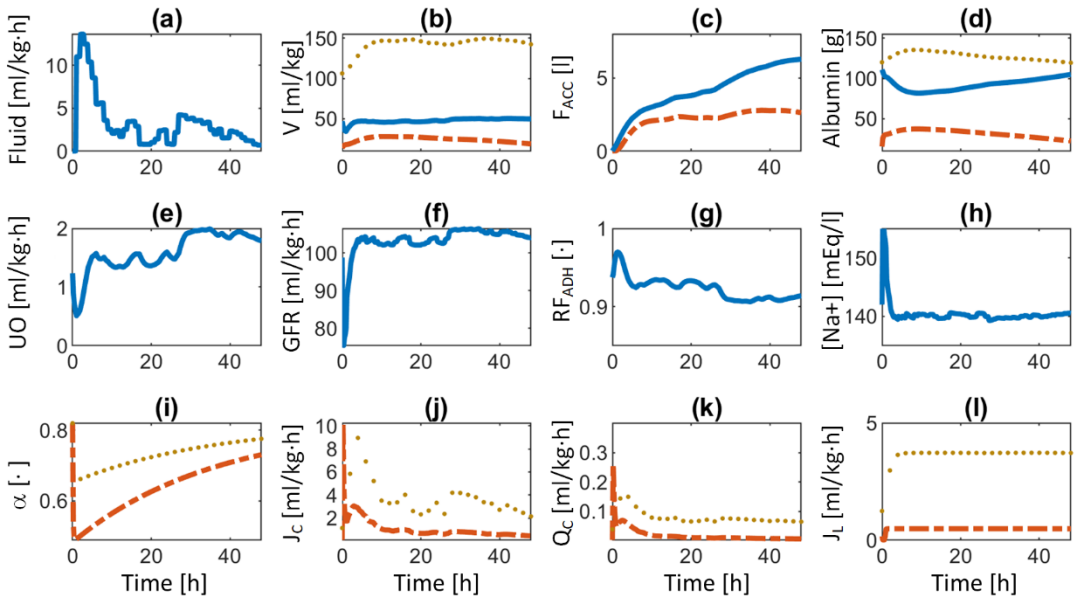

Fig. 3.2: Volume kinetic and renal function responses to burn injury and resuscitation predicted by population-average mathematical model. V: water volume. F_{ACC}: accumulated fluid. RF_{ADH}: reabsorption fraction due to ADH . α: capillary pore radius ratio. J_C: capillary filtration. Q_C: albumin transport across the capillary wall. J_L: lymphatic flow. In (b) and (d), blue solid, orange dash-dot, and brown dotted lines are plasma volume as well as burnt and intact tissue volumes, respectively. In (c), blue solid and orange dash-dot lines are accumulated resuscitation fluid volume and fluid creep, respectively. In (i)-(l), orange dash-dot and brown dotted lines correspond to burnt and intact tissues, respectively.

Our mathematical model could adequately predict PV and UO responses to burn injury and resuscitation (Table 3.3 and Fig. 3.1). In particular, the NMAE associated with our UO prediction was considerably smaller than a recently reported black-box model [73] (30+/-6%) while the underlying UO variability was comparable (44% (our dataset) versus 38% [73] in terms of the coefficient of variation (CoV)). In addition, the level of prediction accuracy was reasonably consistent across subjects (3% in terms of IQR of NMAE for both PV and UO). Further scrutinizing UO prediction, there was 89% agreement between measured and predicted UO in terms of residing in the same range (<0.5ml/h/kg, 0.5-1.0ml/h/kg, and >1.0ml/h/kg) on the average. This is an encouraging

performance given that contemporary burn resuscitation protocols adjust resuscitation dose based on UO range rather than its value. All in all, an important related implication is that our mathematical model may be able to capture inter-patient variability in burn-related pathophysiology. In fact, when characterized with individual-specific parameters, our mathematical model could reproduce largely distinct burn- and resuscitation-induced PV and UO responses of apparently similar sheep. For example, Fig. 3.1 suggests that our mathematical model predicts PV and UO responses associated with two similar sheep of 40kg weight subject to the same 40% burn, but subject to largely distinct initial reduction in PV (approximately 300ml versus 500ml) and its subsequent recovery (200ml versus 1ml above initial PV level). Considering that VK (especially PV) and renal function (especially UO) are direct and surrogate measures of burn resuscitation, respectively, our mathematical model may be adequate for the intended context of use: development and testing of burn resuscitation protocols and algorithms.

In addition to PV and UO, our mathematical model could also predict various VK and renal responses to burn injury and resuscitation not readily accessible via routine clinical measurements in a physiologically plausible fashion. First, VK responses including protein concentrations and lymphatic flows predicted by our mathematical model exhibited adequate agreement with experimental measurements (Table 3.3). Second, all the VK and renal function responses predicted by our mathematical model exhibited behaviors qualitatively consistent with contemporary knowledge on burn pathophysiology and findings from recent studies in both individual and population-average senses. Fig. 3.2 presents responses predicted by the population-average

mathematical model. To mention a few, the model predicted that (i) PV and UO showed an anticipated trend of initial decline upon the onset the burn injury and subsequent recovery with resuscitation and also with the return of resuscitation fluid leaked into tissues back to vasculature >24 hours post burn (Fig. 3.2(b), Fig. 3.2(c), and Fig. 3.2(e)) [74], [75]; (ii) burnt tissue volume increased up to twice its initial value and peaked approximately at 10-20 hours post burn (Fig. 3.2(b)) [8]; (iii) intact tissue volume exhibited the same trend but with smaller degree (up to 30% above its initial value; Fig. 3.2(b)) [8]; (iv) plasma albumin was transported into burnt and intact tissues due to burn-induced perturbations in albumin reflection and permeability-surface area coefficients (Fig. 3.2(d) and Fig. 3.2(k); see [e] in Fig. 2.1) as a result of burn-induced increase in the capillary pore size that decreased the capillary pore radius ratio in both burnt and intact tissue (Fig. 3.2(i)) [57]; and (v) GFR increased just hours post burn even before PV was restored [76] (Fig. 3.2(f)). All in all, its ability to make physiologically plausible predictions of VK and renal function makes our mathematical model suited for gaining sophisticated insights not directly available in routine clinical measurements (e.g., UO). For example, our mathematical model predicts that on the average fluid creep peaks at approximately 10 hours post burn and that more than 50% of the resuscitation fluid in the first 24 hours leaks into tissues to exacerbate edema instead of contributing to hemodynamic recovery, which is in good agreement with the findings in the literature (Fig. 3.2(b) and Fig. 3.2(c)) [75], [77]. It also predicted that sodium concentration decreased after burn injury and resuscitation, which is also consistent with the findings in the literature [78] (Fig. 3.2(h).). Provided that rigorous development and testing of burn resuscitation protocols and algorithms require

comprehensive understanding and in-depth scrutiny of complex VK and renal function responses to burn injury and resuscitation, this attribute may confer additional credibility for the intended context of use on our mathematical model.

It is worth noting that our mathematical model could predict adequate PV and UO as well as physiologically plausible VK and renal function responses while characterized with physiologically acceptable parameter values. In fact, the majority of model parameters associated with physiological implications assumed values comparable to typical values and/or those reported in the literature both on the individual and population-average basis (Table 3.4). Such a physiological acceptability in the model parameter values suggests physiological plausibility (or perhaps even relevance) of our mathematical model, especially the novel mechanisms and components we developed (e.g., our representations for the renal function and burn-induced VK and renal perturbations). It is also worth noting that our mathematical model embraces a wealth of contemporary knowledge on burn physiology and pathophysiology based on findings in recent literatures, including but not limited to burn-induced systemic increase in capillary pore radius [38] and GFR [76] as well as highly nonlinear tissue compliance characteristics dictated by the glycosaminoglycans (GAG) properties [45]. In fact, many of these new findings were made after the pioneering work by Arturson et al. [27]–[29], Roa et al. [30]–[32], and Bert et al. [33]–[36], [79] was conducted. Hence, they were inevitably not incorporated in the existing mathematical models developed by these pioneering researchers. The physiological and mechanistic plausibility of our mathematical model combined with its incorporation of a range of contemporary knowledge on burn pathophysiology allows our mathematical model to

predict PV and UO as well as many VK and renal function responses essential to develop and test burn resuscitation protocols and algorithms against a wide range of pathophysiological variability.

Our work has a number of limitations. First, we (somewhat implicitly) assumed that fluid transfers between VK compartments are isotonic and that VK compartments are in electrolyte balance at all times. These are tenable assumptions in that (i) electrolytes pass capillary walls easily, (ii) they are mixed with water quickly and continuously, and (iii) burn resuscitation fluid considered in this work is isotonic lactated ringers. Hence, we assumed that the primary factor governing the changes in electrolyte concentration in the body is related to the change in sodium concentration due to water reabsorption in collecting ducts in the kidneys (which was considered in our kidney function model). Our mathematical model was able to predict VK and renal function responses reasonably well despite these simplifying assumptions, which suggests that the assumptions may be adequate (or at least may not have had drastic impact on the efficacy of the mathematical model). However, these assumptions may not be valid in case of burn resuscitation with fluid other than lactated ringers. Hence, future work on expanding our mathematical model by removing these assumptions is required. Second, our mathematical model only includes extracellular compartments but not intracellular compartments. As a matter of fact, we initially considered intracellular compartment due to its potential importance to electrolyte balance, but it ended up with adding unnecessary complexity to the mathematical model without any meaningful improvement in the goodness of fit. Regardless, intracellular compartment may need to be incorporated in order to broaden the applicability of our mathematical model

beyond lactated ringers. Hence, future work on expanding our mathematical model to include intracellular compartment model of adequate complexity and efficacy may be rewarding. Third, the dataset used in this work was associated with rather uniform injury severity (30%-40% TBSA). Despite a wide range of VK and renal function responses in the dataset (Table 3.1), the narrow range of injury severity may have prevented us from garnering additional insight into, e.g., the dependence of burn-induced perturbations on the injury severity. Hence, future work is required to investigate the adequacy of our mathematical model (especially its phenomenological models of burn-induced VK and renal function perturbations) under a wide range of burn injury severity, and if needed, to improve the validity and efficacy of our mathematical model against wide-ranging burn injury severity. Fourth, the mathematical model was not validated using extensive and ideal VK and renal function measurements. In particular, PV was derived from hematocrit measurements. Despite its well-known direct relationship to PV, its accuracy is not always perfect and is also impacted by disturbances such as hemolysis. In addition, UO was the only renal function measurement used to validate the mathematical model. We illustrated that our mathematical model, by virtue of mechanistic components therein, can at least predict a large number of VK and renal function variables that are qualitatively adequate (Fig. 3.2).

3.5 Conclusion

We developed a mathematical model of burn injury and resuscitation intended for use in the development and non-clinical testing of burn resuscitation protocols and

algorithms. Using the dataset associated with sheep, we demonstrated the potential of our mathematical model for such context of use: it could predict PV and UO as well as a range of VK and renal function responses to burn injury and resuscitation by virtue of its physiological and mechanistic relevance combined with contemporary knowledge of burn physiology and pathophysiology.

In order to establish its efficacy as a powerful non-clinical tool for developing and testing burn resuscitation protocols and algorithms, effort must be invested to validate our mathematical model in real-world burn patients associated with a wide range of physiological variability, injury severity, and resuscitation protocol, and that is what we intended to do in the next chapter.

3.6 Model Parameters: Nomenclature, Definitions, and Values

Table 3.4: Mathematical model parameters: definitions, categories (I/S), and values. I: subject-invariant parameters. S: subject-specific parameters. SS: sensitive, subject-specific parameters. The values are given as mean, median (IQR), or mean+/-SD.

Symbol	Definition	I/S	Value (Model)	Value (Literature)
$\overline{BV}$	Nominal blood volume [ml/kg]	I	63.5	63.5 [80]
$\bar{V}_P$	Nominal water volume in plasma [ml/kg]	I	42.8	42 [81]-46 [36]
r_{FV}	Skin fluid volume to total interstitial fluid volume ratio [·]	I	0.28	0.28 [36]
$\bar{V}_{BT}$	Nominal water volume in burnt tissue [ml/kg]	I	$120\varepsilon_B r_{FV}$	$120\varepsilon_B r_{FV}$ [36]
$\bar{V}_{IT}$	Nominal water volume in intact tissue [ml/kg]	I	$120(1-\varepsilon_B r_{FV})$	$120(1-\varepsilon_B r_{FV})$ [36]
$[\bar{A}_P]$	Nominal albumin concentration in plasma [g/ml]	I	0.059	0.059 (0.004) [67]
$[\bar{A}_{BT}]$	Nominal albumin concentration in burnt tissue [g/ml]	I	0.028	0.028 [67]
$[\bar{A}_{IT}]$	Nominal albumin concentration in intact tissue [g/ml]	I	0.028	0.028 [67]
$\bar{A}_P$	Nominal albumin content in plasma [g]	I	$[\bar{A}_P]\bar{V}_P$	-
$\bar{A}_{BT}$	Nominal albumin content in burnt tissue [g]	I	$[\bar{A}_{BT}]\bar{V}_{BT}$	-
$\bar{A}_{IT}$	Nominal albumin content in intact tissue [g]	I	$[\bar{A}_{IT}]\bar{V}_{IT}$	-
$\bar{J}_C$	Nominal capillary filtration [ml/kg·h]	SS	1.53 (0.19)	1.72 [79]
C_O	Colloid oncotic pressure constant [mmHg/g·ml]	I	250	250 [67]
$\bar{J}_L$	Nominal total lymphatic flow to plasma [ml/kg·h]	I	1.07 (0.19)	1.08 [36]
$\bar{J}_{L,BT}$	Nominal lymphatic flow from burnt tissue to plasma [ml/kg·h]	I	$\bar{J}_L\varepsilon_B r_{FV}$	$\bar{J}_L\varepsilon_B r_{FV}$ [36]
$\bar{J}_{L,IT}$	Nominal lymphatic flow from intact tissue to plasma [ml/kg·h]	I	$\bar{J}_L(1-\varepsilon_B r_{FV})$	$\bar{J}_L(1-\varepsilon_B r_{FV})$ [36]
C_L	Lymphatic maximal increase coefficient [·]	SS	0.29 (0.21)	-

S_L	Lymphatic pressure sensitivity coefficient [1/mmHg]	S	6.44	-
$\bar{P}_C$	Nominal hydrostatic capillary pressure [mmHg]	SS	8.0 (0.5)	6.7 (0.8) [82]
E_C	Capillary elastance [mmHg/ml]	S	0.0139	0.0097 [37]
α	Tissue electrostatic pressure coefficient [mmHg]	I	10	10 [45]
γ	Tissue tension pressure coefficient [mmHg]	I	3.75	3.75 [45]
$\hat{y}$	Maximum half-thickness of the extracellular matrix [·]	I	4	4 [45]
$\check{y}$	Minimum half-thickness of the extracellular matrix [·]	I	1	1 [45]
$\hat{R}$	Maximum GAG radius [·]	I	3.5	3.5 [45]
β	Radius threshold ratio [·]	I	0.23	0.23 [45]
n	Hydration response coefficient [·]	I	8	2-8 [45]
$\bar{W}_X$	Nominal hydration level [ml/g]	I	0.66	0.23-0.81 [45], [46]
$\bar{J}_{RPF}$	Nominal renal plasma flow [ml/kg·h]	I	536	536 [83]
τ_{TGF}	Tubuglomerular feedback time constant [1/h]	SS	0.35 (0.33)	-
K_{TGF}	Tubuglomerular feedback sensitivity [·]	S	5.75	-
$\bar{R}_G$	Nominal glomerular resistance [mmHg/ml/kg·h]	I	12.34	-
λ_G	Glomerular hydrostatic pressure sensitivity [mmHg^2/(ml/h·kg)^2]	I	1	-
P_B	Hydrostatic pressure in Bowman's capsules [mmHg]	I	18	18 [47]
K_G	Glomerular filtration coefficient [ml/kg·h·mmHg]	SS	9.2 (1.2)	9.6-12.0 [84]
K_{ADH}	Nominal ADH secretion rate [pg/kg·h]	I	287	287 [54], [55]
λ_{V_P}	ADH sensitivity to plasma volume change [1/ml]	SS	0.0017 (0.0008)	-
$\lambda_{[Na^+]}$	ADH sensitivity to sodium concentration change [l/mEq]	S	0.087	-
K_{RR}	Maximum collecting duct reabsorption fraction [·]	I	0.999	-
$[ADH]_{50}$	ADH concentration corresponding to $\frac{1}{2}K_{RR}$ [pg/ml]	S	0.0628	-
$[\overline{Na^+}]$	Nominal plasma sodium concentration [mEq/l]	I	142	142 [85]
$\bar{J}_{RR,ADH}$	Nominal water reabsorption rate in the collecting ducts [·]	SS	0.933 (0.01)	0.97 [51]
$\hat{Q}_{PD}$	Protein influx post burn [g/h]	SS	72.98 (53.23)	-
λ_{PD}	Protein influx decay rate [1/h]	S	10	-
$M_{P_{BT}}$	Maximum burnt tissue hydrostatic pressure perturbation [mmHg]	S	38	30 [56]
$\lambda_{1,P_{BT}}$	Burnt tissue hydrostatic pressure perturbation slow decay rate [1/h]	S	5.48	-
μ	The ratio between slow decay rate to fast decay rate [·]	S	356	-
$\lambda_{2,P_{BT}}$	Burnt tissue hydrostatic pressure perturbation fast decay rate [1/h]	I	$8\lambda_{1,P_{BT}}$	-
$K_{1,EV}$	Nominal tissue evaporation rate [ml/h·m^2]	I	18.48	18.48 [63]
$\lambda_{1,EV}$	Evaporation growth rate [1/h]	I	0.073	0.073 [63]
$K_{2,EV}$	Maximum evaporation rate [ml/h·m^2]	I	28.68	28.68 [63]
$\lambda_{2,EV}$	Evaporation decay rate [1/h]	I	-0.0052	-0.0052 [63]
ε_B	Fraction of body surface subject to burn [·]	S	0.3-0.4	dataset
S_B	Total body surface area [m^2]	I	1	1.07+/-0.16 [86]
K_{EX}	Maximum exudation rate [ml/h·m^2]	I	25	25 [62]
λ_{EX}	Exudation decay rate [1/h]	I	-0.0038	-0.0038 [62]
η_{EX}	Exudate to tissue albumin ratio [·]	S	0.69	0.75 [36]
$\bar{\alpha}$	Nominal albumin to capillary pore radius ratio [·]	S	0.82	0.7-0.9 [37]
$1 - k_{PD,BT}$	Capillary destruction fraction [·]	S	0.56	0.50 [35]
$M_{\alpha_{BT}}$	Maximum pore ratio perturbation in burnt tissue [·]	S	0.37	0.30 [39]
$M_{\alpha_{IT}}$	Maximum pore ratio perturbation in intact tissue [·]	SS	0.16 (0.11)	0.19 [87]
$\lambda_{1,\alpha}$	Pore ratio slow decay rate [1/h]	S	0.030	0.025 [36]
$\lambda_{2,\alpha}$	Pore ratio fast decay rate [1/h]	I	$\mu\lambda_{1,\alpha}$	-
M_{P_C}	Maximum capillary hydrostatic pressure perturbation [mmHg]	SS	19 (12)	23+/-5 [61]
λ_{1,P_C}	Capillary hydrostatic pressure perturbation slow decay rate [1/h]	SS	0.54 (0.08)	-
λ_{2,P_C}	Capillary hydrostatic pressure perturbation fast decay rate [1/h]	I	$\mu\lambda_{1,P_C}$	-

Chapter 4: In-Human Evaluation and Analysis of Volume Kinetics and Kidney Function after Burn Injury and Resuscitation

In this chapter we modify, extensively validate, and analyze a mathematical model capable of replicating volume kinetic and kidney function responses to burn injury and resuscitation in real-world burn patients. By leveraging clinical datasets collected from 233 real burn patients receiving resuscitation, we intend to develop a mathematical model suited to computer-aided in-human burn resuscitation trial and knowledge expansion, by expanding the model introduced in chapter 2, and utilizing systematic parametric sensitivity analysis and regularization introduced in chapter 3. We investigate the validity of the mathematical model by testing its physiological plausibility in a dedicated test dataset.

As mentioned in chapter 1, there are significant differences in mortality rate between patients of different genders, ages, and comorbidities, the cause of which are still not fully unraveled [88]–[91]. In this chapter, using the validated mathematical model, we also examine possible mechanisms responsible for the cohort-dependent differences in burn pathophysiology by comparing the mathematical models fitted exclusively to younger versus older patients, female versus male patients, and patients with versus without inhalational injury.

4.1 Clinical Data

The clinical dataset used in this paper was furnished from two sources. The first source included 207 burn patients admitted to a burn intensive care unit (ICU) in December

2007-June 2009 [92]. These patients were treated with the aid of a clinical decision support system capable of recommending the hour-by-hour dose of lactated ringer (LR) to maintain UO at a target range of 30-50 ml/hr [17]. The care providers had the authority to override the recommendation. The dataset included hourly UO and LR dose as well as demographics including age, gender, and weight, total burn surface area (TBSA), the presence of inhalation injury, and the time of arrival. The second source included 53 burn patients. 29 patients were treated with the aid of the same clinical decision support system, while 24 patients were treated with the contemporary resuscitation protocols. The dataset included hourly UO and LR dose as well as demographics including age and weight, TBSA, and the time of arrival (gender and presence of inhalation injury were not known). Collectively, age, weight, and TBSA of the patients in the dataset were 47±18 years, 87±22 kg, and 40±18%, respectively. The overall mortality rate of the patients was 30%. In the first source, 77% of the patients were male and 11% of the patients were associated with inhalation injury.

We randomly split the clinical dataset into training dataset to enhance and optimize the mathematical model (N=120) and test dataset (N=113) to validate the optimized mathematical model after excluding 27 burn injury patients associated with prohibitively small number of UO measurements (≤10). The demographic and injury severity of the burn patients in the training and test datasets were comparable (age: 45±19 years versus 49±18 years; weight: 85±18 kg versus 86±22 kg; TBSA 41.5±17.6% versus 38±18). The average hourly UO measurements in the training and test datasets were 23±2 samples and 20±4 samples, respectively.

4.2 Method: Model Enhancement, Optimization, and Analysis

4.2.1 Method Overview

We conducted the analysis of the clinical dataset to continue to develop, optimize and validate the mathematical model to enable its in-human application. First, we continued to develop the mathematical model (please see chapter 2 and Fig 2.1 for model description and schematic) by (i) including TBSA and weight dependency as well as human-compatible parameters to make it globally applicable to burn injury patients associated with diverse demographic characteristics and injury severity ("Model Enhancement" in Fig. 4.1), and then (ii) optimizing the mathematical model, by systematically reducing the parameter dimension using the training dataset, to make it compatible with sparse clinical measurements ("Model Optimization" in Fig. 4.1). Second, we validated the optimized mathematical model using the test dataset in terms of its predictive capability and physiological plausibility ("Model Analysis" in Fig. 4.1). Third, we scrutinized the mathematical models determined specifically for various categorical patient cohorts to gain insights on meaningful pathophysiological characteristics in these categorical patient cohorts ("Model Analysis" in Fig. 4.1).

Details regarding the continued development, optimization, and analysis of the mathematical model are given in what follows.

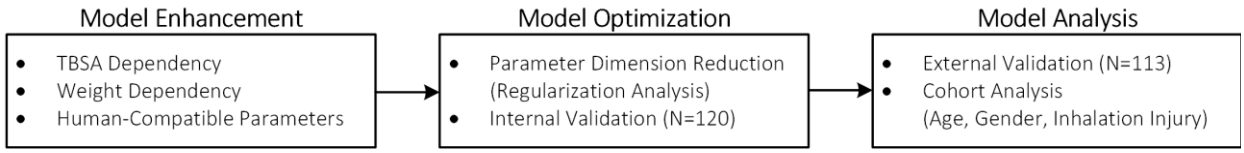

Fig. 4.1: Analysis procedure. (i) The mathematical model was enhanced to enable in-human application by incorporating TBSA and weight dependence and human-compatible parameter values. (ii) The enhanced mathematical model was optimized to enable its use with limited clinical measurements by model fitting analysis with regularization. The optimized model was internally validated using training dataset consisting of 120 burn patients. (iii) The mathematical model was externally validated using testing dataset consisting of 113 burn patients. The mathematical model was analyzed to garner insights on the pathophysiological differences depending on age, gender, and inhalation injury.

4.2.2 Model Enhancement

The clinical dataset presents major challenges in estimating all the parameters in the mathematical model on an individual patient basis. First, the burn patients in the clinical dataset exhibit large variability in the demographic characteristics as well as in the severity of burn injury (TBSA ranging between 16% and 100%), both of which increase the inter-individual variability in physiological responses to burn injury and resuscitation. Second, the number of parameters in the mathematical model is excessively large relative to the available measurements (i.e., hourly resuscitation dose and UO are the only measurements available to characterize these burn patients). To address these challenges and seamlessly apply the mathematical model to real burn patients, we leveraged the training dataset to further develop the mathematical model by (i) expanding it to accommodate the variability in weight, TBSA, and species as well as (ii) systematically reducing the number of parameters to be estimated using the clinical dataset.

First, similar to what we did for sheep subjects, we categorized the total 58 parameters of the model into 34 subject-invariant ("I" in Table 4.3) and 24 subject-specific ("S" and "SS" Table 4.3) parameters.

Second, we improved the mathematical model to accommodate the variability in weight and injury severity in the clinical dataset as well as to increase its suitability to real burn patients. To incorporate the weight dependence into pertinent parameters, we employed a linear allometric relationship by making them linear functions of weight, so that they assume typical values reported in the literature in case of a reference man (70 kg). These parameters include extensive parameters such as the water and protein volumes in the intravascular ($\bar{V}_P$ and $\bar{A}_P$ in Table 4.3), intact tissue ($\bar{\mathrm{V}}_{\mathrm{IT}}$ and $\bar{A}_{IT}$ in Table 4.3), and burnt tissue ($\bar{V}_{BT}$ and $\bar{A}_{BT}$ in Table 4.3) compartments, capillary filtration rate ($\bar{J}_C$ in Table 4.3), and lymphatic drainage ($\bar{J}_L$ in Table 4.3) to list a few. One exception to the linear allometric relationship was the total body surface area (S_B in Table 4.3), which was made a function of weight through the Haycock formula (Eq. (2.32c) in chapter 2) and the weight-height relationship reported in the literature [93]. To incorporate the TBSA dependence into pertinent parameters, we (i) made the extensive parameters associated with the burnt tissue compartment functions of TBSA (ε_B in Table 4.3) and (ii) expanded the plausible ranges of subject-specific parameter values associated with burn-induced pathophysiological responses so that the estimated parameter values avoid saturation at the pre-specified upper and lower bounds. These parameters include those representing the intensity of the inflammatory responses induced by burn injury such as the maximum increase in the capillary pore radius to albumin radius ratio (i.e. pore ratio) in the intact ($M_{\alpha_{IT}}$ in Table 4.3) and burnt ($M_{\alpha_{BT}}$

in Table 4.3) tissue capillary bed, the maximum drop in the burnt tissue hydrostatic pressure ($M_{P_{BT}}$ in Table 4.3), and the maximum increase in the capillary hydrostatic pressure (M_{P_C} in Table 4.3) to list a few. To make the mathematical model (which was initially developed based on the dataset collected from animals in our prior work [40]) more compatible with human burn patients, we refined the values of a number of parameters that are inherently different between animals and humans according to the literature (see Table 4.3 for references). These parameters include nominal albumin concentration in the intravascular ($[\bar{A}_P]$ in Table 4.3), intact tissue ($[\bar{A}_{IT}]$ in Table 4.3), and burnt tissue ($[\bar{A}_{BT}]$ in Table 4.3) compartments, colloid oncotic pressure constant (C_O in Table 4.3), nominal capillary hydrostatic pressure ($\bar{P}_C$ in Table 4.3), and the total body surface area (S_B in Table 4.3).

4.2.3 Optimization and Training

Using the training dataset, we optimized the mathematical model for in-human use by reducing the number of subject-specific parameters that must be estimated on an individual patient basis. As described above, we down-selected 24 subject-specific parameters in the mathematical model that must be estimated using the hourly UO and LR dose measurements. Noting that the information content in the hourly UO and LR dose measurements may not be sufficient to robustly estimate all these 24 parameters, we capitalized on the training dataset to split the subject-specific parameters into parameters sensitive versus insensitive to the LR dose-UO input-output relationship, following our method from chapter 3 which was implemented on sheep data. Then, we

estimated the sensitive subject-specific parameters on an individual patient basis while fixing the insensitive parameters (together with the 34 subject-invariant parameters) at their typical (i.e., group average) values.

First, we determined the typical values of all the 24 subject-specific parameters by fitting the mathematical model to the LR dose-UO measurements pertaining to all the patients in the training dataset based on the pooled approach [70]. This task was accomplished by solving the following optimization problem using a multi-start gradient descent method ("globalsearch" in conjunction with "fmincon") in MATLAB (MathWorks, Natick, MA):

$$\bar{\theta} = arg\,\underset{\theta}{min}\,\bar{J}(\theta) = arg\,\underset{\theta}{min}\sum_{i=1}^{N}\sqrt{\left(\sum_{k=1}^{D_i}\frac{|uo_i^d(t_k)-uo_i(t_k,\theta)|}{UO_i}\right)^2}, \tag{4.1}$$

where $\bar{\theta}$ is the vector of typical values of subject-specific parameters, θ is the vector of 24 subject-specific parameters (i.e., a vector containing the 24 subject-specific parameters in Table AI), N is the number of subjects, D_i is the number of UO measurements for the subject i during the treatment, $uo_i^d(t_k)$ is the value of UO associated with the subject i measured at time t_k, $uo_i(t_k,\theta)$ is the value of UO associated with the subject i at time t_k predicted by the mathematical model for a given θ, and UO_i is the normalization factor for UO associated with the subject i, which is defined as the range of uo_i^d multiplied by D_i. Note that this is exactly similar to Eq. (3.1) from previous chapter, the difference being that there we had multiple variables to fit our predictions to, and here we only have the UO.

Second, we classified the subject-specific parameters into sensitive and insensitive groups by quantifying and comparing the degree of inter-individual variability

associated with all the subject-specific parameters. This task was accomplished by solving the following optimization problem for fitting with regularization [72] on an individual patient basis using a multi-start gradient descent method ("globalsearch" in conjunction with "fmincon") in MATLAB (MathWorks, Natick, MA):

$$\theta_i = arg\,\underset{\theta}{min}\,J_i(\theta) = arg\,\underset{\theta}{min}\sqrt{\left(\sum_{k=1}^{D_i}\frac{|uo_i^d(t_k)-uo_i(t_k,\theta)|}{UO_i}\right)^2} + \lambda_p\sum_{l=1}^{24}\left|\frac{\theta(l)-\bar{\theta}(l)}{\Theta_l}\right|, \quad (4.2)$$

where θ_i is the vector of 24 subject-specific parameters associated with the subject i, λ_p is the regularization weight, and Θ_l is the normalization factor for the l-th element $\theta(l)$ of θ, which was defined so that all the elements in θ are homogeneously ranged approximately between 0 and 1. The subset of subject-specific parameters exhibiting deviations from the typical values in many subjects may be viewed as subject-specific parameters sensitive to the LR dose-UO input-output relationship. We selected sensitive subject-specific parameters as those whose deviations exceeded a threshold value when averaged across all the 120 patients in the training dataset.

Third, we ascertained the ability of the mathematical model (with the chosen sensitive subject-specific parameters) to faithfully replicate the UO responses to the LR dose in the training dataset, as well as its physiological plausibility. To this aim, we estimated the sensitive subject-specific parameters by solving the following optimization problem on an individual patient basis using a multi-start gradient descent method ("globalsearch" in conjunction with "fmincon") in MATLAB (MathWorks, Natick, MA) while fixing the remaining (insensitive subject-specific and subject-invariant) parameters at the respective typical values:

$$\breve{\theta}_i = arg\,\underset{\breve{\theta}}{min}\,\breve{J}_i(\breve{\theta}) = arg\,\underset{\breve{\theta}}{min}\sqrt{\left(\sum_{k=1}^{D_i}\frac{|uo_i^d(t_k)-y_i(t_k,\breve{\theta})|}{UO_i}\right)^2} \tag{4.3}$$

where $\breve{\theta}$ is the vector of sensitive subject-specific parameters selected by solving Eq. (4.2) (i.e., it is a subset of θ), and $\breve{\theta}_i$ is $\breve{\theta}$ estimated for the subject i. Then, we examined the faithfulness of the mathematical model in terms of (i) normalized mean absolute error (NMAE) [40], (ii) correlation coefficient, and (iii) UO range agreement, all between measured versus model-replicated UO on an individual patient basis, and (iv) Bland-Altman statistics between all measured versus model-replicated UO. We computed the UO range-based agreement by specifying UO ranges of interest and then for each range computing the percentage of actual UO in the range whose model-predicted UO also resides in the same range. In addition, we examined the physiological plausibility of the mathematical model in terms of (i) both typical and subject-specific model parameter values (e.g., by comparing them with the values reported in the existing literature) as well as (ii) the plausibility of the volume kinetic and kidney function responses predicted by the mathematical model equipped with typical parameter values. We repeated the above procedure to optimize the mathematical model (i.e., Eq. (4.1)-(4.3)) so that it can yield a minimal number of sensitive subject-specific parameters and adequate faithfulness and physiological plausibility.

Using the test dataset, we externally validated the faithfulness and physiological plausibility of the optimized mathematical model on an individual patient basis, in terms of the same metrics used above.

4.2.4 Cohort-Specific Optimization

In addition to the optimization and validation of the mathematical model for in-human application, we also sought to garner in-depth insights and expand the knowledge on burn pathophysiology using the mathematical model. In particular, existing literature suggests that patients who are older [88], female [89]–[91], and associated with inhalation injury [88], [94], as well as those who are associated with severe burn injury [88] and/or receive delayed treatment [95] have a higher risk of mortality. The mathematical model already incorporates TBSA and arrival time post-burn, thereby allowing it to predict more severe responses to burn injury associated with large TBSA and delayed resuscitation treatments. However, it does not explicitly account for the effect of age, gender, and inhalation injury.

To investigate if the mathematical model can elucidate the age-, gender-, and inhalation injury-dependent differences in the burn physiological and pathophysiological mechanisms, we fitted the (optimized and validated) mathematical model separately to (i) younger versus older patients, (ii) female versus male patients, and (iii) patients with versus without inhalation injury. We used the patients in the training dataset (N=120), since they were associated with consistent treatment durations (i.e., 24 hours monitoring in most patients) compared to the test dataset. We excluded 16 patients since they did not have gender specification. We defined older patients as those with an age above the median age of the 104 patients (45 years), and younger patients otherwise. Using these 104 patients in the training dataset, we built the group-average mathematical models associated with younger (N=52) versus older (N=52) patients, (ii) female (N=22) versus male (N=82) patients, and (iii) patients with

(N=11) versus without (N=93) inhalation injury, all by solving a hybrid of the optimization problems in Eq. (4.1) and Eq. (4.3) (specifically, solving Eq. (4.1) only with respect to sensitive subject-specific parameters rather than all the sensitive parameters) based on the dataset associated with the specific patient groups. Then, we examined if the model parameter values for the two groups in each of the three categories (age, gender, and inhalation injury) exhibited meaningful contrasting differences that provide clinically important physiological insights.

4.3 Results

The iterative optimization of the mathematical model using the training dataset resulted in a mathematical model with seven sensitive subject-specific parameters in total, including the nominal capillary pore radius to albumin radius ratio ($\bar{\alpha}$), the maximum increase in the pore ratio in the intact ($M_{\alpha_{IT}}$) and the burnt ($M_{\alpha_{BT}}$) tissue capillary bed, the maximum increase in the capillary hydrostatic pressure (M_{P_C}), the slow decay rate associated with the increase in the capillary hydrostatic pressure (λ_{1,P_C}), the tubule-glomerular feedback sensitivity (K_{TGF}), and the nominal water reabsorption rate in the collecting ducts ($\bar{J}_{RR,ADH}$). Table 4.1 summarizes NMAE, correlation coefficient, UO range-based agreement pertaining to < 30, 30< <50, and >50 ml/h, or <0.5, 0.5< <1, and >1 ml/kg·hr, and the Bland-Altman statistics (i.e., the limits of agreement), all associated with the optimized mathematical model. Fig. 4.2 presents examples of actual versus model-predicted UO responses associated with eight patients with various burn injury severity in the test dataset (details discussed in section 4.4.1). Fig. 4.3 presents volume kinetic and kidney function responses to burn injury and burn

resuscitation predicted by the group-average mathematical model in response to group-average burn resuscitation LR dose (details discussed in sections 4.4.1 and 4.4.2).

Fig. 4.4 shows the weight-normalized PV, intravascular water gain (LR dose) and loss

Table 4.1: Normalized mean absolute error (NMAE: median (IQR)), correlation coefficient (r value), Bland-Altman statistics (bias±2×SD), and range-based agreement (median (IQR)) associated with urinary output (UO) prediction by the mathematical model.

	Training Dataset (N=120)	Test Dataset (N=113)
NMAE [%]	14.8 (6.0)	15.4 (6.0)
Correlation Coefficient (r Value)	0.67	0.82
Limits of Agreement [ml/hr]	-3±57	+2±45
UO Range-Based Agreement [%] (< 30, 30< <50, and >50 ml/h)	78 (15)	83 (14)
UO Range-Based Agreement [%] (<0.5, 0.5< <1, and >1 ml/kg·h)	90 (16)	92 (16)

(capillary filtration in excess of lymphatic flow), and the burn resuscitation effectiveness (defined as the weight-normalized intravascular water gain rate (i.e., LR dose minus capillary filtration in excess of lymphatic flow) divided by the weight-normalized LR dose) throughout the 24-hour treatment period as predicted by the group-average mathematical model (details discussed in section 4.4.2). Table 4.2 summarizes (i) demographics, (ii) statistical characteristics of fluid retention and UO relative to its treatment target range (30-50 ml/hr), and (iii) group-average model parameter values related to burn-induced inflammatory perturbations, all associated with the two patient groups in the three categories (details discussed in section 4.4.3).

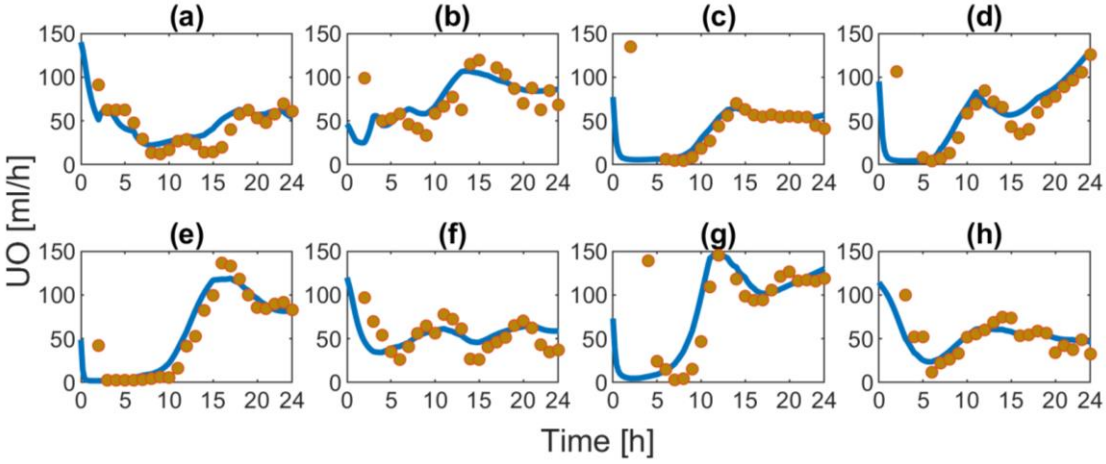

Fig. 4.2: Actual versus model-predicted urinary output (UO) responses of eight burn patients associated with various injury severity and weight. Circles: actual UO. Solid lines: model-predicted UO. (a) TBSA 27% with 80 kg weight. (b) TBSA 36% with 66 kg weight. (c) TBSA 46% with 90 kg weight. (d) TBSA 60% with 71 kg weight. (e) TBSA 24% with 81 kg weight. (f) TBSA 35% with 94 kg weight. (g) TBSA 50% with 89 kg weight. (h) TBSA 60% with 102 kg weight.

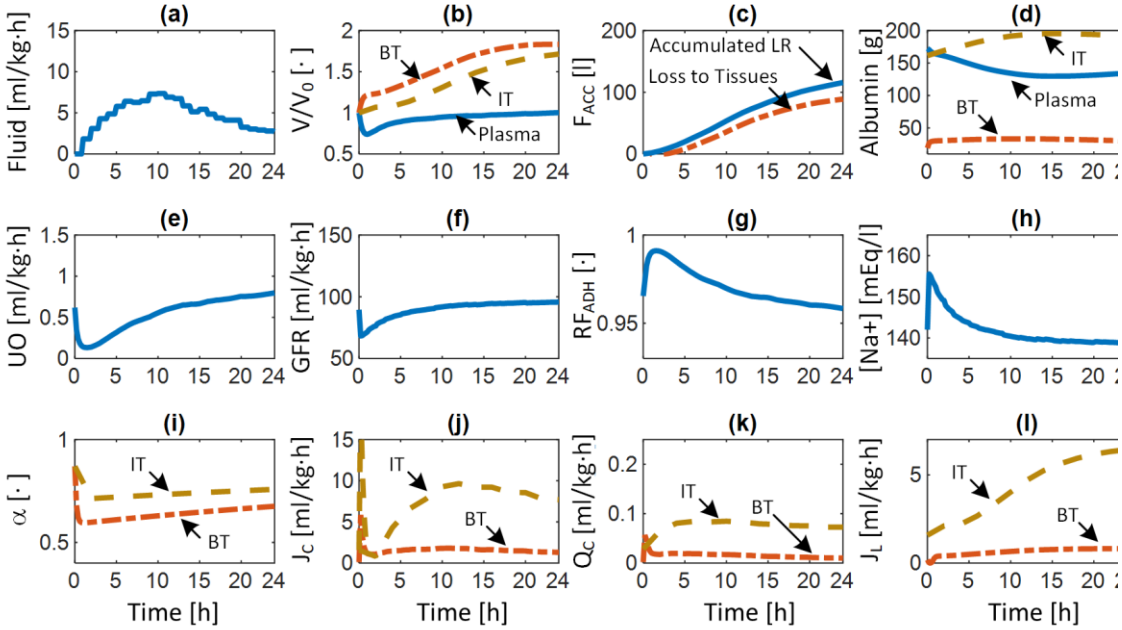

Fig. 4.3: Volume kinetic and kidney function responses to burn injury and burn resuscitation during initial 24 hours post-burn, predicted by the group-average mathematical model. V/V_0: water volume relative to its initial value. F_{ACC}: accumulated fluid. RF_{ADH}: reabsorption fraction due to ADH, α: capillary pore radius ratio. J_C: capillary filtration. Q_C: albumin transport across the capillary wall. J_L: lymphatic flow. (b) and (d): Blue solid, brown dashed, and orange dash-dot lines correspond to plasma, intact tissues, and burnt tissues, respectively. (c): Blue solid and orange dash-dot lines are weight-normalized accumulated resuscitation LR volume and water loss to tissues (i.e., capillary filtration in excess of lymphatic flow), respectively. (i)-(l): Brown dashed, and orange dash-dot lines correspond to intact and burnt tissues, respectively. IT: intact tissues. BT: burnt tissues.

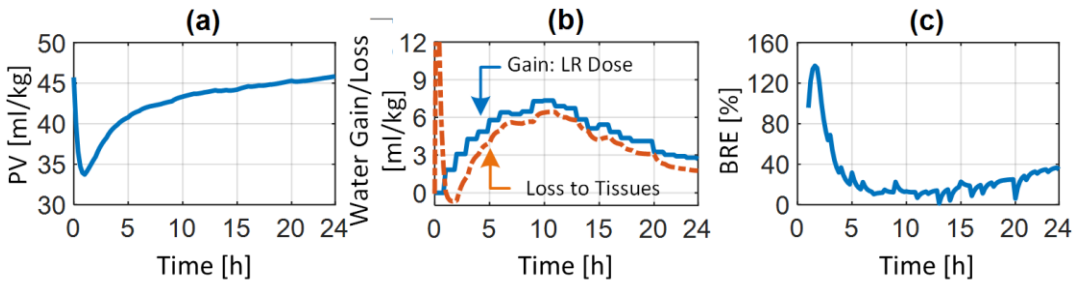

Fig. 4.4: Group-average prediction of (a) weight-normalized plasma volume (PV), (b) weight-normalized intravascular water gain (LR dose: blue solid) and loss (capillary filtration minus lymphatic flow: orange dashed) rates, and (c) burn resuscitation effectiveness (BRE).

4.4 Discussion

Developing treatment strategies and expanding knowledge associated with burn injury present formidable challenges due to its complex pathophysiology, large inter-patient variability, and its less common incidence compared to other widespread injuries despite its devastating impact on the mortality and the quality of life. High-fidelity mathematical models capable of replicating volume kinetic and kidney function responses to burn injury and resuscitation has the potential to advance both treatment development and knowledge expansion aspects of burn resuscitation. Regardless, to the best of our knowledge, no mathematical model exists that has been developed and extensively (and publicly) validated using clinical datasets from real burn patients. In this paper, we present our continued development, extensive in-human validation, and analysis of a mathematical model for the study of burn injury and resuscitation, which is equipped with contemporary knowledge on the burn-related physiology and pathophysiology.

4.4.1 In-Human Credibility

The enhanced/optimized mathematical model based on the training dataset exhibited adequate predictive capability for UO response to burn injury and resuscitation in both training and test datasets (Table 4.1 and Fig. 4.2). In particular, the mathematical model worked equally well in both training and test datasets, both in terms of average statistics and robustness (e.g., NMAE was 15% with small IQR of 6%; Table 4.1). Further, it could capture the physiological differences in burn patients across diverse TBSA range, including those associated with comparable weight ((a) versus (e) and (c) versus (g) in Fig. 4.2) and those associated with distinct weight ((b) versus (f) and (d) versus (h) in Fig. 4.2). In addition, the mathematical model showed a high degree of UO range-based agreement (>90% (when weight-normalized) and >78% (when not weight-normalized) of model-predicted UO resided in the same range to actual UO; Table 4.1). Noting that existing burn resuscitation protocols determine the hourly resuscitation dose based on the range of UO, the results suggest that the mathematical model may serve as a valuable platform for non-clinical testing of burn resuscitation protocols and algorithms.

In addition to UO, the mathematical model was able to predict the overall volume kinetic and kidney function responses to burn injury and resuscitation in a realistic way: the behaviors of the internal volume kinetic and kidney variables were consistent with the contemporary knowledge on burn pathophysiology as well as findings from recent studies (Fig. 4.3). Specifically, the group-average mathematical model predicted that (i) plasma volume and UO showed an anticipated trend of initial decline upon the onset of burn injury and subsequent recovery with the initiation of burn resuscitation and

later with the return of resuscitation fluid leaked into the tissues back to the blood (Fig. 4.3(b), Fig. 4.3(c), and Fig. 4.3(e)) [74], [96]; (ii) burnt and intact tissue volumes increased up to nearly twice their initial values, peaking and starting to decay approximately at 24 hours post-burn (Fig. 4.3(b)) [8], [9], [97]; (iii) plasma albumin was transported into burnt and intact tissues due to the perturbations in albumin reflection and permeability-surface area coefficients (Fig. 4.3(d) and Fig. 4.3(k)) triggered by burn-induced increase in the capillary pore size that decreased the capillary pore radius ratio in both burnt and intact tissue (Fig. 4.3(i)) [57]; (iv) GFR increased just a few hours post-burn even before plasma volume (Fig. 4.3(f)) [76]; and (v) sodium concentration decreased after burn injury and resuscitation (Fig. 4.3(h)) [78].

Importantly, the mathematical model could predict UO as well as physiologically plausible volume kinetic and kidney function responses once physiologically acceptable values were assigned to its parameters. In fact, the majority of the parameters equipped with physiological implications assumed values comparable to typical values and/or those reported in the literature both on the individual and population-average basis (Table 4.3).

In sum, we demonstrated that the mathematical model can faithfully replicate the volume kinetic and kidney function responses in a wide range of burn patients, both in terms of the adequacy of the model-predicted responses and the plausibility of the model parameter values.

4.4.2 Insights on Burn Resuscitation Effectiveness

One strength of the mathematical model presented in this paper is its ability to replicate overall responses of a burn patient to injury and resuscitation, including those that

cannot be clinically measured. Exploiting this advantage, we sought to garner insights on the effectiveness of burn resuscitation in a typical patient subject to burn injury. It is known that the homeostasis in volume kinetics is severely disrupted after burn injury due to the activation of multiple inflammatory mediators, which in turn causes a large portion of the resuscitation fluid to leak out of the intravascular compartment via capillary filtration. Although this leakage is partially recovered by the increase in lymphatic flow, >50% of the resuscitation fluid can leak out of the intravascular compartment in the initial hours post-burn in extensive burn injury [12], [98]. In this regard, burn resuscitation effectiveness represents the portion of the resuscitation fluid actually used to expand plasma volume. Based on the investigation and interpretation of >50 physiological variables including those presented in Fig. 4.3 and Fig. 4.4, we could garner the following insights on the important physiological and pathophysiological mechanisms responsible for the effectiveness of burn resuscitation during the initial 24 hours post-burn. Initially, there is a large and fast fluid shift from the blood to the intact and burnt tissues immediately after burn injury for up to one hour, leading to a large decrease in the plasma volume (Fig. 4.3(j) and Fig. 4.4(a)). Our mathematical model suggests that major mechanisms responsible for this initial loss of plasma volume may be negative hydrostatic pressure, protein denaturation in burnt tissues, and systemic increase in the capillary hydrostatic pressure. After this initial phase, a decrease in the capillary filtration followed by self-regulation of plasma volume occurs for up to one hour. Our mathematical model suggests that major mechanisms responsible for this phase may be the reduction in the plasma volume and the resulting decrease in the capillary hydrostatic pressure, the recovery of hydrostatic

pressure in the burnt tissues, and the increase in the lymphatic flow (Fig. 4.3(l)). The effectiveness of burn resuscitation during this phase is very high (>100%), meaning that plasma volume is expanded based on almost all the resuscitation fluid as well as the fluid returning from the edematous (burnt and intact) tissues (Fig. 4.4(c)). Subsequently, burn resuscitation effectiveness deteriorated quickly as the capillary filtration of water and protein increases again due to the opened capillary pores (Fig. 4.3(i)) and the increase in the plasma volume. Our mathematical model suggests that major mechanisms responsible for this phase may include the increase in the protein concentration in both burnt and intact tissues as well as the hypoproteinemia in the blood (Fig. 4.3(d)), which altogether increase the osmotic pressure gradient toward tissues and promote capillary filtration of both water and protein (thereby forming a vicious circle). Burn resuscitation effectiveness reaches its minimum level of 2%-15% at 10-15 hours after the initiation of treatment, which is in close agreement with the literature suggesting maximal edema formation in this period post-burn [8]. Finally, burn resuscitation effectiveness increases back to approximately 40% at 24 hours after the initiation of treatment. Our mathematical model suggests that major mechanisms responsible for this recovery may include the recovery of lymphatic flow to return excessive water and protein to the blood as well as the gradual decrease in the capillary pore size, which altogether decreases the fluid extravasation rate.

Table 4.2: Demographics, characteristics of fluid resuscitation, fluid retention, and urinary output (UO) relative to its treatment target range (30-50 ml/hr), and group-average model parameter values related to burn-induced inflammatory perturbations, all associated with the two patient groups in (a) age (younger versus older patients), (b) gender (female versus male patients), and (c) inhalation injury (patients with versus without inhalation injury) categories. Fluid retention is computed as the total resuscitation fluid (LR) volume minus the total UO during the 24 hours of treatment. Fluid resuscitation and fluid retention are shown in mean±SD, while UO is shown in median (IQR). $M_{\alpha_{BT}}$, $M_{\alpha_{IT}}$, and M_{P_C} are group-average values of burn-induced inflammatory perturbation parameters in the mathematical model.

(a) Age

	Older (N=52)	Younger (N=52)
Weight [kg]	84 (15)	86 (21)
Injury Severity (TBSA) [%]	38 (17)	44 (17)
Mortality Rate [%]	42	18
Fluid Resuscitation [ml/kg·%]	4.20±1.59	3.27±1.18
Fluid Retention [ml/kg·%]	3.75±1.6	2.78±1.16
30 ml/hr≤UO≤50 ml/hr	23 (16)	26 (15)
UO<30 ml/hr	34 (20)	21 (14)
UO>50 ml/hr	42 (20)	53 (18)
$M_{\alpha_{BT}}$	0.54	0.23
$M_{\alpha_{IT}}$	0.19	0.19
M_{P_C}	1.70	0.05

(b) Gender

	Female (N=22)	Male (N=82)
Weight [kg]	74 (17)	88 (17)
Injury Severity (TBSA) [%]	38 (13)	43 (19)
Mortality Rate [%]	37	27
Fluid Resuscitation [ml/kg·%]	4.0±1.24	3.67±1.52
Fluid Retention [ml/kg·%]	3.43±1.2	3.2±1.5
30 ml/hr≤UO≤50 ml/hr	28 (14)	24 (16)
UO<30 ml/hr	32 (15)	26 (20)
UO>50 ml/hr	40 (16)	50 (20)
$M_{\alpha_{BT}}$	0.32	0.48
$M_{\alpha_{IT}}$	0.16	0.15
M_{P_C}	2.26	1.73

(c) Inhalation Injury

	Injury (N=11)	No Injury (N=93)
Weight [kg]	77 (15)	86 (18)
Injury Severity (TBSA) [%]	46 (14)	41 (18)
Mortality Rate [%]	40	29
Fluid Resuscitation [ml/kg·%]	4.33±1.19	3.66±1.49
Fluid Retention [ml/kg·%]	3.9±1.2	3.0±1.5
30 ml/hr≤UO≤50 ml/hr	24 (16)	24 (15)
UO<30 ml/hr	31 (23)	27 (18)
UO>50 ml/hr	44 (19)	48 (20)
$M_{\alpha_{BT}}$	0.52	0.31
$M_{\alpha_{IT}}$	0.19	0.18
M_{P_C}	1.47	0.13

4.4.3 Cohort-Dependent Differences in Burn Pathophysiology

The analysis of datasets associated with various categorical patient cohorts (with respect to age, gender, and inhalation injury) provided meaningful insights on the cohort-dependent differences in burn physiology and pathophysiology (Table 4.2). To begin with, the mathematical model was able to replicate UO response to burn injury and resuscitation associated with all the categorical patient cohorts (younger versus older, female versus male, and patients with and without inhalation injury).

First, between younger versus older patients, the latter had much higher mortality rate and higher portion of UO responses below the target therapeutic range than the former despite its smaller group-average TBSA and higher level of weight-normalized LR dose, which leads to higher fluid retention in the latter (Table 4.2(a)). Comparing the mathematical models fitted to younger versus older burn patients, the latter was

associated with higher inflammation factors (including the larger increase in capillary pore size in the burnt tissues ($\mathrm{M}_{\alpha_{\mathrm{BT}}}$) and the capillary hydrostatic pressure ($\mathrm{M}_{\mathrm{P_C}}$)). Second, between patients with versus without inhalation injury, the former likewise had >1.3 times higher mortality rate and higher portion of UO responses below the target therapeutic range than the latter (Table 4.2(c)). Comparing the mathematical models fitted to burn patients with versus without inhalation injury, the former exhibited higher inflammation factors (including the larger increase in capillary pore size ($M_{\alpha_{IT}}$ and $M_{\alpha_{BT}}$) and capillary hydrostatic pressure (M_{P_C})) similarly to the older patient cohort. Existing literature shows the possible association between fluid retention and edema versus mortality and complication rates in burn patients [77]. In addition, both literature and our dataset indicate higher fluid retention and edema as well as higher mortality rates in older patients and patients with inhalation injury [99], [100]. From this standpoint, our mathematical model analysis predicts that higher inflammation may be a key contributing factor in increasing the mortality risk of older patients and patients with inhalation injury via an increase in fluid retention. Our prediction is in fact consistent with the contemporary knowledge in the literature identifying inflammation as an important mediator of increased fluid retention and edema, and higher mortality rate in older patients [101], [102] and patients with inhalation injury [103], [104], although other causes can play a role (e.g., degraded cardiovascular efficiency in elderly burn patients [105]). Although our mathematical model analysis reveals possible mechanisms responsible for higher mortality rate, the exact cause is yet to be clearly elucidated. Regardless, lower burn resuscitation effectiveness in older patients and patients with inhalation injury relative to younger

patients and patients without inhalation injury remains true, and our mathematical model was able to replicate the age- and inhalation injury-dependent differences in burn resuscitation effectiveness. Hence, our mathematical model may serve as an effective basis to develop and validate burn resuscitation protocols and algorithms suited to these categorical patient cohorts.

Third, between female and male patients, neither the dataset nor the mathematical model showed any meaningful difference in terms of inflammation and fluid retention (Table 4.2(b)). This contrasts against some literature identifying the female gender as a mediator of mortality risk associated with burn injury, as confirmed by our dataset (1.3 times the mortality rate in males). Hence, our mathematical model analysis suggests that higher mortality risk in female burn patients may be attributed to factors other than an increase in the inflammation and the corresponding increase in the fluid retention, especially those not manifested in the initial 24 hours post-burn. In fact, a prior study performed on mice showed that the difference in the inflammatory responses in female and male subjects was not clear until 6 days post-burn [106]. The exact mechanisms responsible for the gender difference in burn-induced mortality risk are still unknown and must be unveiled.

4.5 Conclusions

The main outcome of this chapter is a physiologically plausible mathematical model capable of replicating volume kinetic and kidney function responses to burn injury and resuscitation suited to in-human application. To the best of our knowledge, the mathematical model presented in this work may be the first of its kind developed and

extensively validated using large clinical datasets from real burn patients. We anticipate that the mathematical model may provide an attractive platform to conduct non-clinical testing of burn resuscitation protocols and test new hypotheses on burn pathophysiology.

In future we plan to investigate the potential of our mathematical model as medical digital twin for disciplined development and rigorous stress testing of emerging burn resuscitation algorithms and as a cornerstone to expand our understanding of burn injury.

4.6 Model Parameters: Nomenclature, Definitions, and Values

Table 4.3: Mathematical model parameters: definitions, categories (I/S/SS), and values. I: subject-invariant parameters. S: subject-specific parameters. SS: sensitive subject-specific parameters. Parameter values are given as mean, median (IQR), or mean+/-SD.

Symbol	Definition	I/ S	Value (Model)	Value (Literature)
$\bar{V}_P$	Nominal water volume in plasma [ml/kg]	I	42.8	42 [81]-46 [36]
r_{FV}	Skin fluid volume to total interstitial fluid volume ratio [·]	I	0.28	0.28 [36]
$\bar{V}_{BT}$	Nominal water volume in burnt tissue [ml/kg]	I	$120\varepsilon_B r_{FV}$	$120\varepsilon_B r_{FV}$ [36]
$\bar{V}_{IT}$	Nominal water volume in intact tissue [ml/kg]	I	$120(1-\varepsilon_B r_{FV})$	$120(1-\varepsilon_B r_{FV})$ [36]
$[\bar{A}_P]$	Nominal albumin concentration in plasma [g/ml]	I	0.045	0.035-0.045 [107]
$[\bar{A}_{BT}]$	Nominal albumin concentration in burnt tissue [g/ml]	I	0.018	0.013 [108]-0.016 [36]
$[\bar{A}_{IT}]$	Nominal albumin concentration in intact tissue [g/ml]	I	0.018	0.013 [108] -0.016 [36]
$\bar{A}_P$	Nominal albumin content in plasma [g]	I	$[\bar{A}_P]\bar{V}_P$	-
$\bar{A}_{BT}$	Nominal albumin content in burnt tissue [g]	I	$[\bar{A}_{BT}]\bar{V}_{BT}$	-
$\bar{A}_{IT}$	Nominal albumin content in intact tissue [g]	I	$[\bar{A}_{IT}]\bar{V}_{IT}$	-
$\bar{J}_C$	Nominal capillary filtration [ml/kg·h]	S	1.76	1.72 [79]
C_O	Colloid oncotic pressure constant [mmHg/g·ml]	I	609	657 [36]
$\bar{J}_L$	Nominal total lymphatic flow to plasma [ml/kg·h]	I	1.76	1.07 [37]-2.9 [109]
$\bar{J}_{L,BT}$	Nominal lymphatic flow from burnt tissue to plasma [ml/kg·h]	I	$\bar{J}_L\varepsilon_B r_{FV}$	$\bar{J}_L\varepsilon_B r_{FV}$ [36]
$\bar{J}_{L,IT}$	Nominal lymphatic flow from intact tissue to plasma [ml/kg·h]	I	$\bar{J}_L(1-\varepsilon_B r_{FV})$	$\bar{J}_L(1-\varepsilon_B r_{FV})$ [36]
C_L	Lymphatic maximal increase coefficient [·]	S	0.07	-
S_L	Lymphatic pressure sensitivity coefficient [1/mmHg]	S	1.2	-
$\bar{P}_C$	Nominal capillary hydrostatic pressure [mmHg]	S	16.3	13 [110]- 24 [8]
E_C	Capillary elastance [mmHg/ml]	S	0.0084	0.0097 [37]
α	Tissue electrostatic pressure coefficient [mmHg]	I	10	10 [45]
γ	Tissue tension pressure coefficient [mmHg]	I	3.75	3.75 [45]
$\hat{y}$	Maximum half-thickness of the extracellular matrix [·]	I	4	4 [45]

$\check{y}$	Minimum half-thickness of the extracellular matrix [·]	I	1	1 [45]
$\hat{R}$	Maximum GAG radius [·]	I	3.5	3.5 [45]
β	Radius threshold ratio [·]	I	0.23	0.23 [45]
n	Hydration response coefficient [·]	I	8	2-8 [45]
$\bar{W}_X$	Nominal hydration level [ml/g]	I	0.66	0.23-0.81 [45], [46]
$\bar{J}_{RPF}$	Nominal renal plasma flow [ml/kg·h]	I	536	536 [111]
τ_{TGF}	Tubuglomerular feedback time constant [1/h]	S	0.35	-
K_{TGF}	Tubuglomerular feedback sensitivity [·]	SS	1.45 (0.4)	-
$\bar{R}_G$	Nominal glomerular resistance [mmHg/ml/kg·h]	I	9.05	-
λ_G	Glomerular hydrostatic pressure sensitivity [mmHg^2/(ml/h·kg)^2]	I	1	-
P_B	Hydrostatic pressure in Bowman's capsules [mmHg]	I	18	18 [47]
K_G	Glomerular filtration coefficient [ml/kg·h·mmHg]	S	9.2 (1.2)	9.6-12.0 [84]
K_{ADH}	Nominal ADH secretion rate [pg/kg·h]	I	287	287 [54], [55]
λ_{V_P}	ADH sensitivity to plasma volume change [1/ml]	S	0.0011	-
$\lambda_{[Na^+]}$	ADH sensitivity to sodium concentration change [l/mEq]	S	0.085	-
K_{RR}	Maximum collecting duct reabsorption fraction [·]	I	0.999	-
$\overline{[ADH]}$	Nominal ADH concentration [pg/ml]	I	1	0-5 [112]
$[ADH]_{50}$	ADH concentration corresponding to $\frac{1}{2}K_{RR}$ [pg/ml]	S	0.0594	-
$\overline{[Na^+]}$	Nominal plasma sodium concentration [mEq/l]	I	142	142 [85]
$\bar{J}_{RR,ADH}$	Nominal water reabsorption rate in the collecting ducts [·]	SS	0.955 (0.01)	0.97 [51]
$\hat{Q}_{PD}$	Protein influx post burn [g/h]	S	85.8	-
λ_{PD}	Protein influx decay rate [1/h]	S	10	-
$M_{P_{BT}}$	Maximum burnt tissue hydrostatic pressure perturbation [mmHg]	S	56	20-270 [56]
$\lambda_{1,P_{BT}}$	Burnt tissue hydrostatic pressure perturbation slow decay rate [1/h]	S	6.88	-
μ	The ratio between slow decay rate to fast decay rate [·]	S	365	-
$\lambda_{2,P_{BT}}$	Burnt tissue hydrostatic pressure perturbation fast decay rate [1/h]	I	$8\lambda_{1,P_{BT}}$	-
$K_{1,EV}$	Nominal tissue evaporation rate [ml/h·m^2]	I	18.48	18.48 [63]
$\lambda_{1,EV}$	Evaporation growth rate [1/h]	I	0.073	0.073 [63]
$K_{2,EV}$	Maximum evaporation rate [ml/h·m^2]	I	28.68	28.68 [63]
$\lambda_{2,EV}$	Evaporation decay rate [1/h]	I	-0.0052	-0.0052 [63]
ε_B	Fraction of body surface subject to burn [·]	S	0.16-1	dataset
K_{EX}	Maximum exudation rate [ml/h·m^2]	I	25	25 [62]
λ_{EX}	Exudation decay rate [1/h]	I	-0.0038	-0.0038 [62]
η_{EX}	Exudate to tissue albumin ratio [·]	S	0.60	0.75 [36]
$\bar{\alpha}$	Nominal albumin to capillary pore radius ratio [·]	SS	0.83 (0.9)	0.7-0.9 [37]
$1-k_{PD,BT}$	Capillary destruction fraction for burnt tissue [·]	S	0.47	0.50 [35]
$1-k_{PD,IT}$	Capillary destruction fraction for intact tissue [·]	I	0	-
$M_{\alpha_{BT}}$	Maximum pore ratio perturbation in burnt tissue [·]	SS	0.27 (0.08)	0.30 [39]
$M_{\alpha_{IT}}$	Maximum pore ratio perturbation in intact tissue [·]	SS	0.21 (0.08)	0.19 [87]
$\lambda_{1,\alpha}$	Pore ratio slow decay rate [1/h]	S	0.015	0.025 [36]
$\lambda_{2,\alpha}$	Pore ratio fast decay rate [1/h]	I	$\mu\lambda_{1,\alpha}$	-
M_{P_C}	Maximum capillary hydrostatic pressure perturbation [mmHg]	SS	18.62 (17)	23 (5) [61]
λ_{1,P_C}	Capillary hydrostatic pressure perturbation slow decay rate [1/h]	SS	0.51 (0.33)	-
λ_{2,P_C}	Capillary hydrostatic pressure perturbation fast decay rate [1/h]	I	$\mu\lambda_{1,P_C}$	-

Chapter 5: Expanding the Model: Introducing a Cardiovascular Model, a Detailed Renal Function Model, and a Renin-Angiotensin-Aldosterone Model

5.1 Motivation for Change

Although the predictions of the original renal function model are consistent with the experimental data and literature in its current form, we could potentially lift some of the simplifying assumptions by diving deeper into physiology to increase the physical transparency of the model. This attempt is particularly relevant to the renal function model and its several phenomenological components, which we will elaborate on in this chapter.

Additionally, there are opportunities to improve the model by adding modules that are of clinical interest, and for which we have unutilized experimental data. One such opportunity is the addition of a cardiovascular component. While in this work we are more interested in volume kinetics, from a clinical standpoint, cardiovascular variables such as cardiac output (CO), mean arterial pressure (MAP), and central venous pressure (CVP) are of great importance. The primary purpose of resuscitation in burn injury and many other forms of shock-inducing trauma is to restore sufficient tissue perfusion, which is often determined by CO, or a combination of vital signs including CO and MAP [113]–[115]. Therefore, although, as mentioned in chapter one, in more than 94% of burn centers, UO, which is easily and non-invasively measured, is used to guide burn resuscitation, its limitations in estimating tissue perfusion as a single variable are well-known, and there is a recent interest to combine hemodynamic monitoring and other

endpoints with UO for optimal resuscitation [116]–[118]. Thus, having validated predictions of cardiovascular variables alongside UO and volume kinetics predictions could be undeniably valuable to the clinical applications of our mathematical model.

Moreover, in the original model, we have often used PV in place of CO and MAP, for instance, to calculate the renal arterial pressure or the rate by which the liver metabolizes a hormone. Updating these simplifying assumptions by replacing PV with estimations of the actual variables could improve our predictions while being more consistent with the physiological principles. Fortunately, the sheep data used for animal training and validation in chapter three has rich measurements of CO, MAP, and CVP, that we could use to identify and validate the CV model. The motivation to add a CV model was reinforced by the addition of a new dataset, 15 porcine subjects with 40% burn injury, introduced and used in chapter six, that also have CO, MAP, and CVP measurements.

One of the key mechanisms for long-term volume, electrolyte, and pressure regulation in the body, is the renin-angiotensin-aldosterone system (RAAS). RAAS is also a bridge between the renal function and the CV model, as we will see in section 5.4. Due to its relevance to VK, renal function, and CV components, the other module that we added to the expanded version of the model is the RAAS. Adding the RAAS both entails and facilitates the inclusion of a more accurate description of the sodium dynamics in the body, which we will proceed to do in the new formulation of the kidney function model.

5.2 Cardiovascular Model: Considerations and Formulation

Mathematical modeling of the cardiovascular system has been an attractive research topic for a long time due to its incredible complexity and multiscale nature, i.e., it has different mechanisms for both short- and long-term regulations. Additionally, since most CV models don't have analytical solutions, the need to develop efficient computational methods to identify the CV model; makes this topic both a physiological and a mathematical challenge. [119].

There is a long list of mechanistic and data-driven models of the CV model in literature to choose from as a basis for the development of a CV model compatible and relevant to our burn injury and resuscitation model [72], [120]–[126]. In this context, we can summarize our selection criteria to 1) simplicity and 2) the potential to support long-term predictions.

1) Simplicity: to connect the CV model to the burn model and benefit from its clinical uses, we only need CO, MAP, and CVP predictions, which we can validate using our experimental data. Considering the intrinsic complexity of the burn model, we needed to minimize the added computational cost and likelihood of overfitting. Therefore, we eliminated the detailed mathematical models of the CV system with tens of tunable parameters that generated variables not relevant to our context of use from the list of candidate models. [121], [123], [125].
2) The potential to support long-term predictions: Many CV models are only relevant to short-term perturbations of the CV model and must be simulated with minuscule time steps. These models are primarily used to predict the CV

variables for time windows of seconds up to minutes. We are, however, interested in the long-term, steady-state perturbations and mechanisms of CV since we are predicting the first 24-48 hours post-burn. Even in the presence of long-term regulation mechanisms, a model that must be simulated with minuscule time steps to work, would impose a substantial computational burden on the model. Therefore, we eliminated the models that aimed at short-term predictions [72], [121], [122], [124], [126].

The mathematical model of renal function proposed by Uttamsingh et al. (1985) has a CV component that satisfies our criteria [127]. This model is principally developed based on Guyton's famous CO-Venous return (VR) curve and empirical equations derived from experimental data in humans from literature. Guyton's CO-VR curve, used at the heart of many CV models, has no analytical solutions, and must be solved iteratively, which is also the case for Uttamsingh's model. Additionally, the empirical equations in the model are based on old data and knowledge that have been updated since 1985 and might not work across different species in our dataset. Therefore, we set out to use the wisdom offered by Uttamsingh, Guyton, and more recent publications on relevant experimental data, to design a modified CV model that has analytical solutions, agrees with recent findings, and is tunable to different datasets.

The first variable of the model, which is directly dependent on VK, is the mean systemic pressure (MSP). MSP is defined as the pressure that exists in the venous circulatory system when there is no blood flow, and therefore is assumed to solely depend on the blood volume in the venous fraction of the circulation. Since we do not consider separate components for arterial and venous blood volumes, we, similar to

Uttamsingh, estimate MSP by the mean circulatory filling pressure (MCFP), which depends on the entire blood volume (BV). In reality, these two variables are very close to each other, except for very for very low values of CO.

Although Guyton [128] and Uttmasingh have considered a linear relationship between MSP and blood volume (BV) based on experiments conducted by Richardson et al. [129], a more recent experiment conducted by Lee et al. [130] proposes a near-exponential relationship:

$$MSP = \overline{MSP} e^{\lambda_{msp}(BV - \overline{BV})}, \tag{5.1}$$

Where $\overline{MSP}$ is the nominal MSP (Eq. (5.8)), λ_{msp} the coefficient of sensitivity, and $\overline{BV}$ is the nominal BV. BV and its nominal value are given by the VK model, which is extensively discussed in chapter 2.

Total peripheral resistance (TPR) is the primary regulator of BP in the body that is altered by the central nervous system (CNS), which senses the BP deviations directly through baroreceptors, and by the hormonal systems, particularly angiotensin II (Ang II), which is indirectly affected by BP deviations. Since the CNS-enforced variations in TPR are short-term and insignificant in the time scale of our model, we only consider the effects of Ang II in accordance with Uttamsingh. Based on the experiments in human, the relationship between TPR and the concentration of Ang II in plasma seems to be best approximated by a sigmoid function [131]:

$$TPR = \frac{(1+K_{TPR}) \times \overline{TPR}}{1+K_{TPR} \times e^{-\lambda_{TPR}([Ang\ II]-[\overline{Ang\ II}])}}, \tag{5.2}$$

Where $\overline{TPR}$ is the nominal value (described by Eq. (5.8)) , K_{TPR} and λ_{TPR} are constant coefficients, [Ang II] the concentration of Ang II in plasma, and $[\overline{Ang\ II}]$ its nominal value. The Ang II dynamics will be described in section 5.4, Eq, (5.74-77).

Guyton hypothesized and proved that the blood flow returning to the heart (VR) is proportional to the pressure drop across the systemic veins, and inversely related to the return venous resistance (RVR) [132].

$$VR = \frac{MSP - RAP}{RVR} = \frac{MSP - CVP}{RVR}, \tag{5.3}$$

RAP is the right atrial pressure, i.e., the pressure of the blood when returning to the heart and is equal to CVP. *RVR* is assumed to equal 7% of the TPR at any instant [127]. On the other hand, CO is proportional to CVP in what could be described as a series of dose-response curves whose maxima depend on cardiac effectiveness (CE):

$$CO = \frac{CO_{max}(CE)}{1 + \frac{CVP_{50}}{CVP}}, \tag{5.4}$$

Where $CO_{max}(CE)$ is the maximum CO, as a function of CE, and CVP_{50} is the CVP at which CO will reach half of its maximum values (described by Eq. (5.10)).

At steady-state, CO and VR must be equal to each other according to the Frank-Starlin law, and their true value could be found by finding the intersection point ("circulatory equilibrium") on the CO-VR curve. However, this is complicated by the effect of the CE on the CO curve, that in many cases, will require an iterative approach to finding the operating CVP point. To simplify the model and facilitate finding an analytical solution for CVP, we ignore the effect of CE on CO. This simplifying assumption is supported by Kenji [133] and Guyton et al. [134], [135] that beautifully illustrated that for a normal heart, equilibrium CO estimated by the CE-adjusted CO curve is very close to that of an unadjusted CO curve. Therefore, we can assume CO_{max} to be a constant coefficient, and find the operating CVP by equating Eq. (5.3) to (5.4):

$$RAP = \frac{1}{2}\Big[MSP - CVR.CO_{max} - CVP_{50} \pm (MSP^2 + RVR^2.CO_{max}^2 + CVP_{50}^2 -$$

$$2 \times MSP(RVR.CO_{max} - CVP_{50}) + 2RVR.CO_{max}CVP_{50})^{\frac{1}{2}}\Big], \quad (5.5)$$

This yields two solutions for CVP, among which only the larger, which is non-negative, is plausible. Having CVP, we can now proceed to calculate CO from either Eq. (5.3) or (5.4).

The pressure-flow relationship (Poiseuille's law) dictates that MAP be described as $\mathrm{CO} \times \mathrm{TPR}$. To satisfy the initial conditions and remove any bias in the definition of initial CO ($\overline{CO}$) and $\overline{TPR}$, we can write MAP as:

$$MAP = CO \times TPR - \overline{\mathrm{CO}} \times \overline{TPR} + \overline{MAP}, \quad (5.6)$$

Where $\overline{MAP}$ is MAP at baseline. After the injury, a surge of inflammatory responses could cause vasoconstriction and vasodilation to exist simultaneously [136], [137]. We have already discussed and implemented the effect of inflammatory-induced vasodilation on small vessels in the vascular capillary hydrostatic pressure in chapter 2 (Eq. (2.38)), which acts by increasing the number of perfused vessels. Vasoconstriction, which happens in large vessels, could cause a transient increase in MAP despite the lowered BV and CO [138]. We systematically see this transiently increased MAP in our sheep subjects, and to a lesser extent in pigs. To be able to capture this behavior, we have added a transient term per our global perturbation equation (Eq. (2.28)) and updated Eq. (5.6):

$$MAP = CO \times TPR - \overline{CO} \times \overline{TPR} + \overline{MAP} + M_{MAP}\left(e^{-\lambda_{1,MAP,t}} - e^{-\lambda_{2,MAP}t}\right), \quad (5.7)$$

where M_{MAP} is the maximum perturbation, and $\lambda_{1,MAP}$ and $\lambda_{2,MAP}$ are the slow and fast time constants associated with the decay of the perturbation in MAP.

There are several constraints that we need to consider in order to satisfy the initial conditions for CO and CVP:

$$\overline{TPR} = \frac{\overline{MSP} - \overline{CVP}}{0.07CO}, \tag{5.8}$$

Uttamsingh assumes $\overline{MSP}$ to equal 7 mmHg; however, our pig and sheep subjects have different $\overline{CVP}$ values, and the assumption of 7 mmHg, could result in negative TPR values when BV dropped after the injury. To allow a safety zone of at least 5 mmHg for MSP to drop without resulting in negative TPR values, we defined MSP_0 as:

$$\overline{MSP} = \overline{CVP} + 5, \tag{5.9}$$

Which yields realistic values for MSP across different species.

Finally, to satisfy the initial condition for CO in Eq. (5.4) we can calculate CVP_{50} as follows:

$$CVP_{50} = \overline{CVP}\left(\frac{CO_{max}}{\overline{CO}} - 1\right), \tag{5.10}$$

The CV model has a total of 10 unknown parameters. For sheep subjects, we use the initial CO and MAP variable from the experimental data and estimate the initial CVP, leaving eight unknown parameters to be found via optimization.

5.3 A Modified Renal Function Model: Considerations and Formulation

In this section, we review a more detailed and accurate description of the kidney regulatory mechanisms, followed by how we formulated these mechanisms and resolved the limitations of the previous model.

5.3.1 Glomerular Filtration Rate and Renal Plasma Flow Regulation

Fig. 5.1. shows a simple schematic of the renal function pertaining to the glomerular filtration rate (GFR) and renal plasma flow (RPF) regulation. As discussed in chapter 2, plasma flows into the kidney through the renal arteries, which branch into millions of parallel nephrons. In every nephron, the flow passes through the afferent arterioles into the glomerular space, where about 20% of it is usually filtered into the bowman's capsule (called the filtrate). The remaining 80% of fluid then flows along the efferent arterioles, peritubular capillaries, and eventually the renal venules. Along this path, the majority of the filtered fluid is reabsorbed back into the circulation, so typically only about 1% of the RPF is excreted as urine. To simplify the model, we have assumed that all nephrons have similar characteristics and resistances and calculated the collective flows to represent the dynamics of the entire kidney.

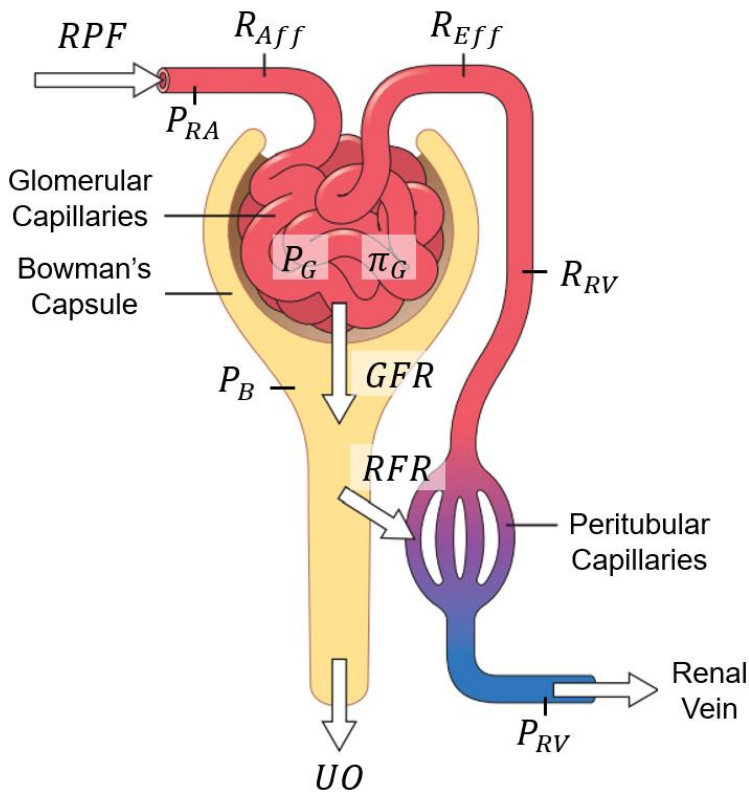

Fig. 5.1: A schematic of RPF and GFR determining mechanisms. RPF: renal plasma flow, GFR: glomerular filtration rate, RFR: reabsorption flow rate, UO: urinary output; R_{Aff}: afferent resistance, R_{Eff}: efferent resistance, R_{RV}: renal vein resistance; P_{RA}: renal arterial pressure, P_{RV} renal vein pressure, P_G: glomerular hydrostatic pressure, π_G: glomerular colloid oncotic pressure, P_B: Bowman's capsule hydrostatic pressure. Figure taken from Guyton and Hall.

Following Poiseuille's Law, the rate at which plasma flows into the kidney depends on the pressure drop across the kidney as well as total renal resistance:

$$J_{RPF} = \frac{P_{RA} - P_{RV}}{R_{Kidney}}, \tag{5.11}$$

$$R_{Kidney} = R_{Aff} + R_{Eff} + R_{RV}, \tag{5.12}$$

Where P_{RA} is the renal arterial pressure, P_{RV} the renal vein pressure, and R_{Kidney} is the total renal resistance, which consists of the renal afferent resistance (R_{Aff}), the renal efferent resistance (R_{Eff}), and the renal vein resistance (R_{RV}).

P_{RA} and P_{RV} are linear functions of MAP and CVP, respectively, with plausible initial values [127], [139]:

$$P_{RA} = 85 + K_{RA}(MAP - \overline{MAP}), \tag{5.13}$$

$$P_{RV} = 3 + K_{RV}(CVP - \overline{CVP}), \tag{5.14}$$

Where K_{RA} and K_{RV} are constant. Since disruptions in RPF and GFR negatively affect renal perfusion and function and could lead to renal failure in extreme cases, the kidneys have intrinsic regulatory mechanisms to keep GFR and RPF around nominal values. The myogenic mechanism (MM) and the Tubuglomerular feedback mechanism (TGF) are the two most important regulatory mechanisms in the kidneys, whose standard actuator is the afferent resistance. Therefore, the afferent resistance is assumed to be comprised of three parts:

$$R_{Aff} = R_{TGF} + R_{MM} + R_{A,0}, \tag{5.15}$$

Where R_{TGF} is the part of the afferent resistance that regulated by the TGF, R_{MM} the part regulated by the MM, and $R_{A,0}$ is a constant, baseline resistance.

Although MM and TGF have the same actuator, they have different inputs. The MM senses the changes in the renal arterial pressure and alters the afferent resistance to maintain the RPF and GFR. For instance, in response to an increase in renal arterial pressure, the MM increases the R_{MM} and limits the plasma flow into the kidneys (Eq. (5.11) and (5.12)). R_{MM} could be calculated by first, assuming that the increase in the afferent pressure is going to completely counteract the effect of increased renal arterial pressure so that the RPF stays the same, and then multiplying the resulting equation to a scaling coefficient which determines the power that MM has to compensate for the

change in the renal arterial pressure. We have used a scaled version of this equation derived by Moore et al. [140], and used by Moss et al. [141], and Czerwin et al. [139]:

$$R_{MM} = G_{MM}\left(R_{TGF} + R_{A,0} + R_{Eff}\right)H\left(\frac{P_{RA}}{P_{ref}} - 1\right), \tag{5.16}$$

Where P_{ref} is the reference pressure below which the R_{MM} equals zero, and G_{MM}, which is the MM scaling coefficient, is chosen to yield plausible initial values for R_{MM} (Table 5.x) [139]. We should note that this term is in reality called the descending myogenic mechanism, and there is also an ascending myogenic mechanism term which we did not considered due to its insignificance compared to the descending mechanism and TGF [140], [141].

The TGF, however, senses the sodium concentration at a specific part of the nephrons called the Macula Densa (MD). The MD is a group of specialized cells in close contact with the afferent arterioles. The sodium concentration at the MD ($[Na^+]_{MD}$), has a direct relationship with GFR, shaped by mechanisms that we will fully explain in section 5.3.2. Simply put, a faster GFR means a quicker flow rate across the nephron tubules and less time for the passive mechanisms to reabsorb the sodium. The MD cells will sense the higher $[Na^+]_{MD}$, and immediately send commands to restrict the afferent arterioles, increasing R_{TGF} and decreasing the GFR and $[Na^+]_{MD}$. This regulation can be described by a sigmoid function [139]:

$$R_{TGF} = \frac{(1+K_{TGF})\times\overline{R_{TGF}}}{1+K_{TGF}\times e^{-\lambda_{TGF}\left([Na^+]_{MD} - \left[\overline{Na^+}\right]_{MD}\right)}}, \tag{5.17}$$

Where K_{TGF} and λ_{TGF} are constant coefficients representing the maximum and steepness of the sigmoid function, and the bar superscript indicates the nominal value for the variables. $[Na]_{MD}$ and its nominal value are later calculated (Eq. 5.55 and

section 5.3.2). The TGF has a second functionality that regulates the MAP and GFR in a more long-term fashion. The MD cells promote the release of renin, the first element of the RAAS, in response to reduced $[Na^+]_{MD}$. Through a mechanism that will be explained in section 5.5, Ang II is released which will restrict the efferent arterioles:

$$R_{Eff} = \frac{K_{Eff}\overline{R_{Eff}}}{1+\frac{[Ang\ II]_{E,50}}{[Ang\ II]}}, \tag{5.18}$$

$$[Ang\ II]_{E,50} = \overline{[Ang\ II]}(K_{Eff} - 1), \tag{5.19}$$

Where K_{Eff} is a constant coefficient, and $[Ang\ II]_{E,50}$ is the concentration at which R_{Eff} reaches half of its maximum value, which is defined by Eq. (5.19) to satisfy the initial conditions.

In the previous version of the model (Chapter 2, Eq. (2.14)), we assumed that the RPF is a linear function of PV. This assumption could be questioned from two aspects: 1) RPF must depend on renal resistance according to the pressure-flow relationship and be closely regulated, and 2) it should be a function of MAP as opposed to PV. In the updated model, we resolved both of these limitations. Also, in the previous version, the renal resistance was represented by a single variable that sensed the variations of GFR (Eq. (2.15)), but here, we have provided a more accurate description of the renal resistance regulation.

The GFR still follows the Starling equation as explained in chapter 2:

$$J_{GFR} = K_G[P_G - P_B - \pi_G], \tag{5.20}$$

As a review, K_G is the glomerular filtration coefficient, π_G the glomerular colloid oncotic pressure, P_B the hydrostatic pressure of Bowman's capsule, and P_G the glomerular hydrostatic pressure. Another violation of Poiseuille's law happened in the

formulation of P_G, which had an inverse relationship with renal resistance (Eq. (2.16)) in the original model. To design the new formulation, we first assumed that despite the fluid being filtered across the glomerular capillaries, P_G does not change from the beginning to the end of the capillaries since arteries pressurize them from both sides [142]. Then, according to Poiseuille's law, the pressure drop from the efferent arterioles to the renal vein is proportional to the flow rate along this path and inversely related to its resistance:

$$P_G - P_{RV} = (R_{Eff} + R_{RV})(J_{RPF} - J_{GFR} + J_{RFR}) = (R_{Eff} + R_{RV})(J_{RPF} - UO), \quad (5.21)$$

Where J_{RFR} is the reabsorption flow rate (RFR). Since UO is very small compared to J_{RPF} in all conditions, we can simplify the Eq. (5.21) and rearrange to get P_G:

$$P_G = P_{RV} + (R_{Eff} + R_{RV})(J_{RPF} - UO) \sim P_{RV} + (R_{Eff} + R_{RV})(J_{RPF}), \quad (5.22)$$

Finally, π_G in the original model only estimated the value at the end of the glomerular capillaries, where all the filtrate was removed (Eq. (2.18)). In reality, there is a steep gradient in π_G along the glomerular capillaries, since the albumin stays within the glomerular space while the fluid keeps getting filtered, raising the colloid oncotic pressure. The higher the GFR, the steeper the π_G gradient. Since the GFR itself is a function of π_G, this can cause a chicken and egg problem, calling for a numerical computation method, or complex finite element methods to predict how π_G varies along the tubules [141]. But there is one other way we can look at this problem. It has been hypothesized and experimentally shown that almost always, the GFR keeps flowing into the Bowman's capsule until the Starling forces equal to zero, called the equilibrium point [143], [144]. Following Eq. (5.20) and considering the fact that both P_G and P_B are constant along the nephron tubules, we can write:

$$\pi_{G,f} = P_G - P_B, \tag{5.23}$$

Where $\pi_{G,f}$ is the value of π_G at equilibrium point, where the glomerular filtration stops. We also know that since the blood flows freely up to the beginning of the glomerular arterioles, carrying its proteins with it, the colloid oncotic pressure at the beginning of the glomerular space equals that of plasma. For simplicity, we assume that π_G could be estimated as the average of the two values:

$$\pi_G = \frac{\pi_{G,f}+\pi_C}{2} = \frac{P_G - P_B + \pi_C}{2}, \tag{5.24}$$

Where π_C is the plasma colloid oncotic pressure.

The new GFR formulation adds two tunable parameters (K_{TGF} and λ_{TGF}) to the original model. The initial value of total renal resistance is chosen such that a 70 kg person would have a normal 625 ml/min renal plasma flow [83], and distribution of resistance is designed to yield plausible initial values for different components of the renal resistance (Table 5.4-5.6).

5.3.2 The Reabsorption of Water and Sodium

Fig. 5.2 illustrates the convoluted structure of a nephron and its segments. Water and sodium are filtered from the glomerular capillaries into the Bowman's capsule. Then the filtrate flows into the proximal tubules, the Loop of Henle, and the distal and collecting tubules, getting reabsorbed back into the circulation along the way. The remaining fluid empties through the collecting ducts into the ureter and the bladder, where it is excreted as UO. The MD is located close to the afferent arterioles to enable the activation of TGF. The characteristics of sodium and water reabsorption are entirely

different from one another and from segment to segment and capturing this difference is key to TGF and RAAS functions.

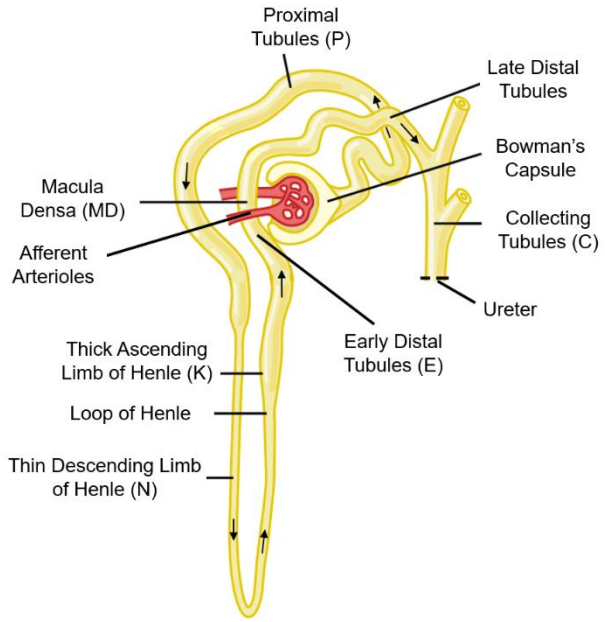

Fig. 5.2: A schematic the sections of a nephron that are functionally different (from Guyton and Hall medical textbook).

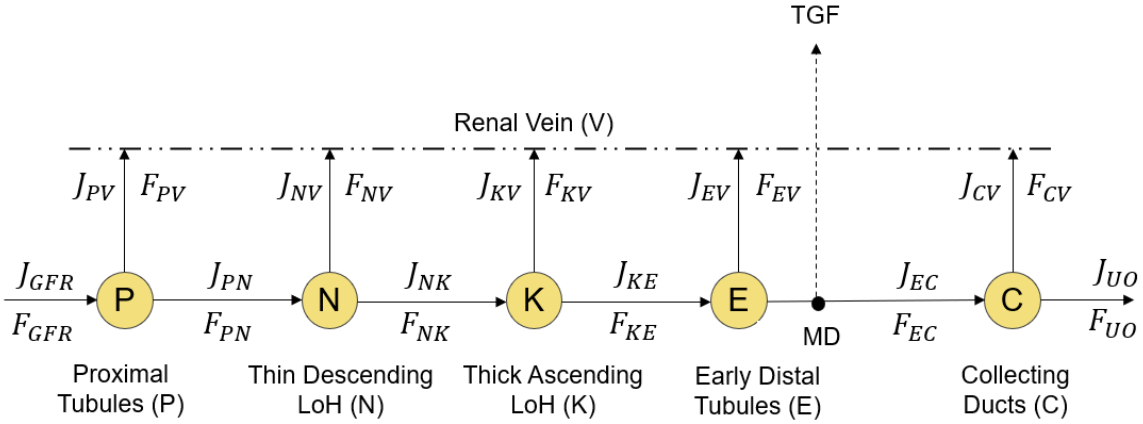

Fig. 5.3: A node schematic of the renal reabsorption model. Abbreviations and concepts are explained below.

Fig. 5.3 is a node schematic of the renal reabsorption model, similar to Czerwin et al. [139], where every node is a segment of the nephron that contributes to the reabsorption of either or both water and sodium. Node P stands for proximal tubules, N for the thin descending limb of Henle (LoH), E for the early distal tubule, and C represents the reabsorption in both late distal tubules and the collecting ducts. MD is the Macula Densa, not a node, but a sensor that sends signals to the TGF as mentioned before. In this schematic, J_{XY} represents the water flow, and F_{XY} the sodium flow, from node X to Y. V stands for renal vein, and every flow leading to that represents reabsorption back into the circulation. J_{GFR} is the glomerular filtration rate of water, F_{GFR} the glomerular filtration rate of sodium, and J_{UO} and F_{UO} represent the excretion rate of water and sodium, which collectively is excreted as UO.

At the proximal tubules, normally 65-75% of the filtered water and sodium are actively reabsorbed together, which is conserved by the glomerulotubular balance [127], [139], [141]. A second factor that has been shown to affect the proximal tubule reabsorption of sodium (and consequently water due to osmosis) in the proximal tubules, is the activation of angiotensin and aldosterone [145]–[147]. We have modeled this phenomenon as a dose-response curve which is bounded from both sides to feasible values, since the proximal tubule reabsorption fraction is mediated by the glomerulotubular balance:

$$r_P = 0.5 + \frac{0.3}{1+\frac{[ALD]_{50,P}}{[ALD]}}, \tag{5.25}$$

$$[ALD]_{50,P} = \overline{[ALD]}\left(\frac{0.3}{r_{P_0}-0.5} - 1\right), \tag{5.26}$$

Where r_P is the reabsorption fraction at the proximal tubules, $[ALD]$ the plasma aldosterone concentration, $\overline{[ALD]}$ its nominal value, and $[ALD]_{50,P}$ the concentration at which the response reaches half of its maximum value, which defined in a way that satisfies the initial condition for r_P (r_{P_0}). Having the reansorption fraction we can write:

$$J_{PV} = r_P J_{GFR}, \tag{5.27}$$

$$F_{PV} = r_P F_{GFR} = r_P J_{GFR}[Na^+], \tag{5.28}$$

$$[Na^+]_P = [Na^+], \tag{5.29}$$

$$J_{PN} = J_{GFR} - r_P J_{GFR} = J_{GFR}(1 - r_P), \tag{5.30}$$

$$F_{PN} = F_{GFR} - r_P F_{GFR} = F_{GFR}(1 - r_P), \tag{5.31}$$

Where $[Na^+]_P$ is the sodium concentration of the filtrate at the end of this node, which is similar to plasma sodium concentration since the reabsorption fraction is the same for water and sodium.

The thin descending LoH is impermeable to sodium and only water is reabsorbed passively through osmosis, meaning that the longer the fluid is in contact with the surface of nephrons before passing, the higher the reabsorption fraction in this section. This creates an inverse relationship with flow rate, which is one of the major players in the phenomenon of pressure diuresis, i.e., when GFR increases, the water passes the nephrons quicker and is reabsorbed less than usual, leading to a disproportionate increase in the UO. Assuming that the cross-sectional area of the LoH (A_N) and its length (Δx_N) are constant, we can write:

$$\Delta t_{pass} = \frac{\Delta x_N\ [dm]}{V_N\ [\frac{dm}{min}]} = \frac{\Delta x_N\ [dm]}{\frac{J_{PN}\left[\frac{ml}{min}\right]}{A_N\ [dm^2]}}, \tag{5.31}$$

Where Δt_{pass} is the time it takes for the filtrate to pass the descending LoH. Now if we assume that the reabsorption rate is a linear function of this time, we will have:

$$J_{NV} \propto C_{NV}\Delta t_{pass} = \frac{C_{NV}\Delta x_N\, A_N}{J_{PN}}, \tag{5.32}$$

$$r_N = \frac{J_{NV}}{J_{PN}} \propto \frac{C_{NV}\Delta x_N\, A_N}{J_{PN}^2}, \tag{5.33}$$

Where r_N is the water reabsorption fraction at node N. This is an indication of the nonlinearity of the relationship between r_N and the flow rate. To simplify, we can describe r_N as an inverse-sigmoidal function of the flow:

$$r_N = \frac{2\times r_{N,0}}{1+e^{\lambda_N(\frac{J_{PN}}{J_{PN,0}}-1)}}, \tag{5.34}$$

$$J_{PN,0} = \bar{J}_{GFR}(1 - r_{P_0}), \tag{5.35}$$

Where λ_N is a positive, constant coefficient.

$$J_{NV} = J_{PN} r_N, \tag{5.36}$$

$$F_{NV} = 0, \tag{5.37}$$

$$J_{NK} = J_{PN}(1 - r_N), \tag{5.38}$$

$$F_{NK} = F_{PN}, \tag{5.39}$$

$$[Na^+]_N = \frac{F_{NK}}{J_{NK}}, \tag{5.40}$$

Since only water is reabsorbed, the sodium concentration at node N ($[Na^+]_N$) increases. We used this property to determine an appropriate initial value for r_N ($r_{N,0}$) and reasonable range for λ_N, using the experimental data from Layton and Layton [148] that suggested $[Na^+]_N$ is normally about 1.8 times that of the proximal tubules at this node:

$$[Na^+]_{N,0} = \frac{F_{PK,0}}{J_{NK,0}} = \frac{[Na^+]_P}{1-r_{N,0}} = 1.8[Na^+]_P, \tag{5.41}$$

This means $r_{N,0}$ is normally about 0.44, that brings the total reabsorption fraction of water before reaching the collecting duct to about 80% which agrees with Guyton's findings [50]. We can re-write Eq. (5.34) as:

$$r_N = \frac{0.88}{1+e^{\lambda_N \frac{J_{PN}}{J_{PN,0}}-1}}, \tag{5.42}$$

The thick ascending LoH, on the contrary, is impermeable to water and actively reabsorbs about 60% of the remaining sodium flow. Since our proximal reabsorption fraction is tunable and can take any value between 0.65-0.75, we designed the reabsorption fraction at this node such that at the end of it, collectively 90% of the sodium would be reabsorbed:

$$r_K = \frac{0.9-r_P}{1-r_P}, \tag{5.43}$$

Where r_K is the sodium reabsorption fraction at node K. Therefore:

$$J_{KV} = 0, \tag{5.44}$$

$$F_{KV} = F_{PK} r_K, \tag{5.45}$$

$$J_{KE} = J_{NK}, \tag{5.46}$$

$$F_{KE} = F_{PK}(1 - r_K), \tag{5.47}$$

$$[Na^+]_K = \frac{F_{KE}}{J_{KE}}, \tag{5.48}$$

Since there is only sodium reabsorption at node K, the sodium concentration drastically decreases.

Before reaching the MD, we pass through the end of the LoH and into the early distal tubules (E). Here we still have water impermeability, but the sodium reabsorption is passive and has an inverse relationship with its flow rate. We have used an inverse-sigmoidal function of the flow similar to the passive reabsorption at node N [139]:

$$r_E = \frac{1}{1+e^{\lambda_E\left(\frac{F_{KE}}{F_{KE,0}}-1\right)}}, \tag{5.49}$$

Where r_E is the sodium reabsorption fraction, λ_E a constant coefficient, and $F_{KE,0}$ the nominal F_{KE} value which is calculated by inserting the nominal reabsorption fractions. The normal reabsorption fraction at node E is considered to be 0.5, which collectively makes the sodium reabsorption up to the collecting duct equal to 95% of the glomerular flow.

$$J_{EV} = 0, \tag{5.50}$$

$$F_{EV} = F_{KE} r_E, \tag{5.51}$$

$$J_{EC} = J_{NK}, \tag{5.52}$$

$$F_{EC} = F_{KE}(1 - r_E), \tag{5.53}$$

$$[Na^+]_E = \frac{F_{EC}}{J_{EC}} = [Na^+]_{MD}, \tag{5.54}$$

The sodium concentration at the Macula Densa is thus determined and has an inverse relationship with the GFR, which lays the foundation for the TGF. Since we have assumed that the normal sodium reabsorption fraction when we reach the MD is 0.95, the initial value of $[Na^+]_{MD}$ that is an important factor in the TGF formulation (Eq. (5.17)). will be determined by the total water reabsorption fraction when we arrive at MD:

$$\left[\overline{Na^+}\right]_{MD} = \frac{F_{EC,0}}{J_{EC,0}} = \frac{(1-0.95)J_{GFR,0}\overline{[Na^+]}}{(1-r_P)(1-0.44)\bar{J}_{GFR}} = \frac{0.089\overline{[Na^+]}}{\left(1-r_{P_0}\right)}, \tag{5.55}$$

Where $\overline{[Na^+]}$ is the nominal plasma sodium concentration. The late distal and collecting ducts are the realm of hormones, i.e., the reabsorption of the remaining water is regulated by the ADH, and sodium by the aldosterone. The ADH dynamics is similar

to what was described in chapter 2, and the only change is replacing the V_P with CO to estimate the rate by which ADH flows into the liver to be metabolized:

$$\frac{d(ADH)}{dt} = K_{ADH} e^{\left(-\lambda_{V_P} \Delta V_P + \lambda_{[Na^+]} \Delta [Na^+]\right)} - 0.27 K_{ADH} [ADH] \frac{J_{GFR}}{\bar{J}_{GFR}} - 0.73 K_{ADH} [ADH] \frac{CO}{\overline{CO}}, \quad (5.56)$$

Where $\overline{CO}$ is the initial CO value. The reabsorption rate of water and sodium are described by dose-response curves of the ADH concentration in plasma ($[ADH]$) and aldosterone concentration in plasma ($[ALD]$), respectively:

$$r_{CW} = \frac{r_{CW,max} - r_{CW,min}}{1 + \frac{[ADH]_{50}}{[ADH]}} + r_{CW,min}, \quad (5.57)$$

$$[ADH]_{50} = [ADH]_0 \left(\frac{r_{CW,max} - r_{CW,min}}{\overline{r_{CW}} - r_{CW,min}} - 1 \right), \quad (5.58)$$

$$r_{CNa} = \frac{r_{CNa,max} - r_{CNa,min}}{1 + \left(\frac{[ALD]_{50}}{[ALD]}\right)^{n_{ALD}}} + r_{CNa,min}, \quad (5.59)$$

$$[ALD]_{50} = [ALD]_0 \sqrt[n_{ALD}]{\frac{r_{CNa,max} - r_{CNa,min}}{\overline{r_{CNa}} - r_{CNa,min}} - 1}, \quad (5.60)$$

$$J_{CV} = J_{EC} r_{CW}, \quad (5.61)$$

$$F_{CV} = F_{EC} r_{CNa}, \quad (5.61)$$

$$J_{UO} = J_{EC}(1 - r_{CW}), \quad (5.63)$$

$$F_{UO} = F_{EC}(1 - r_{CNa}), \quad (5.64)$$

$$[Na^+]_{UO} = \frac{F_{UO}}{J_{UO}}, \quad (5.65)$$

Where r_{CW} is the water reabsorption fraction in the collecting ducts mediated by the ADH, r_{CNa} is the sodium reabsorption fraction at this node mediated by aldosterone, and n_{ALD} is the order of the aldosterone dose-response curve. The min and max subscripts represent the possible minimum and maximum values for the reabsorption

fractions, which are imbedded into the dose-response curve to ensure the reabsorption fraction functions have reasonable upper and lower bounds. $[ADH]_{50}$ and $[ALD]_{50}$ are plasma ADH and aldosterone concentrations at which their mediated reabsorption fraction reaches half of its maximum value. They are determined such that the initial condition values for the reabsorption fractions ($r_{CW,0}$ and $r_{CNa,0}$) are satisfied.

While $r_{CW,0}$ us optimized and can take any value between 0.92 to 0.97, in defining the $\mathrm{r}_{\mathrm{CNa,0}}$ we have to consider that the baseline urine sodium concentration ($[Na^+]_{UO}$) can take vastly different values during the day, and more importantly, across different species. Therefore, we optimize the ratio of normal urine sodium concentration to normal PV sodium concentration ($\alpha_{UO,Na}$). Since we have designed the reabsorption model such that normally 95% of the sodium flow is reabsorbed before reaching the collecting ducts, we can write:

$$\alpha_{UO,Na} = \frac{[Na^+]_{UO,0}}{\overline{[Na^+]}} = \frac{F_{UO,0}}{\overline{[Na^+]}J_{UO,0}} = \frac{J_{GFR}(1-0.95)(1-\overline{r_{CNa}})\overline{[Na^+]}}{\overline{[Na^+]}J_{GFR}(1-r_P)(1-0.44)(1-\overline{r_{CNa}})}, \tag{5.66}$$

Therefore, we can find $r_{CNa,0}$ as a function of $\alpha_{UO,Na}$, r_P and $r_{CW,0}$ using the constraint above:

$$\overline{r_{CNa}} = 1 - 11.2 \times \alpha_{UO,Na}(1 - r_P)(1 - \overline{r_{CW}}), \tag{5.67}$$

5.4 Renin-Angiotensin-Aldosterone System

The RAAS is a mechanism for long-term regulation of blood pressure, blood volume, and electrolytes. The first element of the system, renin, is an enzyme, and part of the TGF. When the MD cells sense the variation in the MD sodium concentration and send commands to change the afferent resistance, they also send commands to change the renin release rate.

Suppose that there is a decrease in BV, and MAP drops. This will reduce the RPF, GFR, and subsequently, $[Na^+]_{MD}$. There is an inverse relationship between the renin release rate and $[Na^+]_{MD}$ [149]. Therefore, a drop in GFR eventually increases the renin release rate. Renin converts angiotensinogen to angiotensin I, which is converted to the vasoconstrictor hormone angiotensin II [147]. Ang II will constrict the vessels and increase the TPR, increasing the blood pressure and the GFR. Because it has a more pronounced effect on the efferent arterioles than afferent arterioles [150], it can increase the GFR at the risk of reducing the RPF (see Eq. (5.11) and (5.22)). Finally, Ang II increases the release rate of ALD which leads to the retention of sodium and, eventually, water [147]. Therefore, the RAAS significantly contributes to the long-term regulation of blood pressure, blood volume, and electrolytes.

The renin release is assumed to be a linear function of the fractional change in $[\mathrm{Na}^+]_{\mathrm{MD}}$:

$$\frac{d(Re)^+}{dt} = Re_0^+\left(1 - \frac{[Na^+]_{MD} - \overline{[Na^+]}_{MD}}{\overline{[Na^+]}_{MD}}\right), \tag{5.68}$$

Where Re_0^+ is the release rate at baseline. Normally about 60% of renin is metabolized in the liver, 20% cleared by the kidneys, and 20% by other tissues, which we have assumed to have a constant clearance rate [151]. Considering that initially the excretion rate must equal the release rate, we can write:

$$\frac{d(Re)^-}{dt} = \frac{0.6Re_0^+}{[Re]_0}[Re]\left(1 + \frac{CO - \overline{CO}}{\overline{CO}}\right) + \frac{0.2Re_0^+}{[Re]_0}[Re]\left(1 + \frac{J_{GFR} - J_{GFR_0}}{J_{GFR_0}}\right) + 0.2Re_0^+, \tag{5.69}$$

$$\frac{d(Re)}{dt} = \frac{d(Re)^+}{dt} - \frac{d(Re)^-}{dt}, \tag{5.70}$$

$$[Re] = \frac{Re}{V_{PL}}, \tag{5.71}$$

Where Re is the total renin circulating in the blood, [Re] is its plasma concentration, and $[\mathrm{Re}]_0$ the initial plasma concentration of renin. The dependency of the first term on CO originates from the fact that the liver blood flow is determined by CO.

Studies have shown that there is a 20–90-minute latency period before Ang II and aldosterone get activated [50], [147]. To simplify the model, we have incorporated the delay into the renin dynamics, which is the precursor to both Ang II and aldosterone:

$$\Delta[Re] = \frac{[Re]-[Re]_0}{[Re]_0}, \tag{5.72}$$

$$\frac{d(\Delta[Re]_{del})}{dt} = \frac{\Delta[Re]-\Delta[Re]_{del}}{\tau_{ren}}, \tag{5.73}$$

Where $\Delta[Re]$ is the fractional deviation of plasma renin concentration from baseline, $\Delta[\mathrm{Re}]_{\mathrm{del}}$ its delayed effect, and τ_{ren} the time constant.

The relationship between Ang II release rate and the delayed renin variation is also linear [127], [152]:

$$\frac{d(Ang\ II)^+}{dt} = Ang\ II_0^+(1 + C_{Ang}\Delta[Re]_{del}), \tag{5.74}$$

Where $Ang\ II_0^+$ is the Ang II nominal release rate, and C_{Ang} a constant coefficient reflecting the sensitivity of Ang II release rate to renin.

Almost all of the Ang II is deactivated by its passage through the liver. Assuming steady-state conditions at baseline:

$$\frac{d(Ang\ II)^-}{dt} = \frac{Ang\ II_0^+}{[Ang\ II]}[Ang\ II]\left(1 + \frac{CO-\overline{CO}}{\overline{CO}}\right), \tag{5.75}$$

$$\frac{d(Ang\ II)}{dt} = \frac{d(Ang\ II)^+}{dt} - \frac{d(Ang\ II)^-}{dt}, \tag{5.76}$$

$$[Ang\ II] = \frac{Ang\ II}{V_{PL}}, \tag{5.77}$$

The final component of the RAAS, aldosterone, is primarily secreted in response to increased $[Ang\ II]$, plasma potassium concentration, and decreased plasma sodium concentration [127], [147]. In this model, we have assumed that the potassium concentration is constant, and the aldosterone secretion rate is an exponential function of the weighted sum of the effects of Ang II and plasma sodium concentrations:

$$\frac{d(ALD)^+}{dt} = ALD_0^+ e^{(w_{ALD}\Delta ALD_{Na}^+ + (1-w_{ALD})\Delta ALD_{Ang}^+)}, \tag{5.78}$$

Where ALD_0^+ is the nominal aldosterone secretion rate, w_{ALD} the weight of the effect of $[\mathrm{Na}^+]$, which can take any value between 0 and 1, ΔALD_{Na}^+ is the fractional effect of $[Na^+]$ on aldosterone release rate, and ΔALD_{Ang}^+ is the fractional effect of $[Ang\ II]$. The relationship between the aldosterone secretion and plasma sodium concentration is assumed to be linear:

$$\Delta ALD_{Na}^+ = -C_{ALD,Na}\left(1 - \frac{[Na^+]-\overline{[Na^+]}}{\overline{[Na^+]}}\right), \tag{5.79}$$

Where $C_{ALD,Na}$ a constant coefficient. Therefore when $[Na^+]$ decreases, the aldosterone concentration is increased and reabsorbs more sodium in the collecting ducts to recover the normal $[Na^+]$ levels (Eq.(5.59))

The following dose-response curve can capture the relationship between the aldosterone release rate and [Ang II] based on experiments conducted by Blair et al. [153]:

$$\Delta ALD_{Ang}^+ = \frac{K_{ALD}}{1+\left(\frac{[Ang\ II]_{50}}{[Ang\ II]}\right)^3} - 1, \tag{5.80}$$

Where, K_{ALD} is the maximum fractional increase in ΔALD_{Ang}^+, and $[Ang\ II]_{50}$ is the concentration at which ΔALD_{Ang}^+ is half of its maximum possible value. To conserve the steady-state at baseline, we can define $[Ang\ II]_{50}$ as:

$$[Ang\ II]_{50} = [Ang\ II]\sqrt[3]{K_{ALD} - 1}, \tag{5.81}$$

Given that normally about 90% of aldosterone is metabolized by the liver and 10% excreted by the kidneys, the aldosterone excretion could be estimated by:

$$\frac{d(ALD)^-}{dt} = \frac{0.9ALD_0^+}{\overline{[ALD]}}[ALD]\left(1 + \frac{CO - CO_0}{CO_0}\right) + \frac{0.1ALD_0^+}{\overline{[ALD]}}[ALD]\left(1 + \frac{J_{GFR} - \bar{J}_{GFR}}{\bar{J}_{GFR}}\right), \tag{5.82}$$

$$\frac{d(ALD)}{dt} = \frac{d(ALD)^+}{dt} - \frac{d(ALD)^-}{dt}, \tag{5.83}$$

$$[ALD] = \frac{ALD}{V_{PL}}, \tag{5.84}$$

Where ALD_0^+ is the aldosterone baseline reabsorption rate, and $\overline{[ALD]}$ its baseline concentration in plasma.

The RAAS model adds four states and six tunable parameters to the model.

5.5 Verification of the Renal Model and RAAS

Before moving on to optimization and validation of the model, we simulated the renal function and RAAS model with plausible parameter values for a range of renal arterial pressures to make sure the different components were working correctly. One motivation behind this preliminary analysis was that we have several new phenomenological elements in the model, such as the dose-response curves that describe the reabsorption fractions' relationship with ALD and ADH or the passive reabsorption fraction relationships, to name a few. These phenomenological models are integrated into mechanistic models, and we have to ensure that they predict physiologically feasible values for subjects with different characteristics under different conditions for three different species. To do this, while we have relied on

literature to assume the “form” of these phenomenological relationships, we were meticulous in defining the parameter bounds and baseline values in a way that can accommodate the inter-subject and inter-species variabilities.

Fig. 5.4 (a) shows how the sodium concentration at different nodes of the nephrons will vary by changing the renal arterial pressure from the baseline value of 85 mmHg. As expected, the sodium concentration at node P will remain the same as the plasma sodium concentration (B stands for Bowman’s capsule) for all of the pressures, since sodium and water will be reabsorbed together. At node N, where only water is reabsorbed, the reabsorption rate has an inverse relationship with the flow rate. Therefore, the higher the pressure and GFR, the less water reabsorbed, and the higher the sodium concentration would be, which is captured by the model. At node K, we will have the same reabsorption rate of sodium for all the nodes, and no water reabsorption. Thus, the sodium concentration decreases for all the pressures, and the order is preserved. At node E. however, where the MD is located, the sodium reabsorption has an inverse relationship with the flow rate. Therefore, the fastest flow undergoes the least reabsorption, and therefore we will have the highest sodium concentration, as evident from the plot.

Fig 5.4. (b) compares the predicted nominal (i.e., $P_{RA} = 85$ mmHg) sodium concentration at different nodes, against the data provided by Layton and Layton [139], [148].

Fig 5.4. (c) shows how the UO drastically changes in response to renal arterial pressure variation, while the GFR is regulated by the TGF and MM mechanisms. This simulation does not consider the regulatory effect of efferent resistance, which when

present, regulates GFR more strictly. This plot is also an illustration of the phenomenon of diuresis, since we can see that for a 50% increase in the GFR, UO has increased by about 250%.

Fig 5.4. (d) shows how renin release rate changes in response to renal arterial pressure variation. This nonlinear, inverse relationship is very similar to the behavior described by Kurtz [149], and shows that renin secretion is inhibited in response to renal arterial pressure increase, to lower the angiotensin concentration, and consequently renal arterial pressure and GFR.

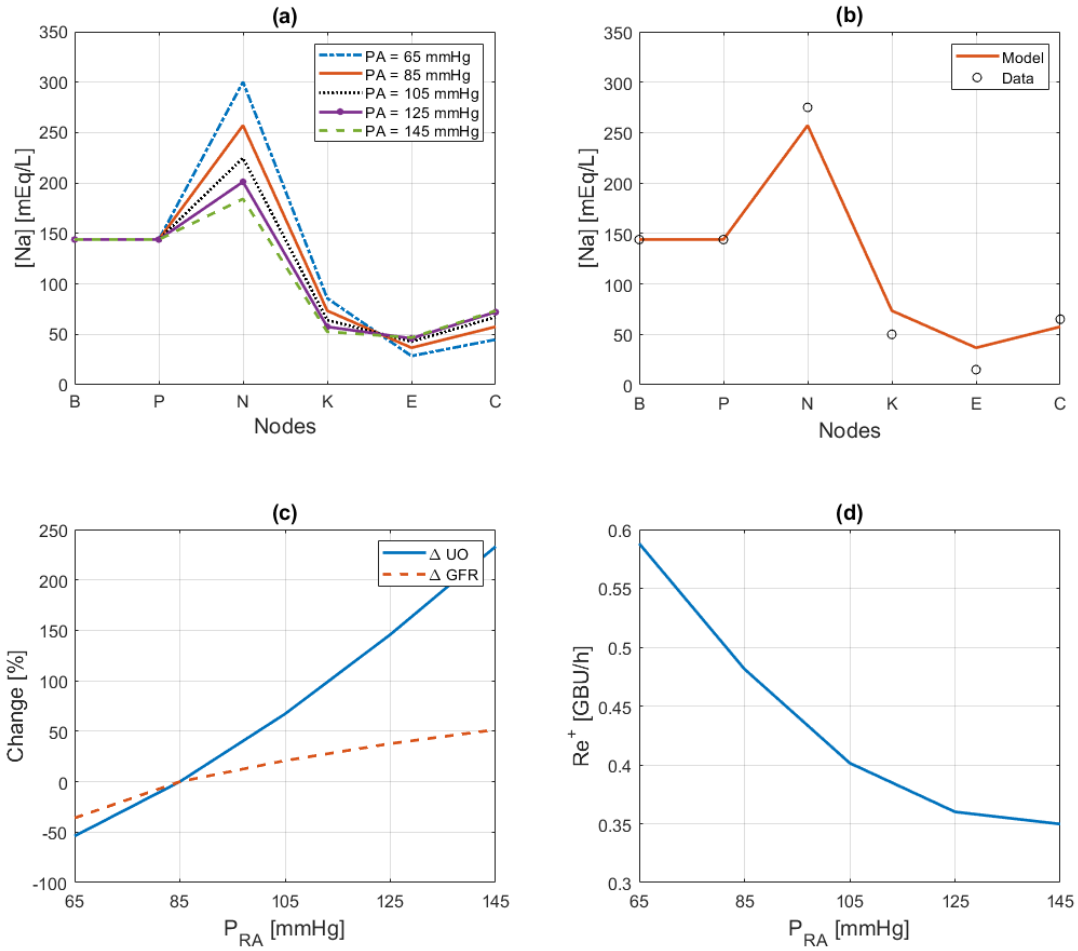

Fig. 5.4: Fig. 5.4, (a): sodium concentration at nodes of the nephron for different renal arterial pressures, (b) nominal sodium concentration at nodes of the nephron against data from Layton and Layton, (c) variation in UO and GFR against change in renal arterial pressure, (d) renin release rate for different renal arterial pressures.

5.6 Optimization: Training for Three Species

In chapters three and four, we discussed how the model's parameters were divided into constant (n=34) and subject-specific (n=24) groups. By conducting regularized optimization, we reduced the number of subject-specific parameters to 12 for sheep and

seven for human subjects. We set the rest of the parameters to constant values derived from their respective population-average models.

Here, since we have integrated new modules that might affect the predictions for the insensitive subject-specific parameters as well, we used the entire set of subject-specific parameters from before and added the new set of subject-specific parameters from the CV, RAAS and new renal function models to them. We estimated the values of the new set of subject-specific parameters (n=46) by fitting the mathematical model to the measurements available in the dataset while fixing subject-invariant parameters to respective pre-specified values. Using this method, we trained and internally validated the expanded model across three species with severe burn injuries: sheep, pigs, and human subjects. Sheep and pigs are large mammals that are regularly used as a replacement for human subjects in pre-clinical and exploratory experiments owing to their physiological and anatomical similarities to us [154], [155].

We estimated the subject-specific parameters on the individual basis by fitting our mathematical model to all the available measurements associated with each subject for every species to minimize the following cost function:

$$\breve{\theta}_i = \arg\min_{\breve{\theta}} \breve{J}_i(\breve{\theta}) = \arg\min_{\breve{\theta}} \sqrt{\sum_{j=1}^{M_i} \left(\sum_{k=1}^{D_{ij}} \frac{\left| y_{ij}^d(t_k) - y_{ij}(t_k, \breve{\theta}) \right|}{Y_{ij}} \right)^2} \tag{5.85}$$

where $\breve{\theta}$ is the vector of sensitive subject-specific parameters, and $\breve{\theta}_i$ is $\breve{\theta}$ estimated for the subject i., M_i is the number of physiological variables measured in the subject i (for instance, M_i=5 for sheep since we fit on UO, HCT, CVP, MAP, and CO data), D_{ij} is the number of measurements associated with the physiological variable j in the subject i during the initial 48 hours, $y_{ij}^d(t_k)$ is the value of the physiological variable j

associated with the subject i measured at time t_k, $y_{ij}(t_k, \theta)$ is the value of the same physiological variable at time t_k predicted by the mathematical model for a given θ, and Y_{ij} is the normalization factor for the physiological variable j. The optimization settings were similar to what was described in section 3.2.2.

5.6.1 Training for Sheep Subjects

Out of the 16 sheep subjects introduced in section 3.1, we used the first nine which had rich CV measurements (that were previously unutilized) to train and validate the model. This time we examine the model's prediction accuracy not just for HCT and UO, but also for CVP, MAP, and CO, by training the model using Eq. (5.85) (M_i=5). For sheep, since we set the initial values of CO and MAP to their baseline measurements, the number of subject-specific parameters was reduced to 44. On average, every sheep subject has 112 datapoints that could be utilized to identify the unknown parameters.

5.6.2 Training for Pig Subjects

The porcine experiment, fully explained in chapter 6, was dedicated to identifying new biomarkers for burn resuscitation. Still, since the subjects had extensive burn injuries (TBSA=40%) and UO, HCT, MAP, CO, CVP, and $[Na^+]$ were measured, the dataset was also suitable for mathematical modeling. In particular, the $[Na^+]$ measurements presented an opportunity to test the sodium dynamic predictions. The subjects in this experiment were randomly assigned to be either under-resuscitated (P1), adequately resuscitated (P2), or over-resuscitated (P3). We used a subset of 15 subjects out of the 21 subjects in the dataset (five from each resuscitation group) to estimate the 46

subject-specific parameters by fitting to UO, MAP, CO, CVP, and $[Na^+]$ by optimizing the objective function in Eq. (5.85). We eliminated HCT from this analysis, because the subjects were not splenectomized, as opposed to sheep subjects, rendering HCT's response to burn injury unreliable. On average, the pig subjects have 94 data points that we can use to identify the unknown parameters.

5.6.3 Training and Testing for Human Subjects

We used the 120 subjects in the training set from chapter 4 for training and internal validation of the expanded model and estimated the unknown parameters by fitting on UO (M_i=1) using Eq. (5.85). Since the ratio of the number of parameters to data points is large (46 to 23±2) for human subjects, we then performed sensitivity analysis using the regularized population-average model (similar to the procedure in section 4.2.3) to reduce the number of subject-specific parameters and avoid overfitting.

Using the reduced model, we externally validated the model for the test set (N=113) subjects and compared the prediction accuracy to the original model.

5.7 Results

5.7.1 Sheep Subjects

Table 5.1 summarizes NMAE, correlation coefficient, and the Bland-Altman statistics associated with HCT, CVP, CO, MAP, and UO predicted by the mathematical model, and their corresponding experimental measurements. Fig. 5.5 presents representative examples of measured versus model-predicted responses of four sheep subjects. Fig.

5.6 presents the behaviors of some of the relevant CV, RAAS, and kidney function responses to burn injury and resuscitation after being averaged across the nine sheep subjects.

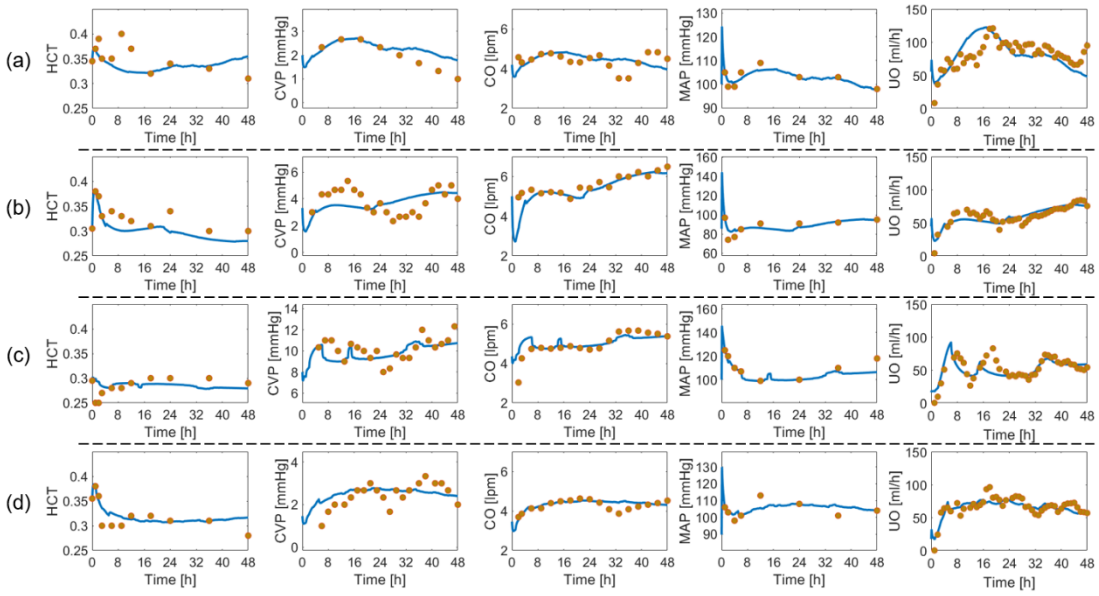

Fig. 5.5: Each row shows the predictions for a particular sheep subject against its measured data. In each plot, the solid blue line represents the prediction, while the gold circles represent data.

Table 5.1: Sheep, normalized mean absolute error (NMAE; reported in median (IQR)), correlation coefficient (r), and Bland-Altman limits of agreement (LoA) associated with HCT: hematocrit, CVP: central venous pressure, CO: cardiac output, MAP: mean arterial pressure, UO: urinary output. LoA: 95% limits of agreement (bias+/-2×SD).

	HCT [.]	CVP [mmHg]	CO [lpm]	MAP [mmHg]	UO [ml/h]
NMAE [%]	16.8 (13.4)	19.1 (8.7)	13.4 (8.6)	16.1 (8.4)	15.7 (6.1)
r	0.85	0.62	0.83	0.83	0.55
LoA	0.003 ±0.05	-0.18±2.5	0.1±0.97	-1.96±12.75	-3.8±45

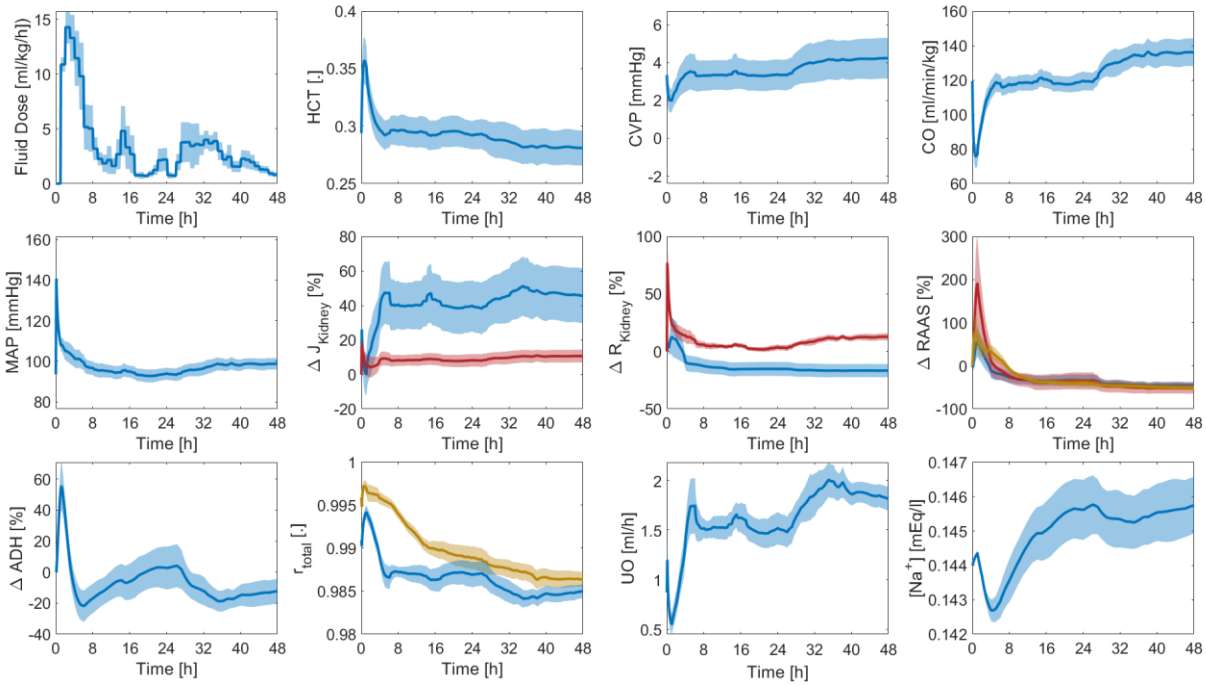

Fig. 5.6: Averaged responses for the nine sheep subjects, where the solid lines represent the mean, and the shaded areas represent the standard error. $\Delta J_{Kidneys}$ plots the percentage deviation from baseline for the GFR (blue), and RPF (red). $\Delta R_{Kidneys}$ plots the percentage deviation from baseline for the efferent resistance (blue), and afferent resistance (red). $\Delta RAAS$ plots the percentage deviation from baseline for renin concentration (blue), angiotensin concentration (red), and aldosterone concentration (gold). r_{total} plots the variation in total water reabsorption fraction (blue), and total sodium reabsorption fraction (gold).

5.7.2 Pig Subjects

Table 5.2 summarizes NMAE, correlation coefficient, and the Bland-Altman statistics associated with CVP, CO, MAP, UO, and $[Na^+]$ as predicted by the mathematical model, and their corresponding experimental measurements. Fig. 5.7, 5.8, and 5.9 each present representative examples of measured versus model-predicted responses of two pig subjects in the un-resuscitated (P1) group, adequately resuscitated (P2) group, and over-resuscitated (P3) group, respectively. Fig. 5.10, 5.11, and 5.12 present the behaviors of some of the relevant CV, RAAS, and kidney function responses to burn

injury and resuscitation after being averaged across the five pig subjects in the un-resuscitated group, adequately resuscitated group, and over-resuscitated group, respectively.

Table 5.2: Pigs, normalized mean absolute error (NMAE; reported in median (IQR)), correlation coefficient (r), and Bland-Altman limits of agreement (LoA) associated with CVP: central venous pressure, CO: cardiac output, MAP: mean arterial pressure, UO: urinary output, $[Na^+]$: plasma sodium concentration. LoA: 95% limits of agreement (bias+/-2×SD).

	CVP [mmHg]	CO [lpm]	MAP [mmHg]	UO [ml/h]	$[Na^+]$ [mEq/l]
NMAE [%]	14.2 (5.1)	16.4 (10)	14.43 (6.8)	15.11 (6.5)	15.61 (11)
r	0.86	0.79	0.84	0.74	0.81
LoA	-0.14±3.05	0.04±0.90	-0.91±16.53	3.08±32.34	0.21±3.04

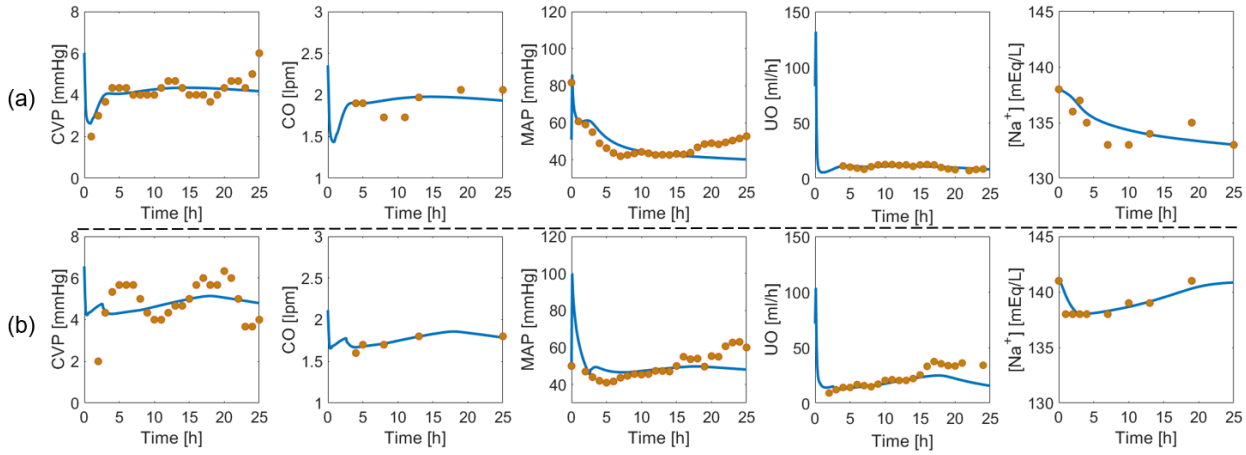

Fig. 5.7: Each row shows the predictions for one pig subject in the un-resuscitated group against its measured data. In each plot, the solid blue line represents the prediction, while the gold circles represent data.

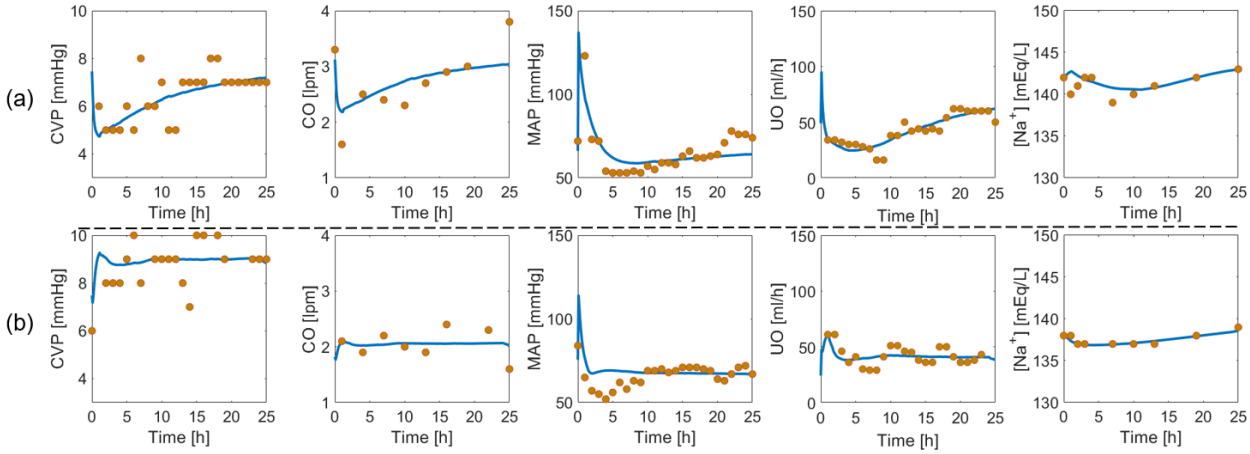

Fig. 5.8: Each row shows the predictions for one pig subject in the adequately resuscitated group against its measured data. In each plot, the solid blue line represents the prediction, while the gold circles represent data.

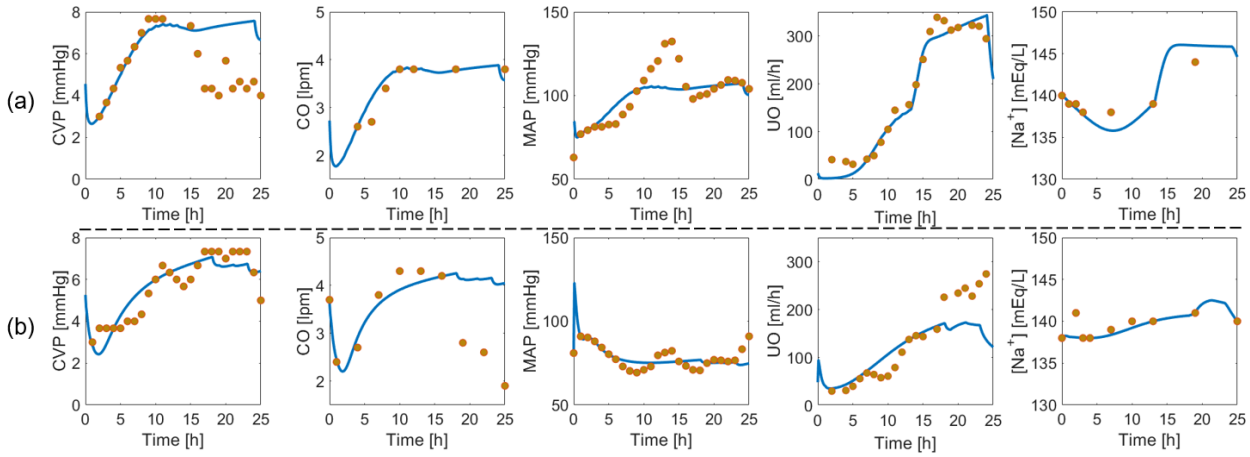

Fig. 5.9: Each row shows the predictions for one pig subject in the over-resuscitated group against its measured data. In each plot, the solid blue line represents the prediction, while the gold circles represent data

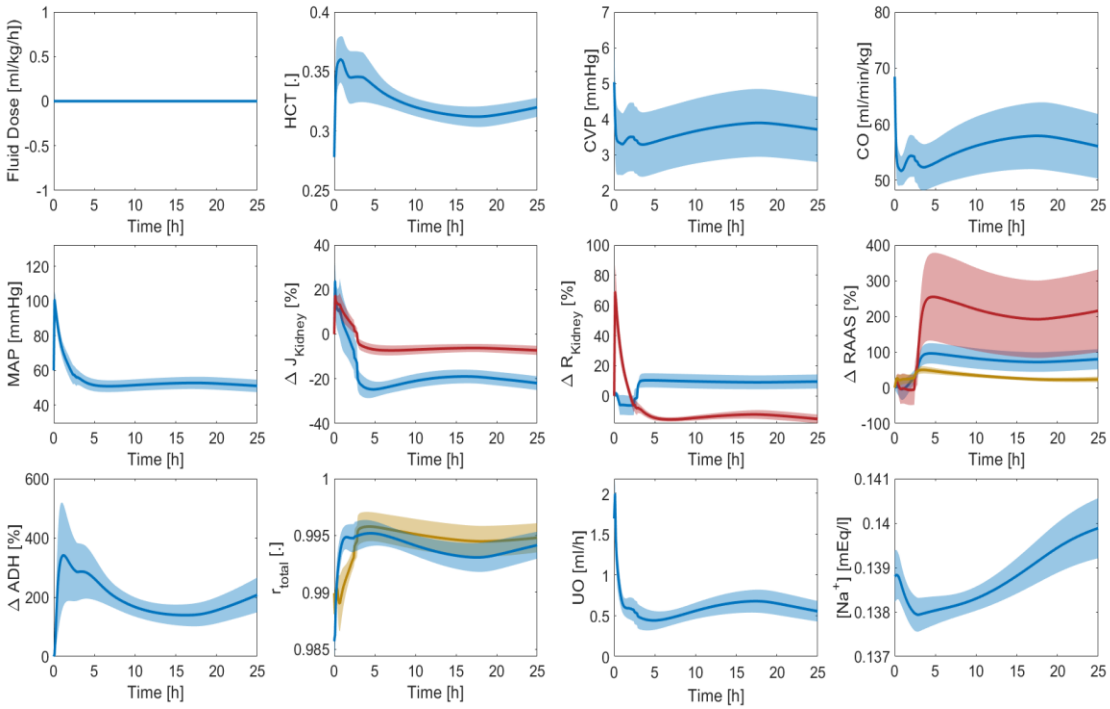

Fig. 5.10: Averaged responses for the five pig subjects in the un-resuscitated group, where the solid lines represent the mean, and the shaded areas represent the standard error. $\Delta J_{Kidneys}$: percentage deviation from baseline for the GFR (blue), and RPF (red). $\Delta R_{Kidneys}$: percentage deviation from baseline for the efferent resistance (blue), and afferent resistance (red). $\Delta RAAS$: percentage deviation from baseline for renin concentration (blue), angiotensin concentration (red), and aldosterone concentration (gold). r_{total}: variation in total water reabsorption fraction (blue), and total sodium reabsorption fraction (gold).

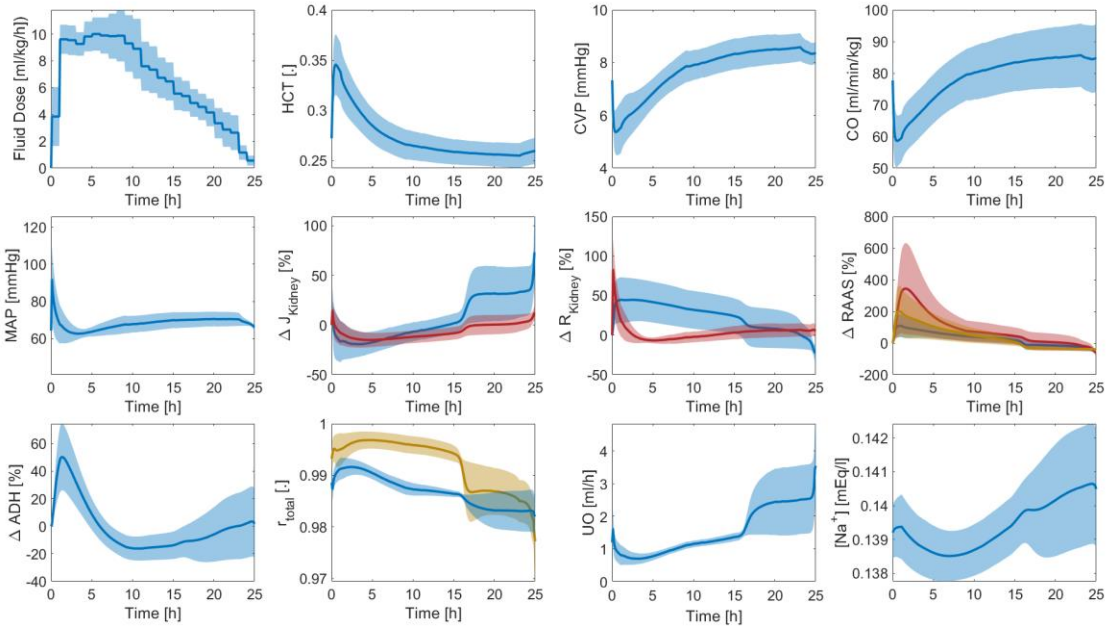

Fig. 5.11: Averaged responses for the five pig subjects in the adequately resuscitated group, where the solid lines represent the mean, and the shaded areas represent the standard error. $\Delta J_{Kidneys}$: percentage deviation from baseline for the GFR (blue), and RPF (red). $\Delta R_{Kidneys}$: percentage deviation from baseline for the efferent resistance (blue), and afferent resistance (red). $\Delta RAAS$: percentage deviation from baseline for renin concentration (blue), angiotensin concentration (red), and aldosterone concentration (gold). r_{total}: variation in total water reabsorption fraction (blue), and total sodium reabsorption fraction (gold).

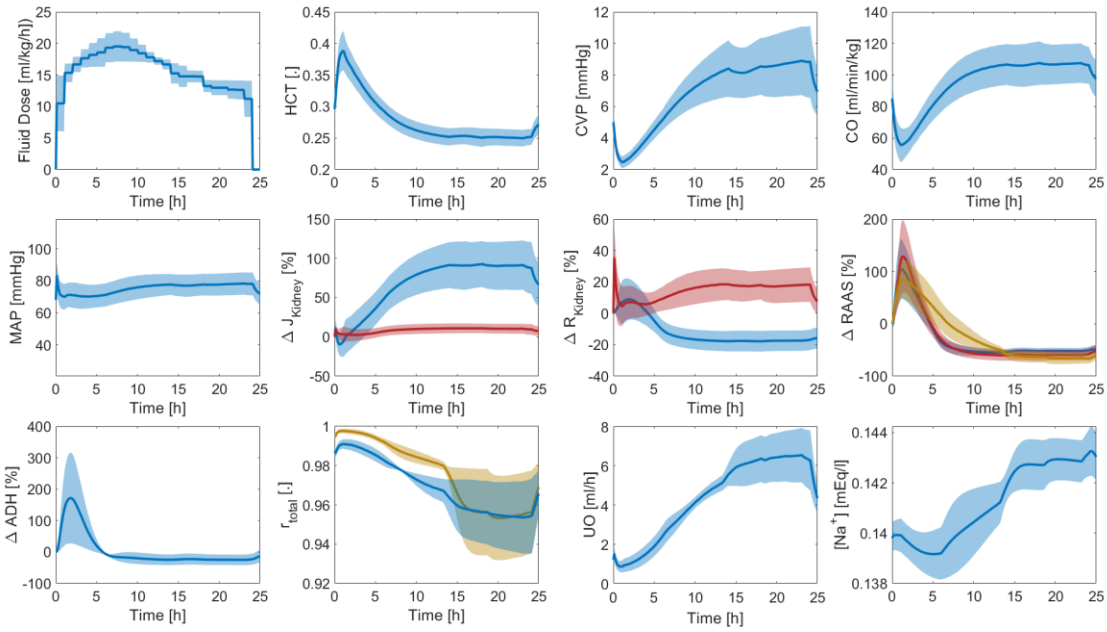

Fig. 5.12: Averaged responses for the five pig subjects in the over-resuscitated group, where the solid lines represent the mean, and the shaded areas represent the standard error. $\Delta J_{Kidneys}$: percentage deviation from baseline for the GFR (blue), and RPF (red). $\Delta R_{Kidneys}$: percentage deviation from baseline for the efferent resistance (blue), and afferent resistance (red). $\Delta RAAS$: percentage deviation from baseline for renin concentration (blue), angiotensin concentration (red), and aldosterone concentration (gold). r_{total}: variation in total water reabsorption fraction (blue), and total sodium reabsorption fraction (gold).

5.7.3 Human Subjects

Table 5.3 summarizes NMAE, correlation coefficient, and the Bland-Altman statistics associated with UO predicted by the mathematical model, and their corresponding experimental measurements in humans for the training and test sets for both the expanded and original models. Fig. 5.13 presents representative examples of measured versus model-predicted responses of eight human subjects similar to Fig. 4.2. Fig. 5.13 presents the behaviors of some of the relevant CV, RAAS, and kidney function responses to burn injury and resuscitation after being averaged across 120 human subjects.

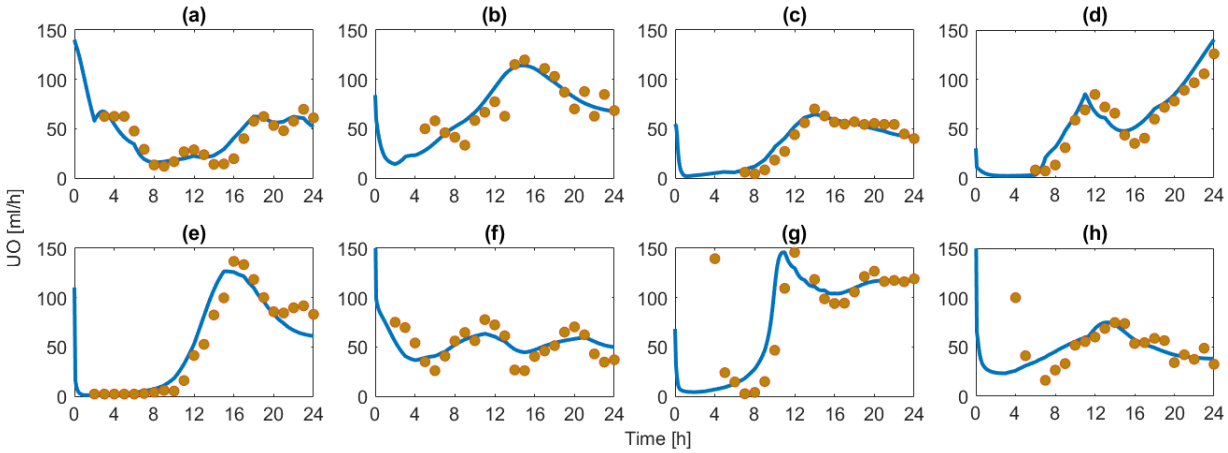

Fig. 5.13: Actual versus model-predicted urinary output (UO) responses of eight burn patients associated with various injury severity and weight. Circles: actual UO. Solid lines: model-predicted UO. (a) TBSA 27% with 80 kg weight. (b) TBSA 36% with 66 kg weight. (c) TBSA 46% with 90 kg weight. (d) TBSA 60% with 71 kg weight. (e) TBSA 24% with 81 kg weight. (f) TBSA 35% with 94 kg weight. (g) TBSA 50% with 89 kg weight. (h) TBSA 60% with 102 kg weight.

Table 5.3: Humans, normalized mean absolute error (NMAE; reported in median (IQR)), correlation coefficient (r), and Bland-Altman limits of agreement (LoA) associated with UO: urinary output, LoA: 95% limits of agreement (bias+/-2×SD).

	Original Model		Expanded Model	
	Training (N=120)	Test (N=113)	Training (N=120)	Test (N=113)
NMAE [%]	14.8 (6.0)	15.4 (6.0)	13.15 (5.5)	11.20 (6.0)
r	0.67	0.82	0.69	0.85
LoA	-3±57	-2±45	0.94±43	0.34±36

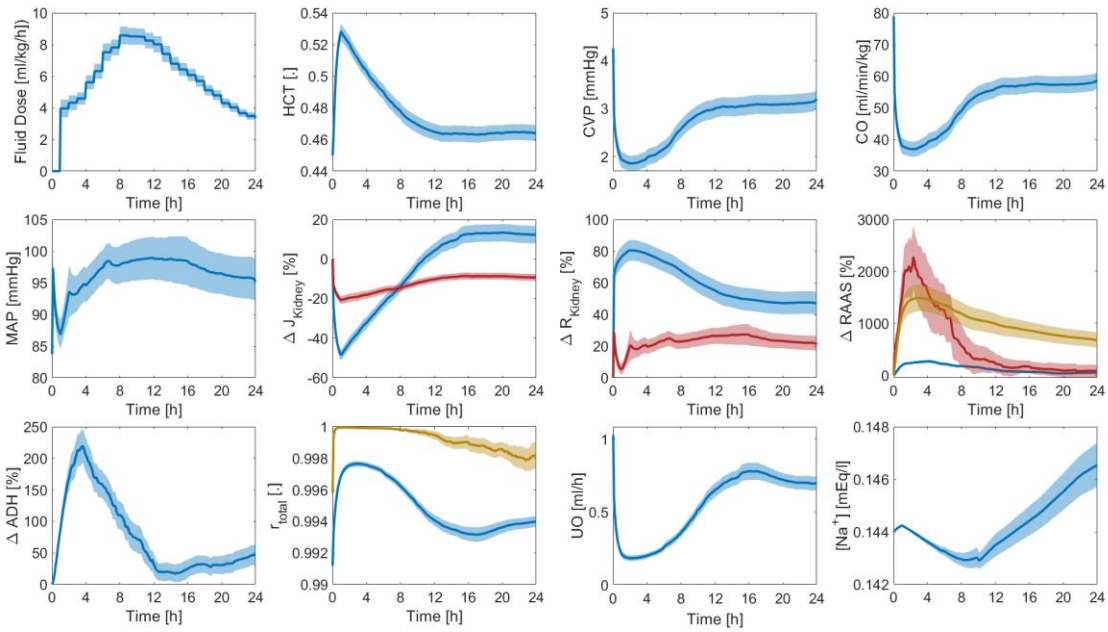

Fig. 5.14: Averaged responses for the 120 human subjects in the training set, where the solid lines represent the mean, and the shaded areas represent the standard error

5.8 Discussion

5.8.1 Sheep Subjects

Fig. 5.5 shows that the mathematical model can predict HCT, CVP, CO, MAP, and UO with reasonable accuracy and capture the inter-subject variability for subjects with similar resuscitation protocols and injury severity. Even though we are optimizing the

fit on five complex variables that often expose the multi-objective optimization problem to trade-offs, the NMAE for UO and HCT (equivalent to PV in Table 3.3) decreased compared to the original model (Table 5.1); however, the interquartile range widened (~6% vs. ~3% in Table 3.3), which means the performance is not as consistently good as before for these two variables.

In general, all the predictions exhibit good tracking of their corresponding measured counterparts in terms of NMAE, correlation coefficient, and LoA. UO has the lowest correlation with data. While 0.55 is only a moderate correlation, there was 76% agreement between measured and predicted UO in terms of residing in the same range (<0.5ml/h/kg, 0.5-1.0ml/h/kg, and >1.0ml/h/kg) on the average. This is an encouraging performance given that current burn resuscitation protocols adjust resuscitation dose based on UO range rather than its value.

In addition to these five variables, we want to ensure all the model's internal variables agree with current knowledge of physiology and burn pathophysiology and that the model assumptions are correctly implemented. Fig. 5.6 shows the predictions corresponding to relevant CV, RAAS, and complex renal function model variables averaged for the nine sheep subjects. The HCT increases immediately post-burn, due to hypovolemia, which is also reflected by a drop in CVP and CO. All three variables recover to baseline values and even show signs of over-resuscitation, which we can see as a common theme in the experimental data as well (Fig. 5.6).

MAP, however, increases despite the lowered CO due to the vasoactive effects of inflammatory agents, but on average, it eventually recovers. This increase in MAP causes a transient increase in GFR, RPF (blue and red, respectively, in ΔJ_{Kidney}), and

UO, followed by an immediate decline to sub-normal values due to hypovolemia, and finally, ascending to above-normal values as the subject undergoes mild over-resuscitation. GFR shows a sustained increase more extreme than the other variables because it is also affected by plasma albumin dilution (see chapter 4, section 4.4). The efferent resistance (blue in ΔR_{Kidney}) decreases to reduce the increased GFR, and the afferent resistance (red in ΔR_{Kidney}) increases to reduce both RPF and GFR back to baseline. The three components of the RAAS are plotted as the percentage of deviation from the baseline in $\Delta RAAS$. As expected, all three elements increase in response to the initial decline in GFR (increased renin release in response to lowered GFR and $[Na^+]_{MD}$) and then decrease, which facilitates the decrease in the efferent resistance, as well as reducing the sodium and water reabsorption, to rid the body of its excess water and to lower blood pressure. This is reflected in the reduced total sodium reabsorption fraction (gold line in r_{total}). The decline in the total water reabsorption fraction is a product of the RAAS and the decrease in ADH levels. As a result, UO increases and stays above the normal range. The plasma sodium concentration ($[Na^+]$) increases, despite the lowered aldosterone and total sodium reabsorption fraction. This is because the pure water reabsorption regulated by ADH is reduced. This agrees with Guyton's findings that pure water reabsorption is a more critical determinant of $[Na^+]$ than aldosterone [147]. Overall, the model trained for sheep performs well both in prediction accuracy and the plausibility of the internal mechanisms and variables. The model predicted all these variables while being characterized with physiologically acceptable parameter values (Table 5.4).

5.8.2 Pig Subjects

One of the limitations of the original model trained for sheep was that the animals were very similar in resuscitation protocols (all resuscitated toward the end-point of 0.5-1 ml/kg/hr UO). The porcine dataset, therefore, provided us with an excellent opportunity to train the model for large mammals resuscitated with vastly different protocols and test its capability to reflect the difference, which is the ultimate goal of this work. Another opportunity was the addition of the measured $[Na^+]$ which we could use to train and validate the electrolyte balance components of the model. Table 5.2 summarizes the accuracy metric for CVP, CO, MAP, UO, and $[Na^+]$ predictions. The model performed consistently well, with small NMAE and strong correlations for all the variables, even the UO which is inherently difficult to predict accurately as it depends on so many mechanisms. More than 91% of the time, the predicted and measured UO resided in the same operational range (<1ml/h/kg, 1-1.5ml/h/kg, and >1.5ml/h/kg).

Fig. 5.7 represents two examples of the subjects in the un-resuscitated group. While both subjects show signs of hypovolemia throughout the experiment, the intensity of the response to burn injury and the level of self-recovery provided by the body's safety factors against hypovolemia and edema are different. For instance, the subject in Fig. 5.7 (a) experiences more pronounced declines in CVP, CO, MAP, and UO and sharper recoveries.

Fig. 5.8 presents two examples of the subjects resuscitated with P2. While the subject in (a) has recovered to baseline by the end of the experiment, subject (b) shows signs of mild over-resuscitation despite goal-directed therapy. The subjects in Fig. 5.9 (a)

and (b), which belong to P3, are over-resuscitated according to the prediction and resuscitation protocol; however, for CVP in (a) and CO in (b), the experimental measurements suggest recovery to baseline values and even falling below the baseline. The model cannot replicate this drop in CVP and CO, primarily because the subjects are aggressively over-resuscitated with high doses of fluid, which is also reflected in their UO measurements. The model has no mechanism to explain why CO and CVP would drop at this point. One possible explanation for the drop in CO could be lowered heart rate, which we do not have a module for in the model.

Fig. 5.10, 5.11, and 5.12 present the averaged responses to burn and resuscitation in the CV, RAAS, and renal function modules. Despite the large inter-subject variability, reflected by the width of standard error bands in some of the plots, the model was able to distinguish the responses in the three paradigms and suggest mechanisms to explain their differences. The HCT increases immediately post-burn in all three paradigms, and while it stays there for the un-resuscitated group (Fig. 5.10), it declines for both the adequately-resuscitated and over-resuscitated groups. For P2, the inter-subject variability means that the subject was either recovered or slightly over-resuscitated towards the end of the experiment. For P3, all subjects are over-resuscitated, but with varying degrees of severity. The CO, CVP, GFR (blue in ΔJ_{Kidney}), RPF (red in ΔJ_{Kidney}), and UO predictions for the three paradigms mirror the behavior predicted for the HCT, i.e., initial decline due to hypovolemia, continued subnormal values for P1, a range of recovery to hypervolemia for P2, and varying degrees of over-resuscitation for subjects in P3.

While MAP is below normal for P1, it cannot distinguish P2 and P3, which agrees with studies suggesting that MAP is not a good end-point for fluid resuscitation [156]. The efferent resistance (blue in ΔR_{Kidney}) and the afferent resistance (red in ΔR_{Kidney}) vary to regulate the GFR and RPF. Renin, angiotensin, and aldosterone (blue, red, and gold in $\Delta RAAS$, respectively) increase in P1 to (i) constrict the vessels and increase MAP, (ii) increase the efferent resistance and preserve GFR, and (iii) increase the sodium and water reabsorption fractions (gold and blue lines in r_{total}, respectively) to retain more water and salt and correct the hypovolemic state of the body. The ADH also increases in response to hypovolemia and contributes to increased water reabsorption fraction. For P2 and P3, these hormones and enzymes similarly increase at first to correct the hypovolemia induced by burn, but then reduce as the subject recovers (P2) or gets over-resuscitated (P3).The $[Na^+]$ shows a wide range of behaviors for P1 and P2 but is increased for P3 despite the lowered aldosterone and total sodium reabsorption fraction, due to the reduction in pure water reabsorption, as we also observed for sheep.

Overall, the predictions of the model for pig subjects agree with contemporary knowledge of physiology and burn pathophysiology and could provide insight into the effectiveness of different resuscitation paradigms. The parameter values associated with the porcine model are reported in Table 5.5.

5.8.3 Human Subjects

The regularized individual optimizations for the training set, which penalized deviations from the population-average parameters, suggested 10 parameters as sensitive, subject-specific parameters. Therefore, we were able to reduce the number

of subject-specific parameters from 46 to 10, and then assess the prediction accuracy of the reduced model using the training and test sets.

Table 5.3 summarizes the results and shows that the model predicts the UO for human subjects very well in both training and test sets, and that the prediction accuracy has improved compared to the original model. The NMAE in the test set, for instance, is almost one third (NMAE = 11.20 (6)%) of the prediction error of a recent work that uses a black box model to predict UO (NMAE = 30 (6)%) [73]. This is a very encouraging improvement, especially considering the fact that our physics-based model predicts many other variables consistent with literature, and with feasible, meaningful values for parameters (Table 5.6).

Fig. 5.13 (re-generated from Fig. 4.2) shows that the model, even after being reduced to 10 parameters, captures the inter-subject variability for patients with very similar demographics and injury severities.

Fig. 5.14 represents the average behavior for the training subjects, and similar to the original model, suggests that on the average, the human subjects are still slightly hypovolemic at the end of the 24 hours, which is reflected by above-baseline values for HCT, and below-baseline values for CVP and CO. MAP is predicted to be higher than baseline for the entire 24 hours due to vasoconstriction, which suggests it is not a good indicator of fluid resuscitation on its own, as confirmed by literature [156]. RPF (red in ΔR_{Kidney}) is below normal, similar to CO and CVP, while GFR (blue in ΔR_{Kidney}) is above normal due to plasma albumin dilution as confirmed by experiments [76]. All three components of the RAAS are still above normal at the end of 24 hours but will continue declining if we continue simulating the model to recover normal MAP values.

The total reabsorption fractions for sodium and water (gold and blue lines in r_{total}, respectively) have increased and are above baseline to retain more water and replace the lost PV. Subsequently, the plasma sodium concentration is slightly above normal despite the increased pure water reabsorption.

5.9 Conclusion

In the previous chapters, we developed and extensively validated mathematical models of burn injury and resuscitation for sheep and human subjects. Here, we resolved some of the limitations of the original models, particularly regarding the renal function model and electrolyte dynamics by adding a detailed, mechanistic model of the kidney's intrinsic regulatory mechanisms as well as reabsorption mechanisms. Additionally, we had an opportunity to add the cardiovascular system to the model, which was motivated by the recent interests in hemodynamic monitoring of burn patients. We also added the renin-angiotensin-aldosterone system which is directly relevant to both the renal function and CV system.

Using nine sheep subjects from chapter three and a new set of 15 pig subjects with severe burn injury resuscitated with different protocols (chapter 6), we extensively validated the new components of the model, and showed that it not only predicts HCT, CVP, CO, MAP, UO, and $[Na^+]$ with reasonable accuracy, but also provides insight into the burn resuscitation effectiveness in restoring VK, CV, and renal function variables. The model also predicts the UO responses of the 233 human subjects very accurately, while also predicting the internal and clinically significant variables consistent with the literature.

To the best of our knowledge, this is the first time in the field that we can do hypothesis testing for burn injury and resuscitation using a model that includes the VK, renal function, CV, and RAAS modules, and has been extensively validated across three species, and particularly for a large and diverse set of human subjects with significant inter-subject variability.

In the future, we can use the model to generate virtual patients for in-silico testing of new resuscitation protocols and decision support systems, as well as for training purposes, particularly for sheep and pig subjects that are validated using a rich dataset. These large mammals are regularly used for pre-clinical, in-vivo testing of new therapies, which is time-consuming, and imposes financial and ethical costs. A credible and transparent mathematical model could essentially replace or complement the pre-clinical stages of developing new resuscitation algorithms via predicting realistic variables, and even relevant burn injury variables that are not measurable but could be very insightful, such as the resuscitation effectiveness that we discussed in chapter 4.

5.10 Model Parameters: Nomenclature, Definitions, and Values

Table 5.4: Mathematical model parameters for sheep: definitions, categories (I/S), and values. I: subject-invariant parameters. S: subject-specific parameters. Parameter values are given as mean, median (IQR), or mean+/-SD.

Symbol	Definition	I/S	Value (Model)	Value (Literature)
$\overline{BV}$	Nominal blood volume [ml/kg]	I	63.5	63.5 [80]
$\bar{V}_P$	Nominal water volume in plasma [ml/kg]	I	42.8	42 [81]-46 [36]
r_{FV}	Skin fluid volume to total interstitial fluid volume ratio [·]	I	0.28	0.28 [36]
$\bar{V}_{BT}$	Nominal water volume in burnt tissue [ml/kg]	I	$120\varepsilon_B r_{FV}$	$120\varepsilon_B r_{FV}$ [36]
$\bar{V}_{IT}$	Nominal water volume in intact tissue [ml/kg]	I	$120(1-\varepsilon_B r_{FV})$	$120(1-\varepsilon_B r_{FV})$ [36]
$[\bar{A}_P]$	Nominal albumin concentration in plasma [g/ml]	I	0.059	0.059 (0.004) [67]
$[\bar{A}_{BT}]$	Nominal albumin concentration in burnt tissue [g/ml]	I	0.028	0.028 [67]
$[\bar{A}_{IT}]$	Nominal albumin concentration in intact tissue [g/ml]	I	0.028	0.028 [67]
$\bar{A}_P$	Nominal albumin content in plasma [g]	I	$[\bar{A}_P]\bar{V}_P$	-
$\bar{A}_{BT}$	Nominal albumin content in burnt tissue [g]	I	$[\bar{A}_{BT}]\bar{V}_{BT}$	-
$\bar{A}_{IT}$	Nominal albumin content in intact tissue [g]	I	$[\bar{A}_{IT}]\bar{V}_{IT}$	-
$\bar{J}_C$	Nominal capillary filtration [ml/kg·h]	S	2.1 (0.63)	1.72 [79]
C_O	Colloid oncotic pressure constant [mmHg/g·ml]	I	250	250 [67]
$\bar{J}_L$	Nominal total lymphatic flow to plasma [ml/kg·h]	I	1.07 (0.19)	1.08 [36]
$\bar{J}_{L,BT}$	Nominal lymphatic flow from burnt tissue to plasma [ml/kg·h]	I	$\bar{J}_L\varepsilon_B r_{FV}$	$\bar{J}_L\varepsilon_B r_{FV}$ [36]
$\bar{J}_{L,IT}$	Nominal lymphatic flow from intact tissue to plasma [ml/kg·h]	I	$\bar{J}_L(1-\varepsilon_B r_{FV})$	$\bar{J}_L(1-\varepsilon_B r_{FV})$ [36]
C_L	Lymphatic maximal increase coefficient [·]	S	0.21 (0.18)	-
S_L	Lymphatic pressure sensitivity coefficient [1/mmHg]	S	5.58 (1.46)	-
$\bar{P}_C$	Nominal hydrostatic capillary pressure [mmHg]	S	7.0 (0.47)	6.7 (0.8) [82]
E_C	Capillary elastance [mmHg/ml]	S	0.0031 (0.0002)	0.0097 [37]
α	Tissue electrostatic pressure coefficient [mmHg]	I	10	10 [45]
γ	Tissue tension pressure coefficient [mmHg]	I	3.75	3.75 [45]
$\hat{y}$	Maximum half-thickness of the extracellular matrix [·]	I	4	4 [45]
$\check{y}$	Minimum half-thickness of the extracellular matrix [·]	I	1	1 [45]
$\hat{R}$	Maximum GAG radius [·]	I	3.5	3.5 [45]
β	Radius threshold ratio [·]	I	0.23	0.23 [45]
n	Hydration response coefficient [·]	I	8	2-8 [45]
$\bar{W}_X$	Nominal hydration level [ml/g]	I	0.66	0.23-0.81 [45], [46]
$\bar{J}_{RPF}$	Nominal renal plasma flow [ml/kg·h]	I	536	536 [83]
P_B	Hydrostatic pressure in Bowman's capsules [mmHg]	I	18	18 [47]
K_G	Glomerular filtration coefficient [ml/kg·h·mmHg]	S	9.2 (1.2)	9.6-12.0 [84]
K_{ADH}	Nominal ADH secretion rate [pg/kg·h]	I	287	287 [54], [55]
λ_{V_P}	ADH sensitivity to plasma volume change [1/ml]	S	0.002 (0.0008)	-
$\lambda_{[Na^+]}$	ADH sensitivity to sodium concentration change [ml/mEq]	S	110.45 (98)	-
$[\overline{Na^+}]$	Nominal plasma sodium concentration [mEq/l]	I	142	142 [85]
$\hat{Q}_{PD}$	Protein influx post burn [g/h]	S	72.98 (53.23)	-
λ_{PD}	Protein influx decay rate [1/h]	S	9.23 (6.28)	-
$M_{P_{BT}}$	Maximum burnt tissue hydrostatic pressure perturbation [mmHg]	S	38	30 [56]
$\lambda_{1,P_{BT}}$	Burnt tissue hydrostatic pressure perturbation slow decay rate [1/h]	S	5.48	-
μ	The ratio between slow decay rate to fast decay rate [·]	S	356	-
$\lambda_{2,P_{BT}}$	Burnt tissue hydrostatic pressure perturbation fast decay rate [1/h]	I	$8\lambda_{1,P_{BT}}$	-
$K_{1,EV}$	Nominal tissue evaporation rate [ml/h·m^2]	I	18.48	18.48 [63]
$\lambda_{1,EV}$	Evaporation growth rate [1/h]	I	0.073	0.073 [63]
$K_{2,EV}$	Maximum evaporation rate [ml/h·m^2]	I	28.68	28.68 [63]
$\lambda_{2,EV}$	Evaporation decay rate [1/h]	I	-0.0052	-0.0052 [63]
ε_B	Fraction of body surface subject to burn [·]	S	0.3-0.4	dataset
S_B	Total body surface area [m^2]	I	1	1.07+/-0.16 [86]
K_{EX}	Maximum exudation rate [ml/h·m^2]	I	25	25 [62]

λ_{EX}	Exudation decay rate [1/h]	I	-0.0038	-0.0038 [62]
η_{EX}	Exudate to tissue albumin ratio [·]	S	0.69	0.75 [36]
$\bar{\alpha}$	Nominal albumin to capillary pore radius ratio [·]	S	0.82	0.7-0.9 [37]
$1-k_{PD,BT}$	Capillary destruction fraction [·]	S	0.56	0.50 [35]
$M_{\alpha_{BT}}$	Maximum pore ratio perturbation in burnt tissue [·]	S	0.37	0.30 [39]
$M_{\alpha_{IT}}$	Maximum pore ratio perturbation in intact tissue [·]	S	0.16 (0.11)	0.19 [87]
$\lambda_{1,\alpha}$	Pore ratio slow decay rate [1/h]	S	0.030	0.025 [36]
$\lambda_{2,\alpha}$	Pore ratio fast decay rate [1/h]	I	$\mu\lambda_{1,\alpha}$	-
M_{P_C}	Maximum capillary hydrostatic pressure perturbation [mmHg]	S	19 (12)	23+/-5 [61]
λ_{1,P_C}	Capillary hydrostatic pressure perturbation slow decay rate [1/h]	SS	0.54 (0.08)	-
λ_{2,P_C}	Capillary hydrostatic pressure perturbation fast decay rate [1/h]	I	$\mu\lambda_{1,P_C}$	-
λ_{msp}	Mean systemic pressure sensitivity [1/ml]	S	0.83 (0.24)	-
K_{TPR}	Total peripheral resistance coefficient [.]	S	5.05 (6.23)	-
λ_{TPR}	Total peripheral resistance coefficient [ml/ng]	S	7.34 (12.75)	-
$\overline{[Ang\ II]}$	Nominal angiotensin II plasma concentration [ng/ml]	I	0.027	0.027 [127]
CO_{max}	Maximum cardiac output [mmHg]	S	3.50 (1.58)	-
$\overline{MAP}$	Nominal mean arterial pressure [mmHg]	S	94.42 (11.35)	90 [139]
$\overline{\mathrm{CO}}$	Nominal cardiac output [lpm]	S	4.86 (0.99)	2-5 [67]
M_{MAP}	Maximum mean arterial pressure perturbation [mmHg]	S	1.75 (0.53)	-
$\lambda_{1MAP,}$	MAP slow decay rate [1/h]	S	0.85 (0.26)	-
$\lambda_{2,MAP,}$	MAP fast decay rate [1/h]	S	$\mu\lambda_{1MAP,}$	-
$\overline{CVP}$	Nominal central venous pressure [mmHg]	S	2.44 (2.22)	1-6 [67]
K_{RA}	Renal arterial pressure coefficient [.]	S	0.50 (0.92)	-
K_{RV}	Renal vein pressure coefficient [.]	S	0.96 (0.65)	-
$R_{A,0}$	Constant afferent resistance [mmHg.min/ml]	I	0.0293/W	Scaled from [139]
P_{ref}	Reference renal arterial pressure for myogenic mechanism [mmHg]	I	74	Scaled from [139]
G_{MM}	Myogenic Mechanism scaling coefficient [.]	I	0.0867	-
K_{TGF}	Coefficient of magnitude for TGF curve [.]	S	1.84 (0.88)	-
λ_{TGF}	Steepness of TGF curve [ml/mEq]	S	17.59 (13.45)	-
$\overline{R_{TGF}}$	Nominal TGF resistance [mmHg.min/ml]	I	0.0079/W	Scaled from [139]
$\overline{R_{Eff}}$	Nominal efferent resistance [mmHg.min/ml]	I	0.0802/W	Scaled from [139]
K_{Eff}	Coefficient of magnitude for efferent resistance curve [.]	S	0.88 (1.09)	-
$\overline{[ALD]}$	Nominal aldosterone concentration in plasma [ng/ml]	I	0.085	0.085 [127]
r_{P_0}	Nominal proximal tubule reabsorption fraction	S	0.65-0.75	0.65-0.8 [51], [127]
λ_N	Descending limb of Henle sensitivity [.]	S	1.91 (1.74)	-
λ_E	Early distal tubule sensitivity [.]	S	2.26 (3.08)	-
$\overline{[Na^+]}$	Nominal plasma sodium concentration [mEq/ml]	I	0.144	[85]
$r_{CW,max}$	Maximum water reabsorption fraction in collecting ducts [.]	I	0.995	-
$r_{CW,min}$	Minimum water reabsorption fraction in collecting ducts [.]	I	0.45	-
$\overline{r_{CW}}$	Nominal water reabsorption fraction in collecting ducts [.]	S	0.94 (0.03)	-
$\overline{[ADH]}$	Nominal ADH concentration [pg/ml]	I	1	1 [51]
$r_{CNa,max}$	Maximum water reabsorption fraction in collecting ducts [.]	I	1	-
$r_{CNa,min}$	Minimum water reabsorption fraction in collecting ducts [.]	I	0.2	-
n_{ALD}	Order of the aldosterone dose-response curve [.]	I	1	-
$\alpha_{UO,Na}$	Ratio of nominal urine sodium concentration to nominal PV sodium concentration	S	0.61 (0.17)	-
Re_0^+	Nominal renin release rate [GBU/hr]	I	0.48	0.48 [127]
Re_0	Nominal renin content in the circulation [GBU]	I	$[Re]_0 V_{PL,0}$	-
$[Re]_0$	Nominal renin concentration in plasma [GBU/ml]	I	0.00006	0.00006 [127]
τ_{ren}	Renin time constant [1/h]	S	0.43 (0.52)	0.05-0.6 [147]
$Ang\ II_0^+$	Nominal Ang II release rate [pg/hr]	I	105*60	105*60 [127]
C_{Ang}	Angiotensin release coefficient [.]	S	0.68 (2.48)	-

ALD_0^+	Nominal aldosterone secretion rate [ng/h]	I	3162	3162 [127]
w_{ALD}	Weight of the effect of $[Na^+]$ on aldosterone secretion [.]	S	0.90 (0.29)	-
$C_{ALD,Na}$	Coefficient of $[Na^+]$ sensitivity for aldosterone secretion [.]	S	36.04 (20.5)	-
K_{ALD}	Coefficient of angiotensin sensitivity for aldosterone secretion [.]	S	2.91 (1.24)	-

Table 5.5: Mathematical model parameters for pig subjects: definitions, categories (I/S), and values. I: subject-invariant parameters. S: subject-specific parameters. Parameter values are given as mean, median (IQR), or mean+/-SD.

Symbol	Definition	I/S	Value (Model)	Value (Literature)
$\overline{BV}$	Nominal blood volume [ml/kg]	I	63.5	63.5 [80]
$\bar{V}_P$	Nominal water volume in plasma [ml/kg]	I	42.8	42 [81]-46 [36]
r_{FV}	Skin fluid volume to total interstitial fluid volume ratio [·]	I	0.28	0.28 [36]
$\bar{V}_{BT}$	Nominal water volume in burnt tissue [ml/kg]	I	$120\varepsilon_B r_{FV}$	$120\varepsilon_B r_{FV}$ [36]
$\bar{V}_{IT}$	Nominal water volume in intact tissue [ml/kg]	I	$120(1-\varepsilon_B r_{FV})$	$120(1-\varepsilon_B r_{FV})$ [36]
$[\bar{A}_P]$	Nominal albumin concentration in plasma [g/ml]	I	0.059	0.059 (0.004) [67]
$[\bar{A}_{BT}]$	Nominal albumin concentration in burnt tissue [g/ml]	I	0.028	0.028 [67]
$[\bar{A}_{IT}]$	Nominal albumin concentration in intact tissue [g/ml]	I	0.028	0.028 [67]
$\bar{A}_P$	Nominal albumin content in plasma [g]	I	$[\bar{A}_P]\bar{V}_P$	-
$\bar{A}_{BT}$	Nominal albumin content in burnt tissue [g]	I	$[\bar{A}_{BT}]\bar{V}_{BT}$	-
$\bar{A}_{IT}$	Nominal albumin content in intact tissue [g]	I	$[\bar{A}_{IT}]\bar{V}_{IT}$	-
$\bar{J}_C$	Nominal capillary filtration [ml/kg·h]	S	1.42 (0.78)	1.72 [79]
C_O	Colloid oncotic pressure constant [mmHg/g·ml]	I	250	250 [67]
$\bar{J}_L$	Nominal total lymphatic flow to plasma [ml/kg·h]	I	1.07 (0.19)	1.08 [36]
$\bar{J}_{L,BT}$	Nominal lymphatic flow from burnt tissue to plasma [ml/kg·h]	I	$\bar{J}_L\varepsilon_B r_{FV}$	$\bar{J}_L\varepsilon_B r_{FV}$ [36]
$\bar{J}_{L,IT}$	Nominal lymphatic flow from intact tissue to plasma [ml/kg·h]	I	$\bar{J}_L(1-\varepsilon_B r_{FV})$	$\bar{J}_L(1-\varepsilon_B r_{FV})$ [36]
C_L	Lymphatic maximal increase coefficient [·]	S	0.17 (0.28)	-
S_L	Lymphatic pressure sensitivity coefficient [1/mmHg]	S	6.11 (1.58)	-
$\bar{P}_C$	Nominal hydrostatic capillary pressure [mmHg]	S	7.29 (1.48)	6.7 (0.8) [82]
E_C	Capillary elastance [mmHg/ml]	S	0.0030 (0.0006)	0.0097 [37]
α	Tissue electrostatic pressure coefficient [mmHg]	I	10	10 [45]
γ	Tissue tension pressure coefficient [mmHg]	I	3.75	3.75 [45]
$\hat{y}$	Maximum half-thickness of the extracellular matrix [·]	I	4	4 [45]
$\check{y}$	Minimum half-thickness of the extracellular matrix [·]	I	1	1 [45]
$\hat{R}$	Maximum GAG radius [·]	I	3.5	3.5 [45]
β	Radius threshold ratio [·]	I	0.23	0.23 [45]
n	Hydration response coefficient [·]	I	8	2-8 [45]
$\bar{W}_X$	Nominal hydration level [ml/g]	I	0.66	0.23-0.81 [45], [46]
$\bar{J}_{RPF}$	Nominal renal plasma flow [ml/kg·h]	I	536	536 [83]
P_B	Hydrostatic pressure in Bowman's capsules [mmHg]	I	18	18 [47]
K_G	Glomerular filtration coefficient [ml/kg·h·mmHg]	S	9.2 (1.2)	9.6-12.0 [84]
K_{ADH}	Nominal ADH secretion rate [pg/kg·h]	I	287	287 [54], [55]
λ_{V_P}	ADH sensitivity to plasma volume change [1/ml]	S	0.0009 (0.0027)	-
$\lambda_{[Na^+]}$	ADH sensitivity to sodium concentration change [ml/mEq]	S	119.4 (176)	-
$[\overline{Na^+}]$	Nominal plasma sodium concentration [mEq/l]	I	142	142 [85]
$\hat{Q}_{PD}$	Protein influx post burn [g/h]	S	111.12 (141)	-
λ_{PD}	Protein influx decay rate [1/h]	S	6.37 (3.34)	-
$M_{P_{BT}}$	Maximum burnt tissue hydrostatic pressure perturbation [mmHg]	S	47.85 (42)	30 [56]
$\lambda_{1,P_{BT}}$	Burnt tissue hydrostatic pressure perturbation slow decay rate [1/h]	S	6.37 (3.34)	-
μ	The ratio between slow decay rate to fast decay rate [·]	S	472 (380)	-
$\lambda_{2,P_{BT}}$	Burnt tissue hydrostatic pressure perturbation fast decay rate [1/h]	I	$8\lambda_{1,P_{BT}}$	-
$K_{1,EV}$	Nominal tissue evaporation rate [ml/h·m^2]	I	18.48	18.48 [63]

$\lambda_{1,EV}$	Evaporation growth rate [1/h]	I	0.073	0.073 [63]
$K_{2,EV}$	Maximum evaporation rate [ml/h·m^2]	I	28.68	28.68 [63]
$\lambda_{2,EV}$	Evaporation decay rate [1/h]	I	-0.0052	-0.0052 [63]
ε_B	Fraction of body surface subject to burn [·]	S	0.66 (0.19)	dataset
S_B	Total body surface area [m^2]	I	1	1.07+/-0.16 [86]
K_{EX}	Maximum exudation rate [ml/h·m^2]	I	25	25 [62]
λ_{EX}	Exudation decay rate [1/h]	I	-0.0038	-0.0038 [62]
η_{EX}	Exudate to tissue albumin ratio [·]	S	0.69	0.75 [36]
$\bar{\alpha}$	Nominal albumin to capillary pore radius ratio [·]	S	0.82	0.7-0.9 [37]
$1-k_{PD,BT}$	Capillary destruction fraction [·]	S	0.56	0.50 [35]
$M_{\alpha_{BT}}$	Maximum pore ratio perturbation in burnt tissue [·]	S	0.37	0.30 [39]
$M_{\alpha_{IT}}$	Maximum pore ratio perturbation in intact tissue [·]	S	0.16 (0.11)	0.19 [87]
$\lambda_{1,\alpha}$	Pore ratio slow decay rate [1/h]	S	0.030	0.025 [36]
$\lambda_{2,\alpha}$	Pore ratio fast decay rate [1/h]	I	$\mu\lambda_{1,\alpha}$	-
M_{P_C}	Maximum capillary hydrostatic pressure perturbation [mmHg]	S	19 (12)	23+/-5 [61]
λ_{1,P_C}	Capillary hydrostatic pressure perturbation slow decay rate [1/h]	S	0.54 (0.08)	-
λ_{2,P_C}	Capillary hydrostatic pressure perturbation fast decay rate [1/h]	I	$\mu\lambda_{1,P_C}$	-
λ_{msp}	Mean systemic pressure sensitivity [1/ml]	S	0.92 (0.38)	-
K_{TPR}	Total peripheral resistance coefficient [.]	S	3.27 (6.86)	-
λ_{TPR}	Total peripheral resistance coefficient [ml/ng]	S	8.67 (16.70)	-
$\overline{[Ang\ II]}$	Nominal angiotensin II plasma concentration [ng/ml]	I	0.027	0.027 [127]
CO_{max}	Maximum cardiac output [mmHg]	S	2.61 (1.30)	-
$\overline{MAP}$	Nominal mean arterial pressure [mmHg]	S	54 (18.2)	50-70 [157]
$\overline{\mathrm{CO}}$	Nominal cardiac output [lpm]	S	3.27 (1.56)	2-4 [157]
M_{MAP}	Maximum mean arterial pressure perturbation [mmHg]	S	1.53 (0.55)	-
$\lambda_{1MAP,}$	MAP slow decay rate [1/h]	S	0.59 (0.58)	-
$\lambda_{2,MAP,}$	MAP fast decay rate [1/h]	S	$\mu\lambda_{1MAP,}$	-
$\overline{CVP}$	Nominal central venous pressure [mmHg]	S	4.07 (1.21)	2-8 [157]
K_{RA}	Renal arterial pressure coefficient [.]	S	0.84 (0.47)	-
K_{RV}	Renal vein pressure coefficient [.]	S	1.05 (0.92)	-
$R_{A,0}$	Constant afferent resistance [mmHg.min/ml]	I	0.0293/W	Scaled from [139]
P_{ref}	Reference renal arterial pressure for myogenic mechanism [mmHg]	I	74	Scaled from [139]
G_{MM}	Myogenic Mechanism scaling coefficient [.]	I	0.0867	-
K_{TGF}	Coefficient of magnitude for TGF curve [.]	S	2.19 (1.47)	-
λ_{TGF}	Steepness of TGF curve [ml/mEq]	S	22.60 (16.98)	-
$\overline{R_{TGF}}$	Nominal TGF resistance [mmHg.min/ml]	I	0.0079/W	Scaled from [139]
$\overline{R_{Eff}}$	Nominal efferent resistance [mmHg.min/ml]	I	0.0802/W	Scaled from [139]
K_{Eff}	Coefficient of magnitude for efferent resistance curve [.]	S	0.27 (0.54)	-
$\overline{[ALD]}$	Nominal aldosterone concentration in plasma [ng/ml]	I	0.085	0.085 [127]
r_{P_0}	Nominal proximal tubule reabsorption fraction	S	0.66 (0.06)	0.65-0.8 [51], [127]
λ_N	Descending limb of Henle sensitivity [.]	S	1.32 (1.38)	-
λ_E	Early distal tubule sensitivity [.]	S	4.11 (5.5)	-
$\overline{[Na^+]}$	Nominal plasma sodium concentration [mEq/ml]	I	0.144	[85]
$r_{CW,max}$	Maximum water reabsorption fraction in collecting ducts [.]	I	0.995	-
$r_{CW,min}$	Minimum water reabsorption fraction in collecting ducts [.]	I	0.45	-
$\overline{r_{CW}}$	Nominal water reabsorption fraction in collecting ducts [.]	S	0.92 (0.02)	-
$\overline{[ADH]}$	Nominal ADH concentration [pg/ml]	I	1	1 [51]
$r_{CNa,max}$	Maximum water reabsorption fraction in collecting ducts [.]	I	1	-
$r_{CNa,min}$	Minimum water reabsorption fraction in collecting ducts [.]	I	0.2	-
n_{ALD}	Order of the aldosterone dose-response curve [.]	I	1	-
$\alpha_{UO,Na}$	Ratio of nominal urine sodium concentration to nominal PV sodium concentration	S	0.69 (0.36)	-
Re_0^+	Nominal renin release rate [GBU/hr]	I	0.48	0.48 [127]

Re_0	Nominal renin content in the circulation [GBU]	I	$[Re]_0 V_{PL,0}$	-
$[Re]_0$	Nominal renin concentration in plasma [GBU/ml]	I	0.00006	0.00006 [127]
τ_{ren}	Renin time constant [1/h]	S	0.36 (0.21)	0.05-0.6 [147]
$Ang\ II_0^+$	Nominal Ang II release rate [pg/hr]	I	105*60	105*60 [127]
C_{Ang}	Angiotensin release coefficient [.]	S	0.60 (1.41)	-
ALD_0^+	Nominal aldosterone secretion rate [ng/h]	I	3162	3162 [127]
w_{ALD}	Weight of the effect of $[Na^+]$ on aldosterone secretion [.]	S	0.76 (0.64)	-
$C_{ALD,Na}$	Coefficient of $[Na^+]$ sensitivity for aldosterone secretion [.]	S	28.14 (29.8)	-
K_{ALD}	Coefficient of angiotensin sensitivity for aldosterone secretion [.]	S	1.91 (1.95)	-

Table 5.6: Mathematical model parameters for human subjects: definitions, categories (I/S), and values. I: subject-invariant parameters. S: subject-specific parameters, SS: sensitive subject-specific. Parameter values are given as mean, median (IQR), or mean+/-SD.

Symbol	Definition	I/S	Value (Model)	Value (Literature)
$\bar{V}_P$	Nominal water volume in plasma [ml/kg]	I	42.8	42 [81]-46 [36]
r_{FV}	Skin fluid volume to total interstitial fluid volume ratio [·]	I	0.28	0.28 [36]
$\bar{V}_{BT}$	Nominal water volume in burnt tissue [ml/kg]	I	$120\varepsilon_B r_{FV}$	$120\varepsilon_B r_{FV}$ [36]
$\bar{V}_{IT}$	Nominal water volume in intact tissue [ml/kg]	I	$120(1-\varepsilon_B r_{FV})$	$120(1-\varepsilon_B r_{FV})$ [36]
$[\bar{A}_P]$	Nominal albumin concentration in plasma [g/ml]	I	0.045	0.035-0.045 [107]
$[\bar{A}_{BT}]$	Nominal albumin concentration in burnt tissue [g/ml]	I	0.018	0.013 [108]-0.016 [36]
$[\bar{A}_{IT}]$	Nominal albumin concentration in intact tissue [g/ml]	I	0.018	0.013 [108] -0.016 [36]
$\bar{A}_P$	Nominal albumin content in plasma [g]	I	$[\bar{A}_P]\bar{V}_P$	-
$\bar{A}_{BT}$	Nominal albumin content in burnt tissue [g]	I	$[\bar{A}_{BT}]\bar{V}_{BT}$	-
$\bar{A}_{IT}$	Nominal albumin content in intact tissue [g]	I	$[\bar{A}_{IT}]\bar{V}_{IT}$	-
$\bar{J}_C$	Nominal capillary filtration [ml/kg·h]	SS	1.88 (0.66)	1.72 [79]
C_O	Colloid oncotic pressure constant [mmHg/g·ml]	I	609	657 [36]
$\bar{J}_L$	Nominal total lymphatic flow to plasma [ml/kg·h]	I	1.76	1.07 [37]-2.9 [109]
$\bar{J}_{L,BT}$	Nominal lymphatic flow from burnt tissue to plasma [ml/kg·h]	I	$\bar{J}_L\varepsilon_B r_{FV}$	$\bar{J}_L\varepsilon_B r_{FV}$ [36]
$\bar{J}_{L,IT}$	Nominal lymphatic flow from intact tissue to plasma [ml/kg·h]	I	$\bar{J}_L(1-\varepsilon_B r_{FV})$	$\bar{J}_L(1-\varepsilon_B r_{FV})$ [36]
C_L	Lymphatic maximal increase coefficient [·]	S	0.07	-
S_L	Lymphatic pressure sensitivity coefficient [1/mmHg]	SS	1.33 (1.13)	-
$\bar{P}_C$	Nominal capillary hydrostatic pressure [mmHg]	S	16.3	13 [110]- 24 [8]
E_C	Capillary elastance [mmHg/ml]	S	0.0084	0.0097 [37]
α	Tissue electrostatic pressure coefficient [mmHg]	I	10	10 [45]
γ	Tissue tension pressure coefficient [mmHg]	I	3.75	3.75 [45]
$\hat{y}$	Maximum half-thickness of the extracellular matrix [·]	I	4	4 [45]
$\check{y}$	Minimum half-thickness of the extracellular matrix [·]	I	1	1 [45]
$\hat{R}$	Maximum GAG radius [·]	I	3.5	3.5 [45]
β	Radius threshold ratio [·]	I	0.23	0.23 [45]
n	Hydration response coefficient [·]	I	8	2-8 [45]
$\bar{W}_X$	Nominal hydration level [ml/g]	I	0.66	0.23-0.81 [45], [46]
$\bar{J}_{RPF}$	Nominal renal plasma flow [ml/kg·h]	I	536	536 [111]
τ_{TGF}	Tubuglomerular feedback time constant [1/h]	S	0.35	-
K_{TGF}	Tubuglomerular feedback sensitivity [·]	S	1.45	-
$\bar{R}_G$	Nominal glomerular resistance [mmHg/ml/kg·h]	I	9.05	-
λ_G	Glomerular hydrostatic pressure sensitivity [$mmHg^2/(ml/h\cdot kg)^2$]	I	1	-
P_B	Hydrostatic pressure in Bowman's capsules [mmHg]	I	18	18 [47]
K_G	Glomerular filtration coefficient [ml/kg·h·mmHg]	S	9.2	9.6-12.0 [84]
K_{ADH}	Nominal ADH secretion rate [pg/kg·h]	I	287	287 [54], [55]
λ_{V_P}	ADH sensitivity to plasma volume change [1/ml]	SS	6.56e-4 (0.001)	-
$\lambda_{[Na^+]}$	ADH sensitivity to sodium concentration change [l/mEq]	S	102.6 (153)	-

K_{RR}	Maximum collecting duct reabsorption fraction [·]	I	0.999	-
$\overline{[ADH]}$	Nominal ADH concentration [pg/ml]	I	1	0-5 [112]
$[ADH]_{50}$	ADH concentration corresponding to $\frac{1}{2}K_{RR}$ [pg/ml]	S	0.0594	-
$\overline{[Na^+]}$	Nominal plasma sodium concentration [mEq/l]	I	142	142 [85]
$\bar{J}_{RR,ADH}$	Nominal water reabsorption rate in the collecting ducts [·]	S	0.955	0.97 [51]
$\hat{Q}_{PD}$	Protein influx post burn [g/h]	S	85.8	-
λ_{PD}	Protein influx decay rate [1/h]	S	10	-
$M_{P_{BT}}$	Maximum burnt tissue hydrostatic pressure perturbation [mmHg]	S	56	20-270 [56]
$\lambda_{1,P_{BT}}$	Burnt tissue hydrostatic pressure perturbation slow decay rate [1/h]	S	6.88	-
μ	The ratio between slow decay rate to fast decay rate [·]	S	365	-
$\lambda_{2,P_{BT}}$	Burnt tissue hydrostatic pressure perturbation fast decay rate [1/h]	I	$8\lambda_{1,P_{BT}}$	-
$K_{1,EV}$	Nominal tissue evaporation rate [ml/h·m^2]	I	18.48	18.48 [63]
$\lambda_{1,EV}$	Evaporation growth rate [1/h]	I	0.073	0.073 [63]
$K_{2,EV}$	Maximum evaporation rate [ml/h·m^2]	I	28.68	28.68 [63]
$\lambda_{2,EV}$	Evaporation decay rate [1/h]	I	-0.0052	-0.0052 [63]
ε_B	Fraction of body surface subject to burn [·]	S	0.16-1	dataset
K_{EX}	Maximum exudation rate [ml/h·m^2]	I	25	25 [62]
λ_{EX}	Exudation decay rate [1/h]	I	-0.0038	-0.0038 [62]
η_{EX}	Exudate to tissue albumin ratio [·]	S	0.60	0.75 [36]
$\bar{\alpha}$	Nominal albumin to capillary pore radius ratio [·]	SS	0.86 (0.09)	0.7-0.9 [37]
$1-k_{PD,BT}$	Capillary destruction fraction for burnt tissue [·]	S	0.47	0.50 [35]
$1-k_{PD,IT}$	Capillary destruction fraction for intact tissue [·]	I	0	-
$M_{\alpha_{BT}}$	Maximum pore ratio perturbation in burnt tissue [·]	S	0.27	0.30 [39]
$M_{\alpha_{IT}}$	Maximum pore ratio perturbation in intact tissue [·]	SS	0.21 (0.08)	0.19 [87]
$\lambda_{1,\alpha}$	Pore ratio slow decay rate [1/h]	S	0.015	0.025 [36]
$\lambda_{2,\alpha}$	Pore ratio fast decay rate [1/h]	I	$\mu\lambda_{1,\alpha}$	-
M_{P_C}	Maximum capillary hydrostatic pressure perturbation [mmHg]	SS	18.62 (17)	23 (5) [61]
λ_{1,P_C}	Capillary hydrostatic pressure perturbation slow decay rate [1/h]	S	0.51 (0.33)	-
λ_{2,P_C}	Capillary hydrostatic pressure perturbation fast decay rate [1/h]	I	$\mu\lambda_{1,P_C}$	-
λ_{msp}	Mean systemic pressure sensitivity [1/ml]	SS	0.27 (0.37)	-
K_{TPR}	Total peripheral resistance coefficient [.]	SS	4.18 (8.07)	-
λ_{TPR}	Total peripheral resistance coefficient [ml/ng]	S	10.95	-
$\overline{[Ang\ II]}$	Nominal angiotensin II plasma concentration [ng/ml]	I	0.027	0.027 [127]
CO_{max}	Maximum cardiac output [mmHg]	S	2.86	-
$\overline{MAP}$	Nominal mean arterial pressure [mmHg]	S	82.25	90 [139]
$\overline{CO}$	Nominal cardiac output [lpm]	S	5.55	5-6 [158]
M_{MAP}	Maximum mean arterial pressure perturbation [mmHg]	S	1.42	-
$\lambda_{1MAP,}$	MAP slow decay rate [1/h]	S	0.56	-
$\lambda_{2,MAP,}$	MAP fast decay rate [1/h]	S	$\mu\lambda_{1MAP,}$	-
$\overline{CVP}$	Nominal central venous pressure [mmHg]	S	4.61	2-8 [159]
K_{RA}	Renal arterial pressure coefficient [.]	S	0.83	-
K_{RV}	Renal vein pressure coefficient [.]	S	0.81	-
$R_{A,0}$	Constant afferent resistance [mmHg.min/ml]	I	0.0293/W	Scaled from [139]
P_{ref}	Reference renal arterial pressure for myogenic mechanism [mmHg]	I	74	Scaled from [139]
G_{MM}	Myogenic Mechanism scaling coefficient [.]	I	0.0867	-
K_{TGF}	Coefficient of magnitude for TGF curve [.]	S	2.36	-
λ_{TGF}	Steepness of TGF curve [ml/mEq]	S	18.1	-
$\overline{R_{TGF}}$	Nominal TGF resistance [mmHg.min/ml]	I	0.0079/W	Scaled from [139]
$\overline{R_{Eff}}$	Nominal efferent resistance [mmHg.min/ml]	I	0.0802/W	Scaled from [139]
K_{Eff}	Coefficient of magnitude for efferent resistance curve [.]	SS	0.71 (1.28)	-
$\overline{[ALD]}$	Nominal aldosterone concentration in plasma [ng/ml]	I	0.085	0.085 [127]
r_{P_0}	Nominal proximal tubule reabsorption fraction	S	0.70	0.65-0.8 [51], [127]

λ_N	Descending limb of Henle sensitivity [.]	S	0.99	-
λ_E	Early distal tubule sensitivity [.]	S	6.05	-
$\overline{[Na^+]}$	Nominal plasma sodium concentration [mEq/ml]	I	0.144	[85]
$r_{CW,max}$	Maximum water reabsorption fraction in collecting ducts [.]	I	0.995	-
$r_{CW,min}$	Minimum water reabsorption fraction in collecting ducts [.]	I	0.45	-
$\overline{r_{CW}}$	Nominal water reabsorption fraction in collecting ducts [.]	S	0.95	-
$\overline{[ADH]}$	Nominal ADH concentration [pg/ml]	I	1	1 [51]
$r_{CNa,max}$	Maximum water reabsorption fraction in collecting ducts [.]	I	1	-
$r_{CNa,min}$	Minimum water reabsorption fraction in collecting ducts [.]	I	0.2	-
n_{ALD}	Order of the aldosterone dose-response curve [.]	I	1	-
$\alpha_{UO,Na}$	Ratio of nominal urine sodium concentration to nominal PV sodium concentration	S	0.54	-
Re_0^+	Nominal renin release rate [GBU/hr]	I	0.48	0.48 [127]
Re_0	Nominal renin content in the circulation [GBU]	I	$[Re]_0 V_{PL,0}$	-
$[Re]_0$	Nominal renin concentration in plasma [GBU/ml]	I	0.00006	0.00006 [127]
τ_{ren}	Renin time constant [1/h]	S	0.46	0.05-0.6 [147]
$Ang\ II_0^+$	Nominal Ang II release rate [pg/hr]	I	105*60	105*60 [127]
C_{Ang}	Angiotensin release coefficient [.]	SS	1.01 (2.10)	-
ALD_0^+	Nominal aldosterone secretion rate [ng/h]	I	3162	3162 [127]
w_{ALD}	Weight of the effect of $[Na^+]$ on aldosterone secretion [.]	S	0.53	-
$C_{ALD,Na}$	Coefficient of $[Na^+]$ sensitivity for aldosterone secretion [.]	S	36.25	-
K_{ALD}	Coefficient of angiotensin sensitivity for aldosterone secretion [.]	S	2.88	-

Chapter 6: In Search of Burn Resuscitation Biomarkers Hidden in the Arterial Blood Pressure Waveform

6.1 Introduction

Incorporating intravenous (IV) fluids in burn resuscitation has drastically improved mortality rates. However, as discussed in chapter 1, there is a lack of agreement on an optimal resuscitation protocol that avoids under and over-resuscitation. The current resuscitation protocols suggest hourly doses of the IV fluid and are usually initialized based on the patient's weight, total burned surface area (TBSA), and hours post-burn. More crucial than the formula chosen to initialize IV fluid rate is subsequent titration to the patient's physiological responses since even with similar demographic information and TBSAs, patients respond differently to burn and resuscitation.

Almost exclusively, IV fluid rate is manipulated to maintain the UO in a pre-specified range (e.g., 30-50 ml/hr or 0.5-1.0 ml/hr/kg in adults). A systematic review by Paratz et al. found that, despite the variability of approaches to burn resuscitation, 94% of burn centers continued to use UO as the primary index of the adequacy of resuscitation [116]. This concept has even been utilized as the basis for decision-support systems such as the Burn Navigator which protocolizes alterations in IV fluid rate and is currently used in approximately 15% of U.S. burn centers [18]. Early results indicated decreased mortality, ventilator days, and resuscitation-fluid volumes; and improved achievement of UO targets [17]. Still, this strategy relies on a single variable (i.e., UO), which may be a less-than-ideal target for resuscitation [117], [160], [161].

UO is a highly complex variable to predict and interpret because it is affected by many things. It regulates not only PV but also blood pressure and electrolyte balance, to name a few, and is even affected by intense fear and pain.

Besides the inherent complexity of UO as a surrogate for fluid perfusion, sometimes patients have conditions that affect their UO in a certain way, such as pre-existing renal diseases [162], or burn shock-induced renal failure [163], which make UO a faulty representative of their volume kinetics. Even temporary conditions such as alcohol consumption would compromise the use of UO for assessing the patient status in the early hours post-burn, which are of significant importance [164].

Other informative parameters that could guide resuscitation are not as protocolized and widely adopted as UO, which may also suggest their inadequacy. Serum lactate level which measures the concentration of lactic acid in serum has been recommended in trauma patients [165], as it increases when the blood flow to organs has been limited, or in shock. However, it may not be accurate during organ dysfunction or ethanol intoxication [118], [166], and while it may correlate with outcome in general, there is scant evidence to utilize it for titration of IV fluid rate. Moreover, markers such as serum lactate cannot be read in a real-time or continuous fashion and require blood drawing. Common arterial blood pressure (ABP) measures, while significantly important to monitor for every patient, and valuable to guide resuscitation for hemorrhagic shock, are not as relevant and sensitive in burn shock given the massive fluid shifts and subsequent edema in burn patients [156], especially without an arterial line [116], [118], [167], [168]. More specific than the crude measurement of ABP, indicators of volume status such as cardiac output (CO) and stroke volume (SV), wedge

pressures, and oxygen delivery and consumption have been suggested as valuable endpoints for resuscitation. However, pulmonary arterial catheters that initially provided this information are not as commonly used due to concerns such as infections and arrhythmias.

Less invasive systems have been developed to combat this challenge, such as the PiCCO and LiDCO systems, which use thermodilution and lithium, respectively, to provide CO estimates [169], [170]. These systems can also allow sophisticated arterial pulse wave analysis (PWA) to generate functional hemodynamic measurements. Recently emerging success in the application of advanced hemodynamic monitoring (including PWA) to burn injury patients have triggered an ever-increasing interest in its integration into burn resuscitation [137], [160], [171], [172]. PWA can generate several CO and SV estimates as well as indices of fluid responsiveness, such as pulse pressure variation (PPV), systolic pressure variation (SPV), and stroke volume variation (SVV) in real-time. While it is evident why reliable and non-invasive estimates of CO and SV would be significantly valuable, we need some background to understand why the dynamic indices, i.e., PPV, SPV, and SVV, are relevant. Briefly, inspiration and expiration cause rhythmic oscillations in the intrathoracic pressure, slightly affecting the afterload and preload. This will cause cyclical variations in the ABP that will intensify when the heart is more responsive. The dynamic indices quantify the variations in the ABP in every respiratory cycle. Therefore, the more responsive the heart, the higher the dynamic index. We also know from the Frank-Starling curve of SV-preload that the subject is more fluid-responsive- i.e., an increase in preload volume will be translated into an increase in SV and CO- when the preload

and SV are smaller. Thus, while the dynamic indices do not directly represent SV and CO, they will be exaggerated in hypovolemic states and lowered in hypervolemia [173], thereby negatively correlate with them. Fig. 6.1 summarizes these concepts on the Frank-Starling curve. At point A, the SV is very responsive to variations in preload caused by mechanical ventilation. This is reflected by exaggerated cyclical oscillations in ABP, indicating both fluid responsiveness and the possibility of hypovolemia. At point B, the same increase in preload has minimal to no effect in SV, which is captured by minimal variations in ABP, indicating both non-responsiveness and the possibility of hypervolemia.

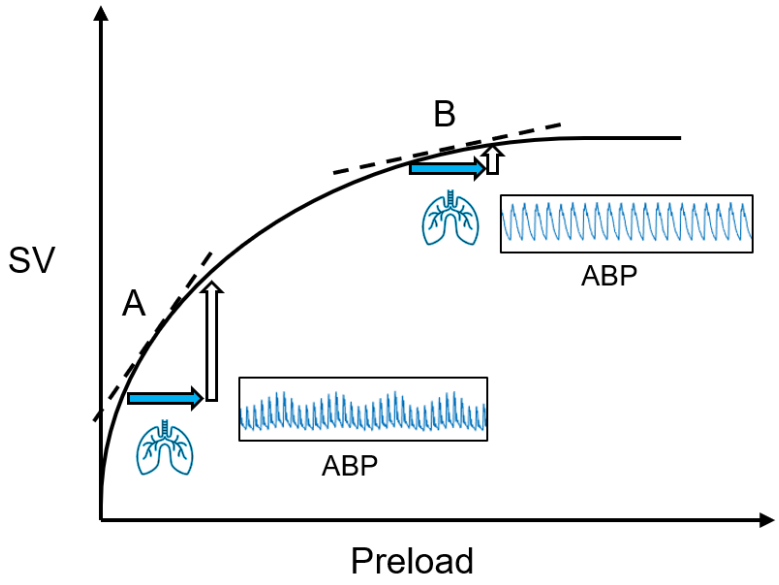

Fig. 6.1: The Frank-Starling curve. SV: stroke volume, ABP: arterial blood pressure waveform, blue arrow: change in preload in response to respiration, white arrow: change in SV in response to the change in preload. Point A: hypovolemia, exaggerated ABP waveform variation in response to respiration . Point B: hypervolemia, SV is preload-independent (non-responsive), reflected in ABP waveform not oscillating.

The dynamic indices have shown promise in hemorrhage resuscitation as well as peri- and post-operative fluid management [174]–[176]. However, none of these readouts have been extensively validated in the burn clinic, potentially due to patient heterogeneity. For instance, according to an international survey, PPV is among the top five most widely used parameters to guide resuscitation; nonetheless, no standard algorithm is suggested for using PPV in the context of burn injury [137]. Moreover, there is limited knowledge of these hemodynamic variables in burn resuscitation extremes. Thus, this chapter, which is an extension of our previously published paper [157], aims to test the hypothesis that PWA-derived dynamic indices PPV, SPV, and SVV, can play a complementary role to UO in determining the adequacy of burn resuscitation in various conditions.

6.2 Method

6.2.1 Experimental Procedure

Anesthesia and instrumentation

Female Yorkshire swine (n=21) were acclimated to the facility for 5 days prior to experimental use. Animals were fasted but allowed water ad-libitum 12 hours prior to the study. On the day of the experiment, animals were sedated using ketamine 15-30 mg/kg and xylazine 1-4 mg/kg IM, and a peripheral IV line was established in the lateral ear vein. Animals were endotracheally intubated and ventilated with 1-3 l/min of oxygen, 7-15 ml/kg tidal volume, and 10-20 bpm, to maintain end-tidal CO2 of 40±5 mmHg. General anesthesia was maintained using a combination of propofol (200

mcg/min/kg IV), ketamine (10-30 mg/hr/kg IV), vecuronium (0.15-1 mg/hr/kg IV), and fentanyl (3-4 µg/hr/kg IV). Electrocardiogram (ECG) signal was obtained at either 100 or 300 Hz by placement of ECG pads (Medtronic, Minneapolis, MN), which was monitored throughout the course of the experiment.

A Foley catheter was inserted trans-urethrally. Using ultrasound guidance, the left carotid artery was identified, and an introducer needle was inserted, followed by guidewire placement for insertion of a multi-lumen central venous catheter for monitoring of ABP. A femoral artery catheter was placed in a similar fashion for hemorrhaging and blood drawing. For pulmonary artery catheter placement, the right internal jugular vein was catheterized percutaneously, and a Swan-Ganz catheter was advanced while visualizing appropriate waveforms through the right atrium (at which point the balloon was inflated), right ventricle, and pulmonary artery. Proper placement was also confirmed with the aid of an angiogram. CO measurements were taken every 3-6 hours via standard thermo-dilution using the Swan Ganz catheter, while central venous pressure (CVP) and ABP waveform data were continuously collected throughout the course of the experiment.

Injury and Resuscitation

Through the femoral line, a controlled hemorrhage of 15% blood volume was performed to counteract the contractile properties of the porcine spleen. Animals were then subjected to a 40% TBSA burn with brass billets heated to 150˚C kept in contact with the skin for 10 sec producing a full-thickness burn. Burns were dressed with 1% silver sulfadiazine cream and covered with a dressing shirt. Animals were then randomized to receive IV Lactated Ringer's solution in the following amounts: (i)

Paradigm 1 (P1): no IV fluids to extremely dehydrate the subjects, (ii) Paradigm 2 (P2) IV fluid rate guided by UO according to the Burn Navigator to maintain adequate resuscitation, or (iii) Paradigm 3 (P3), a high rate 500 ml/hr or higher throughout the protocol to deliberately over-resuscitate. Animals were monitored for 24 hours post-injury, with their vitals recorded every 15 minutes, and blood samples collected at hours 1, 2, 3, 6, 9, 12, 18, and 24.

6.2.2 Computation of PWA Indices

First, we gated individual cardiac beats using the ECG signal (Fig. 6.2 (a)). For this purpose, we detected the R waves in the ECG signal using the "findpeaks" command in MATLAB and defined individual cardiac beats as the interval between neighboring R waves.

Second, we extracted fiducial points from the ABP signal on a beat-by-beat basis (Fig. 6.2 (b)). For each cardiac beat, systolic (SP) and diastolic (DP) blood pressures were identified as the maximum and minimum values in the ABP signal within the beat, and heart period was computed as the length of the beat in seconds. Mean arterial blood pressure (MAP) was computed as the area under the ABP signal within the beat (approximately via numerical integration) divided by the corresponding heart period. Once SP, DP, and heart period were obtained from all the cardiac beats, we detected and removed artifact-corrupted SP, DP, and heart period samples based on a binary abnormality score computed using the jSQI algorithm [177]. In brief, the jSQI derives the abnormality score based on a set of pre-specified, empiric constraints imposed on the ABP signal, including the amplitudes, slopes, and beat-to-beat variations associated

with SP, DP, MAP, and heart period. The artifact-corrupted samples predominantly occurred in the animals belonging to Paradigm 1, which may be attributed to the high risk of blood clotting in the catheter placed in these animals due to the high hematocrit values in the absence of IV fluids.

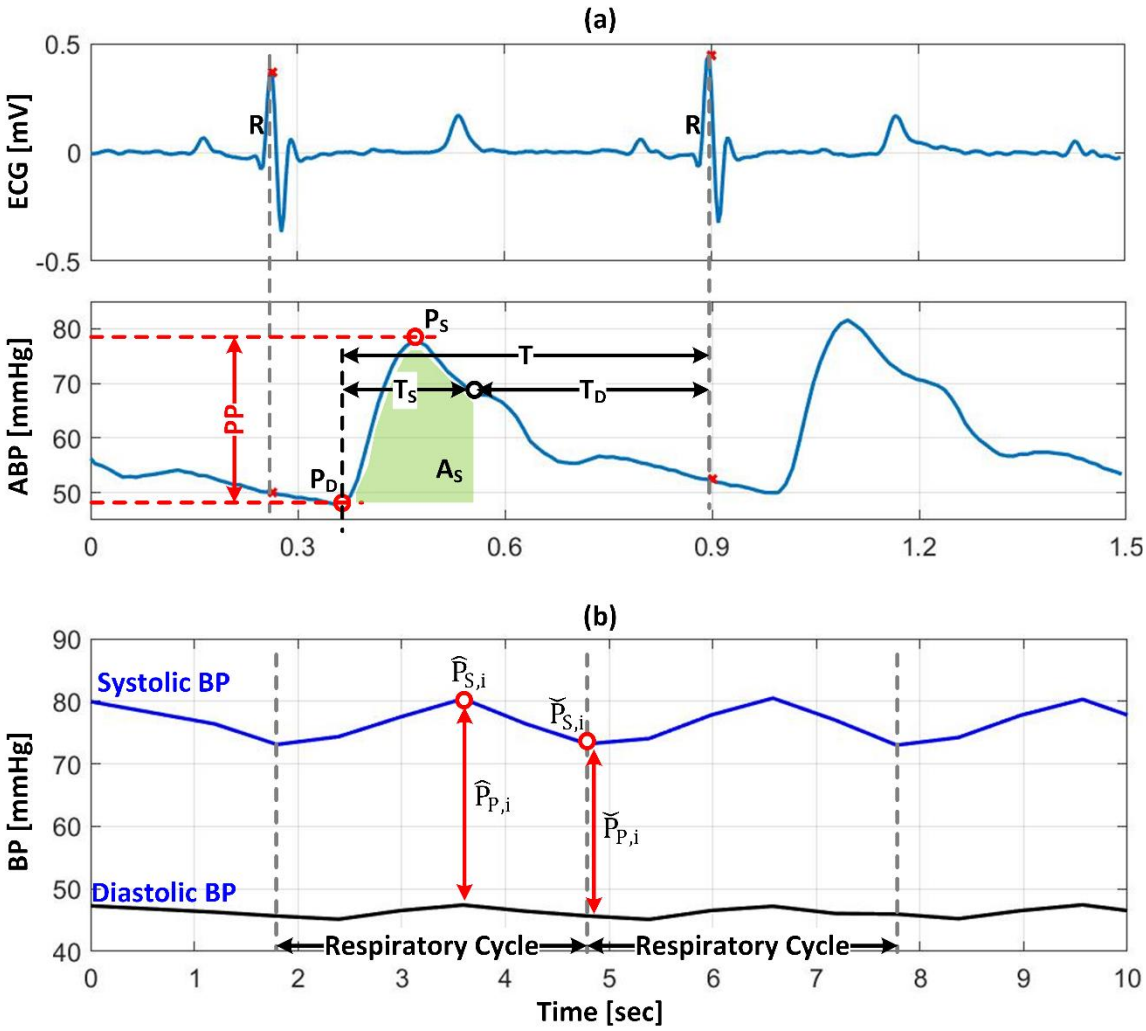

Fig. 6.2, Gating of cardiac beats and extraction of fiducial points for computing PWA-derived indices. (a) Fiducial points for computing PWA-derived CO indices. (b) Fiducial points for computing PPV and SPV. P_S: systolic blood pressure. P_D: diastolic blood pressure. T: heart period. T_S: ejection duration. T_D: diastolic duration. A_S: systolic blood pressure area.

Third, we computed PWA-derived indices, including CO and SV estimates, PPV, SPV, and SVV. Previously we had compared 10 different surrogates for CO and SV and chosen the one that best tracked CO and SV in terms of strongest correlation and least root-mean-squared error (RMSE) [157]. Here, we computed the SV indices on a beat-by-beat basis for all the subjects to enable calculation of SVV:

$$SV_{est} = \frac{\bar{P} - P_D}{60}, \tag{6.1}$$

Where SV_{est} is the best surrogate for SV, $\bar{P}$ is the MAP, and P_D the diastolic pressure. We then computed PPV, SPV, and SVV based on the established formulas for every respiratory cycle [178]:

$$PPV_i = 100 \times \frac{\hat{P}_{P,i} - \check{P}_{P,i}}{0.5 \times (\hat{P}_{P,i} + \check{P}_{P,i})}, \tag{6.2}$$

$$SPV_i = 100 \times \frac{\hat{P}_{S,i} - \check{P}_{S,i}}{0.5 \times (\hat{P}_{S,i} + \check{P}_{S,i})}, \tag{6.3}$$

$$SVV_i = 100 \times \frac{\widehat{SV}_{est,i} - \widecheck{SV}_{est,i}}{0.5 \times (\widehat{SV}_{est,i} + \widecheck{SV}_{est,i})}, \tag{6.4}$$

Where i is the respiratory period index, $\hat{P}_{P,i}$ and $\check{P}_{P,i}$ are the maximum and minimum PP, and $\hat{P}_{S,i}$ and $\check{P}_{S,i}$ the maximum and minimum SP, and $\widehat{SV}_{est,i}$ and $\widecheck{SV}_{est,i}$ the maximum and minimum surrogate for SV in the *i*-th respiratory period. In the absence of airway pressure signal recordings, we exploited the rhythmic oscillations in the time series sequences of PP to (i) estimate respiratory period, (ii) detect maximum and minimum PP, SP, SV_{est} and in each respiratory period, and (iii) compute PPV, SPV, and SVV associated with the respiratory period using Eq. (6.2-4). We extensively validated the integrity of the estimated respiratory period (which is crucial in computing accurate dynamic indices) using visual inspection and comparison with the respiratory rate settings in the mechanical ventilator.

6.2.3 Data Analysis

To facilitate data analysis, we summarized UO and PWA-derived indices into hourly-averaged values. During each hour post-burn in each animal, we defined outliers associated with UO and PWA-derived indices as the samples in the respective time series sequences residing outside of 10th-90th percentile range, removed them, and computed the mean and standard deviation of the remaining samples as the representative hourly values. Using these hourly average values of UO and PWA-derived indices, we performed analysis to garner the following insights: (i) the behaviors of UO and PWA-derived indices in response to a wide range of burn resuscitation paradigms; (ii) their ability to track the changes in CO and SV in a subject and in general; (iii) their similarity and discrepancy in classifying burn resuscitation adequacy; and (iv) their inter-individual variability.

First, we investigated the group-aggregated behaviors of CO, SV, UO, and PWA-derived indices in response to diverse burn resuscitation paradigms designed to encompass under-resuscitated, adequately resuscitated, and over-resuscitated regimes. Of particular interest was to elucidate the behaviors of our derived features in burn resuscitation as well as to compare them with UO, CO, and SV measurements. For each burn resuscitation paradigm, we aggregated the hourly average values of UO, CO, SV, PPV, SPV, and SVV across all the animals in the paradigm in terms of mean and standard error. Then, we investigated the time-dependent changes in the group-aggregated indices as burn resuscitation progresses in order to assess their utility as indicators of burn resuscitation adequacy and fluid responsiveness in burn injury.

Second, we investigated the ability of UO and PWA-derived indices to track the changes in CO and SV for every subject. For this purpose, we calibrated UO and PWA-derived indices to reference CO and SV on an animal-by-animal basis via linear regression and compared their effectiveness in tracking reference CO and SV using the root-mean-squared error (RMSE) and correlation coefficient (r) between reference CO and SV, and the calibrated UO and PWA-derived indices.

Third, we compared UO and PWA-derived indices in determining burn resuscitation adequacy. For this purpose, we specified normal ranges of UO, and PWA-derived indices based on our in-house in-vivo data and data available in the literature. We determined the normal ranges of CO and SV based on the data pertaining to this work: using the available initial pre-injury recordings in all the animals, we specified normal CO range of 63-88 ml/min/kg and normal SV range of 0.65-1.15 ml/kg/beat. We determined the normal ranges of PPV and SPV based on the existing literature as well as their distributions for different paradigms. For PPV, literature suggests that normal values can be as low as 10% [179] and as high as 20% [178], [180]. Within this bound, we chose 13%-17% as the normal PPV range, which were used as cutoff values for fluid-responsiveness in prior works [161], [181], and more generally because the 10-20% range was not as sensitive and encompassed too many datapoints. While less literature exists on SPV, we specified normal SPV range of 5%-8%, which is congruent with the 5-10 mmHg range reported in the literature [182], [183] after normalizing with typical SP values. For SVV, different numbers have been reported as normal fluid-responsiveness. We chose the range of 18-28% from our baseline recordings, which also encompasses the baseline SVV values in an experimental study before [180]. The

normal range for UO for porcine models is assumed to be 1-1.5 ml/kg/hr, which is the end-point used to resuscitate subjects in paradigm 2.

Using these normal ranges, we classified the hourly UO as well as PWA-derived samples associated with all the animals into (i) under-resuscitation (UR); (ii) adequate resuscitation (AR); and (iii) over-resuscitation (OR). In this way, each post-burn hour was assigned four adequacy labels determined by UO, PPV, SPV, and SVV. Subsequently, we performed the cross-tabulation analysis between UO versus, PPV, SPV, and SVV and investigated the equivalence or discrepancy in the classification of resuscitation adequacy among these indicators, using Chi-square tests.

Fourth, we investigated the group-aggregated patterns in the relationship between reference CO and SV versus UO and PWA-derived indices. Of particular interest was the consistency and robustness of the physiologically anticipated relationships between reference CO and SV versus UO and PWA-derived indices. For this purpose, we performed group-aggregated regression analysis and assessed the signs of the slopes in the resulting regression equations as well as the degree of correlations and data scatters in comparison to those obtained at the individual animal level.

6.3 Results

Fig. 6.3 shows the group-average time courses of CO, SV, UO, PPV, SPV, and SVV in each of the three resuscitation paradigms. The CO and SV trends show a decline immediately post-burn for all three paradigms due to the volume shift from the intravascular compartment to tissues, which is the signature of burn injury. For P1, CO and SV mostly stay below the normal range after that, while P2 subjects reside within

the normal range, and P3 above the normal range. As can be seen from the plot, CO trends for P2 and P3 have a lot of overlap, and a Wilcoxon signed-rank test confirms that the CO does not distinguish P2 and P3 before averaging the results. After taking the average, however, it can differentiate between the two paradigms. All the other variables on the plot distinguish between the three paradigms before and after taking the average ($p<0.01$).

All the PWA-derived indices exhibited physiologically reasonable group-aggregated behaviors in each paradigm: PPV, SPV, and SVV increased in Paradigm 1 (indicating that the animals became increasingly fluid responsive toward the end of the 24 hours post-burn), fluctuated around normal values in Paradigm 2, and substantially decreased for Paradigm 3; indicating that the animals became less fluid responsive toward the end of the 24 hours post-burn).

UO exhibited an increasing degree of inter-individual variability toward the end of the 24 hours post-burn, which made it less attractive as a metric of burn resuscitation adequacy in some animals, especially in that UO values were within or above the normal range for the subjects in P1 which did not receive any fluid, and the was high above the normal range for P2, which was adequately resuscitated.

Table 6.1 summarizes the performance of UO and the dynamic indices in tracking reference CO and/or SV, while Fig. 6.4 visualizes the correlation between reference CO and SV versus UO, PPV, SPV, and SVV, all calibrated to the reference CO and SV.

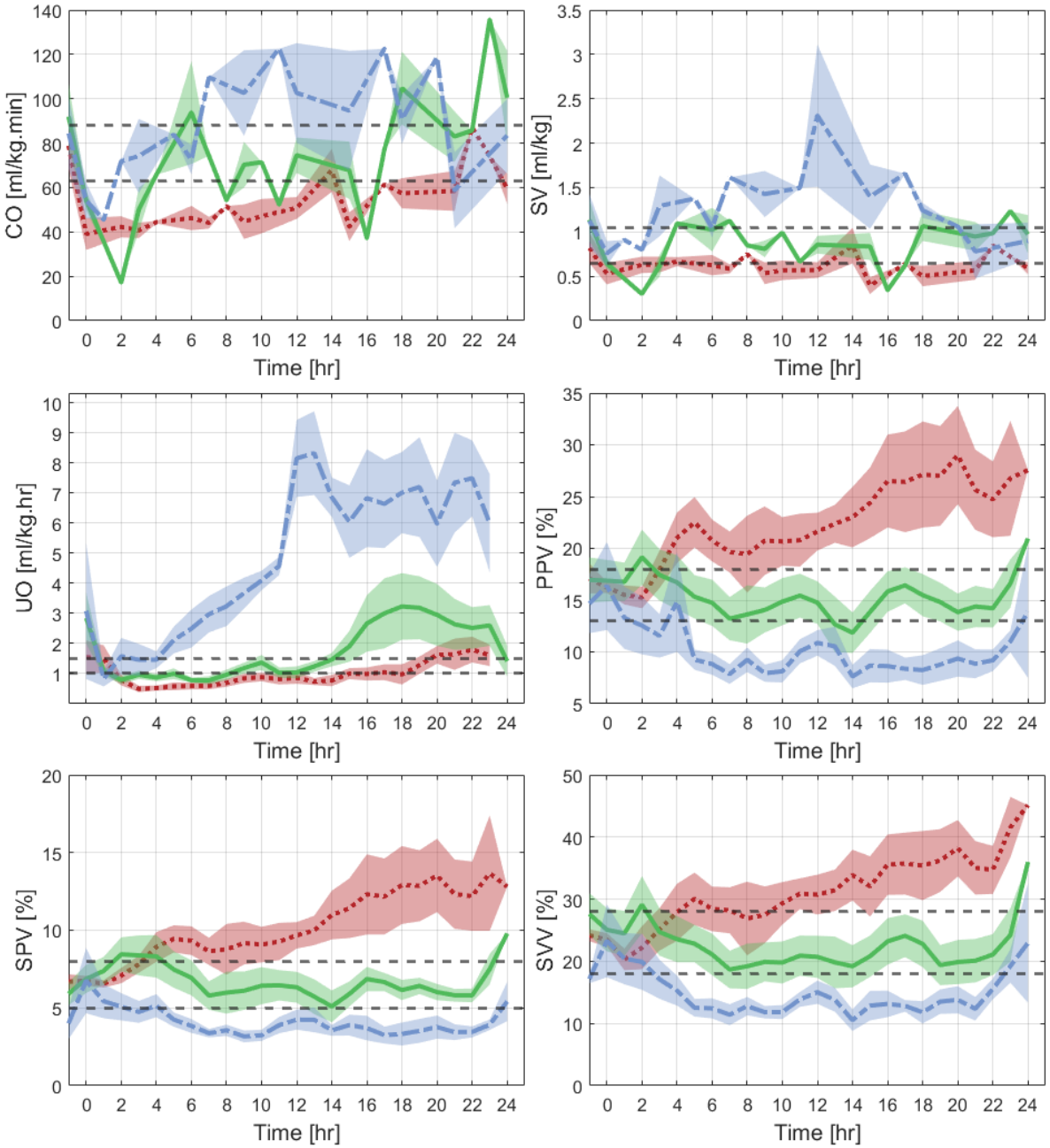

Fig. 6.3, group-averaged time courses of CO, SV, UO, PPV, SPV, and SVV for the three paradigms. P1: paradigm 1, no resuscitation, red dotted-line (mean) and red shaded area (standard error), P2: paradigm 2, adequately-resuscitated, solid green line and green shaded area, P3: paradigm 3, over-resuscitated, blue dash-dot line, and blue shaded area.

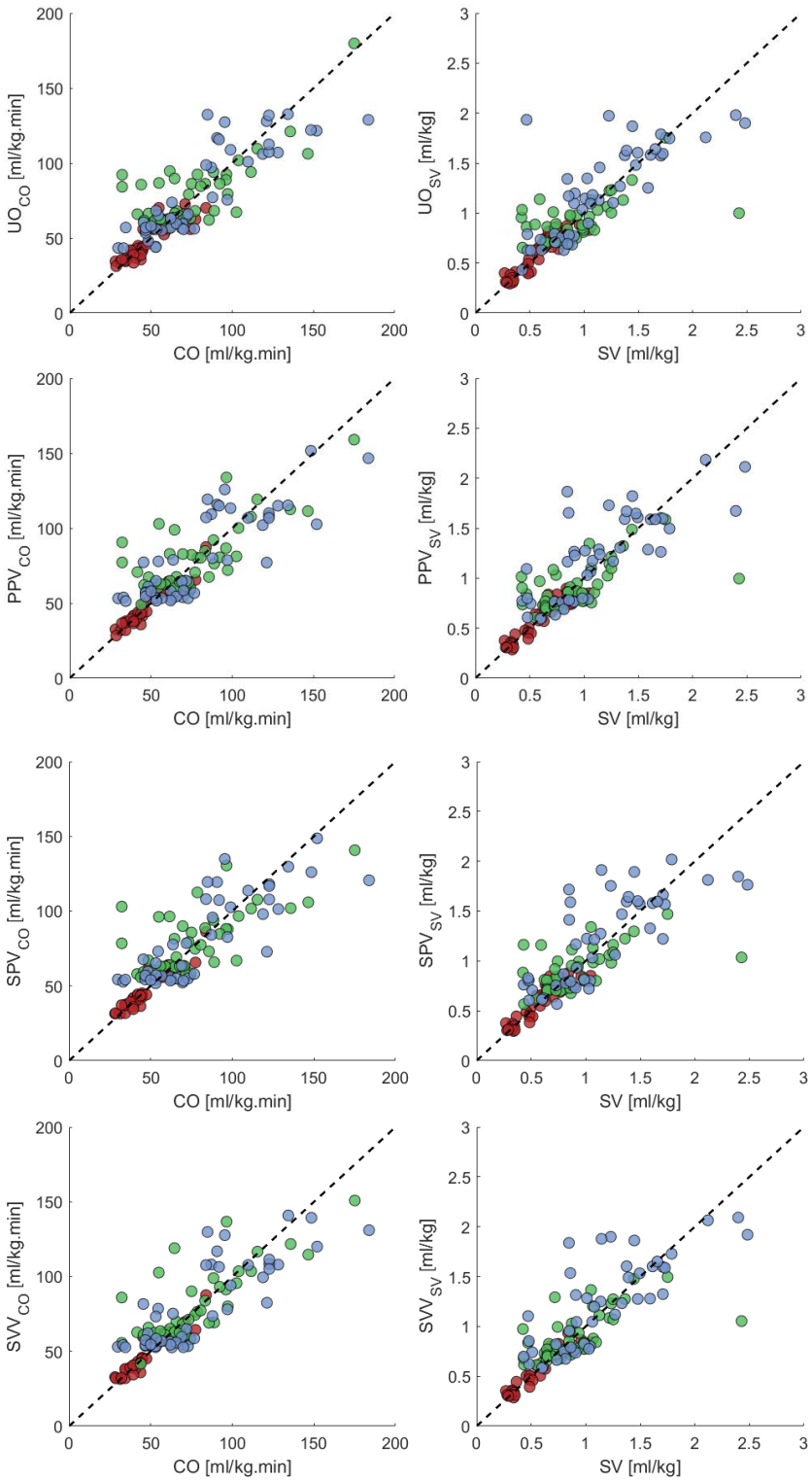

Figure 6.4: Scatter-plots for UO, PPV, SPV, and SVV after being calibrated to CO (left column) and SV (right column) for the three paradigms. Red circles: P1 data points, green circles: P2 data points, blue circles: P3 datapoints

Table 6.1: Post-calibration correlation coefficient (r) and root-mean-squared error (RMSE, median(iqr)) between reference CO versus UO, PPV, SPV, and SVV.

	UO	PPV	SPV	SVV
r_{CO}	0.80	0.80	0.78	0.81
$\mathrm{RMSE_{CO}}$ [ml/kg/min]	10.98 (11.05)	10.58 (15.21)	11.36 (16.97)	11.48 (15.52)
$\mathrm{r_{SV}}$	0.73	0.73	0.73	0.75
$\mathrm{RMSE_{SV}}$ [ml/kg]	0.13 (0.11)	0.13 (0.14)	0.12 (0.17)	0.13 (0.14)

The average RMSEs associated with UO, PPV, SPV, and SVV were similar and had no statistically significant difference, suggesting that PWA-derived indices may complement UO in tracking the time-dependent trends of CO and SV, since they have similar tracking performance but can be calculated in real-time, in contrast to the UO. It is also noted that tracking the absolute values of CO and SV may require subject-by-subject calibration of these surrogate metrics to their respective reference values. In fact, non-trivial degradation in the degree of correlation was observed when the data from all the animals were pulled without subject-specific calibration (see Fig. 6.6 and the related discussions).

Fig. 6.5 shows the results of preliminary classification and contingency analysis. The first row of Fig. 6.5 shows the cross-tabulation between UO vs PWA-derived indices. While the Chi-squared test confirmed that the classifications are not independent ($p<0.01$) and they have more than 50% agreement in the case of over-resuscitation, it is evident that there is a lot of discrepancy between the UO vs dynamic indices in determining adequate- and under- resuscitation status. Between UO and PPV, there is only 25.5% (23/90) agreement among the samples classified as adequate resuscitation (AR), while they have a 62% (110/176) agreement on over-resuscitation (OR), and

47% (78/167) on under-resuscitation (UR). Between UO and SPV, among the samples classified as adequate resuscitation by UO, 41% (37/90) were also classified as such by SPV, while among the samples classified as adequate resuscitation by SPV, only 26% (37/141) were classified as such by UO. For the UR group, 41% (70/167) of the samples classified by SPV are also classified as UR by UO, while this number is 49% (70/142) for the UO.

Between UO and SVV, among the samples classified as AR by UO, 34% (31/90) are also classified as such by SVV, while among the samples classified as AR by SPV, only 22% (31/143) were classified as AR by UO. There's also a large discrepancy in the UR group, where only 30% (51/167) of samples classified as UR by UO were confirmed by SVV.

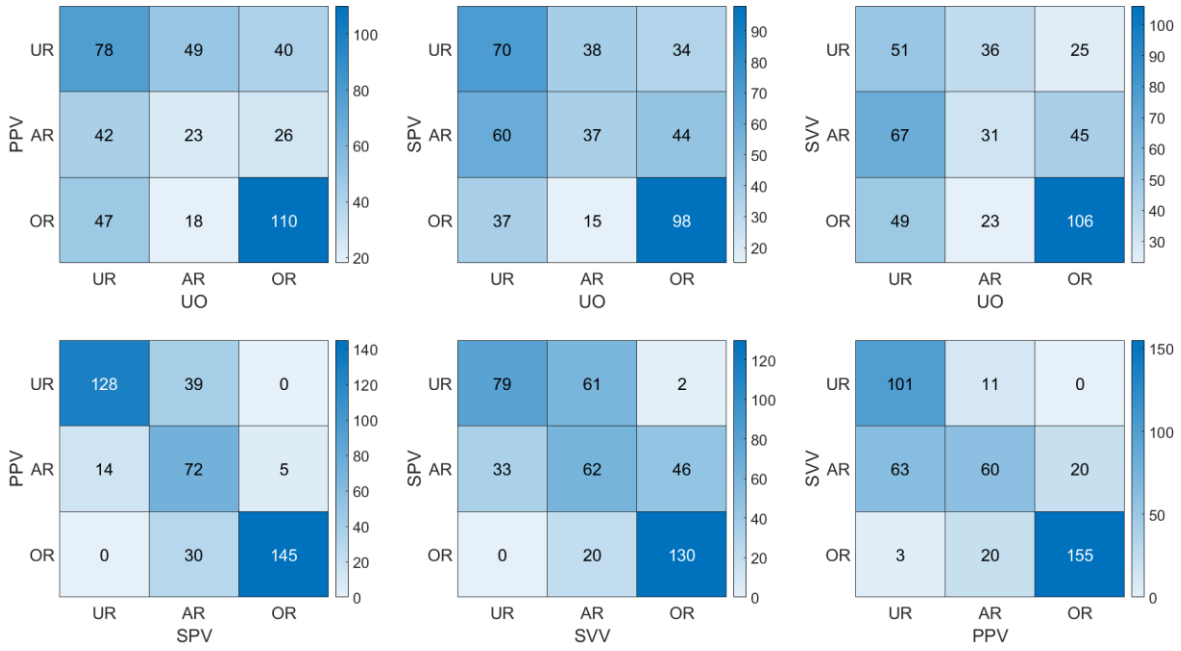

Figure 6.5: Cross-tabulation between the features. UR: under-resuscitated, AR: adequately resuscitated, OR: over-resuscitated.

The second row of Fig. 6.5 compares the classifications for the dynamic indices against each other. This analysis aims to see if any of the features are redundant. While the level of agreement is more significant than cross-tabulation with UO, especially in the resuscitation extremes, we can see that there is still a notable degree of disagreement in the AR classification. One significant difference between the indices is the general distribution of samples in the three groups. PPV, similar to UO, classifies only 21% of the samples as AR, while this number is 32% and 33% for SPV and SVV, respectively. That is why only 51% (72/141) of the samples identified as AR by SPV agree with PPV, while this number is equal to 79% (72/90) for PPV due to its small number of AR-classified samples.

Similarly, For SVV, 42% (60/143) of the samples classified as AR agree with PPV, while this number is 67% (60/90) for PPV. SPV and SVV have a 43% agreement on the classification of AR from both ends since they have the same number of samples in the AR group.

Although these numbers are very susceptible to variations in normal threshold defined for each variable, experimenting with various feasible thresholds showed that the disagreement, especially in classifying the AR group, still holds. Another caveat is that defining a group-averaged threshold may not be the best course of action since there is a large inter-subject variability, as shown in Fig. 6.6 and elaborated on in the discussion section.

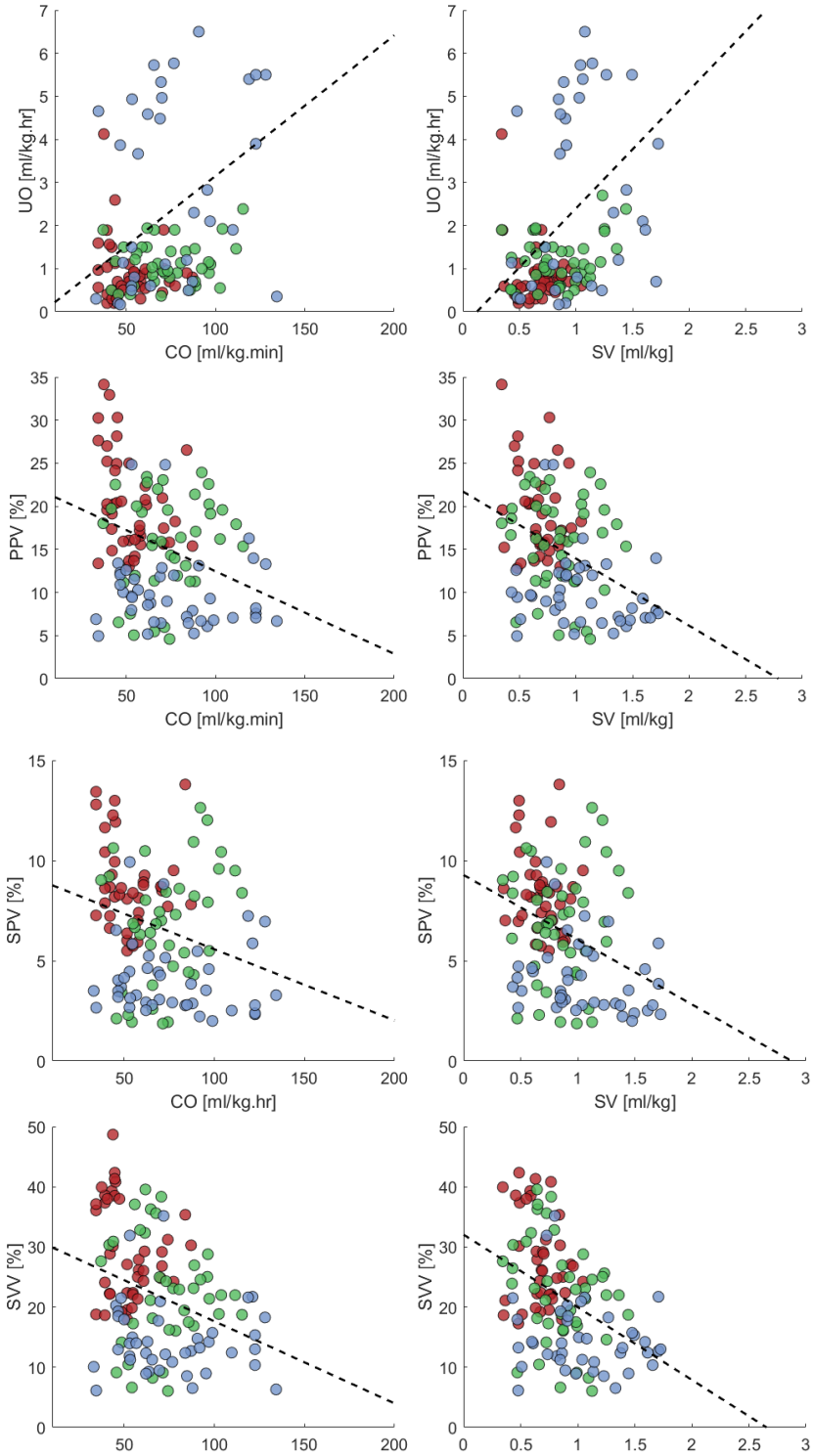

Figure 6.6: scatter-plots of raw (uncalibrated) UO, PPV, SPV, and SVV against CO (left column) and SV (right column) for the three paradigms. Red circles: P1 data points, green circles: P2 data points, blue circles: P3 datapoints

Fig. 6.6 shows the pre-calibration relationship between reference CO or SV versus UO, PPV, SPV, and SVV. In contrast to Fig. 6.4 (in which the same relationship was presented after the features were calibrated to reference CO and SV in each animal), a non-trivial degree of inter-individual variability in the relationship was observed. For example, normal UO range of 1.0-1.5 ml/hr/kg corresponded to a wide range of CO: 39-111 l/min/kg. Likewise, normal PPV range of 13%-17% corresponded to a wide range of SV: 0.36-1.7 ml/kg. The variability originated from the animal-to-animal differences in nominal CO and SV values as well as in the degree of changes in the surrogate metrics in response to a given change in CO and SV. The results suggest the benefit of tailoring the surrogate metrics on a subject-by-subject basis.

6.4 Discussion

UO, a widely used endpoint for titrating burn resuscitation, is known to be a deficient measure of CO and tissue perfusion. Hence, complementing UO with additional physiological indicators to optimize burn resuscitation may improve outcomes. Recent success in incorporating advanced hemodynamic monitoring based on PWA into burn resuscitation has shown promise. However, the potential of PWA-derived indices in burn resuscitation, especially compared to UO, is largely unknown. In addition, the validity of various PWA-derived indices in burn injury patients is yet to be established. To investigate the complementary value of PWA-derived indices in burn resuscitation, we hypothesized that PWA-derived indices (PPV, SPV, and SVV) can provide additional insight relevant to burn resuscitation adequacy beyond UO. We

demonstrated that PPV, SPV, and SVV (i) faithfully track the changes in thermodilutionally-derived CO and SV in individual subjects; (ii) exhibit physiologically anticipated behaviors against diverse burn resuscitation paradigms; and (iii) provides distinct assessment of burn resuscitation adequacy compared with UO.

Since examining resuscitation extremes (i.e., targeting over- resuscitation or fluid withholding) is not ethical in humans, animal models provide an opportunity to study these extremes. Compared with resuscitation strategies typically employed in rodents (i.e., subcutaneous single bolus injections), swine allows for titration of fluid rate in a clinically relevant ICU setting. Swine also have a cutaneous structure and healing mechanism that more approximate the clinical situation [184]–[186]. In this regard, we were able to follow a clinically relevant protocol of burn resuscitation (i.e., adherence to the Burn Navigator) as well as prescribe resuscitation extremes.

The time-dependent behaviors of the PWA-derived indices in response to three different resuscitation paradigms strongly suggested their potential utility as the basis for classifying burn resuscitation adequacy (Fig. 6.3). In the case of Paradigm 1, UO as well as CO and SV resided below their respective normal ranges. Consistently, PPV, SPV, and SVV resided above their respective normal ranges, but with relatively large inter-animal variability despite a lack of fluid resuscitation. In the case of Paradigm 2, CO, SV and all the PWA-derived indices remained in the vicinity of their respective normal ranges. However, UO exhibited a huge variability after 15 hours post-burn, and mostly resided above the normal range. Additionally, it appears that UO increased to normal values at least four hours after PWA-derived indices, potentially suggesting a superior sensitivity of PWA-derived indices that could identify adequate resuscitation

earlier and prevent fluid creep. In fact, delayed UO response to burn resuscitation has been observed in prior studies [6]. In the case of Paradigm 3, CO, SV, and UO measurements showed sizeable inter-subject variability. In general, CO and SV show a decline after the burn injury, increase as the subject is over-resuscitated, peak around 8-16 hours post-burn, and eventually marginally recover due to the body's self-regulating mechanisms. The UO is above the normal range after hour four, and while it's decreasing after hour 12, the recovery is minimal, and UO is still very large. The PWA-derived dynamic indices remained below their normal ranges for much of the experiment for P3 but ended up within or close to normal ranges at the end, which is a testament to their relevance to fluid responsiveness, as opposed to UO.

In sum, UO and PWA-derived indices generally responded plausibly to burn resuscitation, reflecting their potential utility in tracking fluid responsiveness and resuscitation adequacy. However, their predictions were not always consistent and often exhibited non-trivial degrees of discrepancy.

With subject-specific calibration, PWA-derived indices agreed with reference CO and/or SV reasonably well (Fig. 6.4). The slope of the calibration equation indicated that PPV, SPV, and SVV are inversely proportional relationship to reference CO and SV. This is physiologically plausible, since the dynamic indices are indicators of fluid responsiveness (which is expected to decrease as CO and SV increase). In terms of both RMSE and r, the dynamic features and UO performed similarly. Admittedly, exact tracking of the absolute values of CO and SV as shown in Fig. 6.4 necessitates subject-specific calibration (which is not always practical). However, our results suggest that PWA-derived indices may be useful as qualitative indicators of time-

dependent changes in CO and SV, with the advantage of being calculated in real-time as opposed to UO.

According to the cross-tabulation analysis, the classification of burn resuscitation adequacy was not significantly different between UO and PWA-derived dynamic indices ($p<0.001$, Chi-square test; Fig. 6.5). In particular, UO and PWA-derived indices exhibited relatively higher agreement in classifying over-resuscitation, as indicated by the large numbers in the lower right corners in all the contingency matrices. However, there was notable discrepancy in determining adequate resuscitation (note that burn resuscitation is regarded as adequate if the treatment endpoint of choice resides in its normal range), and to a lesser extent, in determining under-resuscitation. All in all, UO and PWA-derived indices appear to be more consistent in determining extreme (severe) under- and over-resuscitation status. However, their decisions deviate in classifying the grey zone, i.e., adequate resuscitation. We acknowledge that these classification decisions are based upon and sensitive to the prescribed normal values, while in practice trends across time in these parameters may prove more valuable. Regardless, these normal ranges were carefully derived (i.e., either based on our own in vivo data or credible values reported in the literature). Hence, our results suggest that PWA-derived indices may complement UO in collectively assessing the physiological state in burn patients by accounting for multi-faceted aspects of burn resuscitation. For example, noting that UOP often exhibits delayed response to burn resuscitation, PWA-derived indices may complement UOP by cancelling the delay, and prevent fluid creep.

Translation of the above promising findings to practice may require careful consideration of inter-individual variability in physiological characteristics and resuscitation responses. Most importantly, accurate tracking of the absolute values of CO and SV may require subject-specific calibration (as was done in Fig. 6.4), because each subject is associated with unique normal CO and SV as well as PPV and SPV values. In this regard, the analysis of in vivo data associated with all the animals without subject-specific calibration yielded both promise and potential challenges (Fig. 6.6). Most impressively, physiologically anticipated patterns were preserved, i.e., positive correlation with CO and SV for UO, and negative correlations for the dynamic indices. On the other hand, it is obvious that the degree of correlation is weaker with an increase in data scatter relative to Fig. 6.4, which is largely attributed to the animal-to-animal variability in normal index values and their sensitivity to resuscitation.

The above patterns essentially suggest potential challenges in guiding burn resuscitation using a single index (be it UO or PWA-derived indices) based on its population-based normal range: one-size-fits-all approach may not be efficacious given the large variation in reference CO and SV pertaining to normal UO and PWA-derived index ranges. Conversely, these patterns also suggest opportunities to optimize burn resuscitation. For example, novel ideas to calibrate UO and PWA-derived indices to ground truth CO and SV on a patient-by-patient basis may enable accurate tracking of absolute CO and SV. Personalizing the normal ranges of UO and PWA-derived indices may enhance their utility as biomarkers capable of tracking CO and SV. In addition, UO or PWA-derived indices may be more informative in specific patients depending on comorbidities, pre-existing conditions, etc., highlighting the need for precision

medicine. In this regard, innovative approaches to determine the effectiveness of burn resuscitation based on deep fusion of UO and multiple PWA-derived indices (e.g., via machine learning analytics to aggregate them into a new resuscitation endpoint) may facilitate strict optimization of burn resuscitation, as supported by the findings visualized in Fig. 6.5 (cross-tabulation).

Limitations of the current study include the preclinical nature of the protocol, with a single species and gender accounted for. Still, the complementary nature of UO with PWA-derived indices indicates that both may be used synergistically to inform fluid responsiveness in burn resuscitation.

6.5 Conclusion

This work has advanced the knowledge of the utility of hemodynamic PWA-derived indices in burn resuscitation extremes. Although more evidence needs to be garnered, our results suggest that: PPV, SPV, and SVV can represent CO and SV status during burn resuscitation; these indices can track changes in CO and SV in individual animals, and they may provide multi-faceted perspectives in determining burn resuscitation adequacy and fluid responsiveness. Future work is needed to (i) confirm the findings from this work clinically, (ii) develop novel calibration approaches to personalize the use of PWA-derived indices, and (iii) develop innovative approaches to integrate UO and PWA-derived indices in guiding burn resuscitation.

Chapter 7: Conclusion

When we hear of burn injury treatment, we often immediately think of wound healing. While wound healing is of utmost importance for the patient's quality of life in the future, the first 24-48 hours post-burn is also about keeping the patient alive. Following a chain of inflammatory responses post-burn, significant amounts of plasma shift from the vascular compartment into the tissues, and the blood volume and pressure drop. Standard burn resuscitation protocols aim to replace the lost blood volume with intravenous infusion; however, due to the presence of the inflammatory agents released after the injury, considerable amounts of this fluid leak into the burnt and intact tissue, causing edema. This phenomenon makes burn resuscitation uniquely challenging because edema is not a significant threat in most other forms of shock. Therefore, it is very important to optimize the fluid doses given to the patients using an end-point to guide the resuscitation, so that the hypovolemia is corrected without exacerbating the edema.

Due to the significant variability in treatment efficacy, there is yet to be a consensus over the best course of treatment, or the best end-point to use for titration of fluid doses. Individualizing the burn resuscitation protocols through developing new algorithms and decision support systems is an ongoing effort. In this work, we strived to contribute to this effort by (i) developing a platform for the virtual evaluation of burn resuscitation protocols and (ii) identifying biomarkers to guide fluid resuscitation effectively.

A credible, comprehensive mechanistic model of burn injury and resuscitation could have many benefits, such as (i) serving as a platform for in-silico evaluation of

resuscitation protocols, (ii) providing insight into the burn injury and resuscitation by predicting variables that are not measurable and enhance the knowledge around burn injury, and (iii) be used as a training tool.

Developing new biomarkers to guide burn resuscitation could help determine the status of burn patients and their fluid requirements effectively, by complementing UO and resolving its limitations.

7.1 Summary of Contributions

7.1.1 Mathematical Models

We could summarize the contributions of this work in the following folds:

1) Developing a multi-compartmental model of blood volume kinetics using the concepts introduced by Ampratwum et al. and novel burn perturbation models that could replicate the water and protein dynamics in the vascular compartment, burnt tissues, and intact tissues, after burn injury and resuscitation.
2) Developing two renal function models: (i) a novel phenomenological lumped-parameter model, and (ii) a novel mechanistic renal function model capable of predicting the water and sodium filtration, reabsorption, and excretion rates for both healthy and non-healthy cases. The expanded model includes the intrinsic regulatory mechanisms of the kidney, i.e., the Tubuglomerular feedback, glomerotubular balance, and the myogenic mechanism.
3) Developing a cardiovascular model inspired by the concepts introduced by Guyton and Uttamsingh that has analytical solutions and could be integrated

into the burn model. This is the first validated mathematical model of burn injury and resuscitation that includes both cardiovascular and renal function models, enabling trustworthy evaluation of burn resuscitation protocols and devices with the option to choose the end-points from our validated variables of UO, CO, CVP, MAP, and HCT, which are clinically relevant.

4) Developing a pharmacokinetic pharmacodynamic model for the renin-angiotensin-aldosterone system, adopted from Uttmasingh et al, and updated using recent findings of this hormonal system.
5) Performing the most extensive in-human validation of a mathematical model of burn injury and resuscitation using real clinical data from 233 diverse patients with extensive burn injuries. To the best of our knowledge, our mathematical model may be the first of its kind which is extensively validated for use as a digital twin to replicate realistic burn patients.
6) Conducting a cohort-dependent analysis that showcased how patients that are older, or have inhalation injury, are less responsive to resuscitation compared to younger patients, and patients without inhalation injury, respectively. The model predicted more inflammation and less resuscitation effectiveness for the high-risk groups, suggesting that we should consider the cohort-dependent differences in evaluating and designing new resuscitation protocols. A quality that the current resuscitation protocols are lacking. The model also predicted that in the first 24 hours post-burn, there is no significant difference between male and female patients.

7) Performing an extensive validation for 16 sheep and 15 pig subjects with rich volume kinetics, renal function, cardiovascular system, and electrolyte balance data. Collectively, the prediction accuracy for 11 variables were assessed using collected data: HCT, UO, albumin concentrations in plasma, burnt tissues, and intact tissues, lymphatic flow from burnt and intact tissues, CVP, CO, MAP, and plasma sodium concentration. To the best of our knowledge, our mathematical model may be the first of its kind which is extensively validated for use to replace or complement standard large mammal pre-clinical testing of burn resuscitation protocols.

7.1.2 Biomarkers

In an attempt to advance the knowledge on the utility of hemodynamic PWA-derived indices in burn resuscitation extremes, we:

(1) Observed the longitudinal behavior of pulse pressure variation (PPV), systolic pressure variation (SPV), and stroke volume variation (SVV) for 21 pig subjects with 40% burn injury and showed that these features distinguish different resuscitation paradigms in an interpretable manner.

(2) Showed that PPV, SPV, and SVV track the changes in the cardiac output (CO) and stroke volume (SV) reasonably well. While they perform just as well as UO in tracking CO and SV, their inherent advantage of being available in real-time and their disagreement with UO in determining the subject status suggest that they may provide multi-faceted perspectives in determining burn resuscitation adequacy and fluid responsiveness.

7.2 Limitations and Suggestions for Future work

7.2.1 Mathematical Models

1) Perhaps more significant than all, is the fact that our human dataset only included the urinary output, resuscitation protocols, and demographic data. The training of the model for in-human use could be much strengthened by the addition of more measurements. We have tried to compensate for the lack of other measurements by scrutinizing the predicted variables and comparing them to the literature, where the data is already available.
2) In the cardiovascular model, we do not incorporate a module for heart rate and, thus, stroke volume. Additionally, we do not have distinct compartments for venous blood volume and arterial blood volume dynamics. We, therefore, have estimated the mean systemic filling pressure (which depends on venous volume) using the mean circulatory filling pressure (which depends on total blood volume). While these two variables are shown to be very close and interchangeable in many cases, they are different, especially for very low cardiac output values. We have also considered the CO efficiency constant due to the need for more information.
3) Our cardiovascular model only predicts “static” hemodynamic variables with a relatively large time step (6 minutes). Adding smaller-scale CV models, such as the Windkessel model, could have benefits, such as predicting more cardiovascular variables. More importantly, if we add a respiratory system model, we could predict dynamic indices such as PPV, SPV, and SVV and

enable testing new algorithms that are designed based on these variables. This would connect our modeling and biomarker works and could be a worthy attempt for future work. Additionally, we should note that our CV model is a 0D model, i.e., it is only time-dependent. Incorporating a spatial model that represents distributed properties of the arterial system could enable predicting signals in different parts of the body and allow testing algorithms that rely on the peripheral signals.

4) We don't have an intracellular compartment, and relevant to that, the potassium dynamics in the model. Successful addition of these two components could improve the model, especially the aldosterone and antidiuretic hormone dynamics. We tried adding both of these components to the model, but the intracellular model only added unnecessary complexity without contributing to the goodness of fit. Reliable prediction of the potassium dynamics, on the other hand, was hampered by the fact that potassium is, in general, very unpredictable after burn injury due to the possibility of hyperkalemia.

For sheep and pig subjects, we will conduct a sensitivity and identifiability analysis for the expanded model as part of future work. For human subjects, the cohort-dependent analysis must be repeated for the expanded model, and hypothesis testing, particularly for new modules such as the cardiovascular model, could be performed. Although a lack of measurements hampers the

reliability of predictions for the CV model to confirm the predictions, we could turn to literature to assess the validity of predictions.

7.2.2 Biomarkers

1) In this work, we have only focused on the potential of every index in representing the status and fluid-responsiveness of the subjects on its own. Future work will focus on using innovative machine-learning approaches to integrate the established biomarkers, such as UO, and our PWA-derived biomarkers. The generated algorithm then has to be tested to assess its potential advantages compared to the original methods of guiding fluid resuscitation.
2) In this work, we have used population-derived ranges to determine the status of subjects for both our trend analysis and cross-tabulation. However, as depicted by Fig. 6.6, there is a significant level of inter-subject variability observed for both UO and the dynamic indices, and using an identical threshold for classifying the subjects is far from ideal. Future work is required to develop novel calibration approaches to personalize the use of PWA-derived indices.
3) Beyond the inter-subject variability and the need for calibration, future work could analyze the progression of the measurements and indices in time and unravel its potential contribution to certain observations. For instance, the UO increases and resides at least partially beyond the baseline values for subjects in all three paradigms (Fig. 6.3). Similarly, CO and SV reside within or closer to the normal range in the later phases post-burn for P1 which has not received any resuscitation. This could be due to the long-term volume and pressure

regulation effects of the body, and another indication of the complexity of using these indices to guide resuscitation.

Bibliography

[1] "Burn Incidence Fact Sheet – American Burn Association." [Online]. Available: https://ameriburn.org/who-we-are/media/burn-incidence-fact-sheet/. [Accessed: 29-Nov-2020].

[2] C. B. Nielson, N. C. Duethman, J. M. Howard, M. Moncure, and J. G. Wood, "Burns: Pathophysiology of Systemic Complications and Current Management," *J. Burn Care Res.*, vol. 38, no. 1, pp. e469–e481, 2017.

[3] F. N. Williams *et al.*, "The leading causes of death after burn injury in a single pediatric burn center.," *Crit. Care*, vol. 13, no. 6, p. R183, 2009.

[4] "American Burn Association, National Burn Repository® 2016. Version 12.0., Chicago, IL."

[5] K. D. Capek *et al.*, "Contemporary Burn Survival," *J. Am. Coll. Surg.*, vol. 226, no. 4, pp. 453–463, Apr. 2018.

[6] R. Cartotto and A. Zhou, "Fluid Creep: The Pendulum Hasn't Swung Back Yet!," *J. Burn Care Res.*, vol. 31, no. 4, pp. 551–558, Jul. 2010.

[7] L. Fodor, A. Fodor, Y. Ramon, O. Shoshani, Y. Rissin, and Y. Ullmann, "Controversies in fluid resuscitation for burn management: Literature review and our experience," *Injury*, vol. 37, no. 5, pp. 374–379, 2006.

[8] R. H. Demling, "The Burn Edema Process : Current Concepts," *J. Burn Care Rehabil.*, vol. 26, pp. 207–227, 2005.

[9] B. A. Latenser, "Critical care of the burn patient: The first 48 hours," *Crit. Care Med.*, vol. 37, no. 10, pp. 2819–2826, 2009.

[10] T. J. Schaefer and O. Nunez Lopez, *Burns, Resuscitation And Management*.

StatPearls Publishing, 2019.

[11] D. G. Greenhalgh, “Burn resuscitation: The results of the ISBI/ABA survey,” *Burns*, vol. 36, no. 2, pp. 176–182, Mar. 2010.

[12] A. J. Diver, “The evolution of burn fluid resuscitation,” *International Journal of Surgery*, vol. 6, no. 4. Elsevier, pp. 345–350, 01-Aug-2008.

[13] B. A. J. M. Pruitt, “Protection from Excessive Resuscitation: “Pushing the Pendulum Back",” *J. Trauma*, vol. 49, no. 3, pp. 567–568, 2000.

[14] M. B. Klein *et al.*, “The association between fluid administration and outcome following major burn: A multicenter study,” *Ann. Surg.*, vol. 245, no. 4, pp. 622–628, Apr. 2007.

[15] R. G. Carlson, R. K. Finley, S. F. Miller, L. M. Jones, M. A. Morath, and S. Alkire, “Fluid retention during the first 48 hours as an indicator of burn survival,” *J. Trauma - Inj. Infect. Crit. Care*, vol. 26, no. 9, pp. 840–844, 1986.

[16] R. Cartotto, D. G. Greenhalgh, and C. Cancio, “Burn state of the science: Fluid resuscitation,” *J. Burn Care Res.*, vol. 38, no. 3, pp. e596–e604, 2017.

[17] J. Salinas *et al.*, “Computerized decision support system improves fluid resuscitation following severe burns: An original study,” *Crit. Care Med.*, vol. 39, no. 9, pp. 2031–2038, 2011.

[18] L. C. Cancio, J. Salinas, and G. C. Kramer, “Protocolized Resuscitation of Burn Patients,” *Critical Care Clinics*, vol. 32, no. 4. W.B. Saunders, pp. 599–610, 01-Oct-2016.

[19] F. Pappalardo, G. Russo, F. M. Tshinanu, and M. Viceconti, “In silico clinical trials: concepts and early adoptions,” *Brief. Bioinform.*, vol. 20, no. April 2018,

pp. 1699–1708, 2018.

[20] M. Viceconti, M. Juarez, C. Curreli, M. Pennisi, G. Russo, and F. Pappalardo, "POSITION PAPER: Credibility of In Silico Trial Technologies - A Theoretical Framing.," *IEEE J. Biomed. Heal. informatics*, vol. 24, no. 1, pp. 4–13, 2019.

[21] M. Viceconti, C. Cobelli, T. Haddad, A. Himes, B. Kovatchev, and M. Palmer, "In silico assessment of biomedical products: The conundrum of rare but not so rare events in two case studies," *Proc. Inst. Mech. Eng. Part H J. Eng. Med.*, vol. 231, no. 5, pp. 455–466, 2017.

[22] O. Faris and J. Shuren, "An FDA viewpoint on unique considerations for medical-device clinical trials," *New England Journal of Medicine*, vol. 376, no. 14. Massachussetts Medical Society, pp. 1350–1357, 06-Apr-2017.

[23] G. Huang, R. Reynolds, and C. Candler, "Virtual Patient Simulation at U.S. and Canadian Medical Schools," *Acad. Med.*, vol. 82, no. 5, pp. 446–451, May 2007.

[24] M. Botezatu, H. Hult, M. K. Tessma, and U. G. H. Fors, "Virtual patient simulation for learning and assessment: Superior results in comparison with regular course exams," *Med. Teach.*, vol. 32, no. 10, pp. 845–850, Oct. 2010.

[25] P. Glynn, S. D. Unudurthi, and T. J. Hund, "Mathematical modeling of physiological systems: An essential tool for discovery," *Life Sciences*, vol. 111, no. 1. Elsevier Inc., pp. 1–5, 2014.

[26] A. C. Guyton, "Dominant Role of the Kidneys and Accessory Role of Whole-Body Autoregulation in the Pathogenesis of Hypertension," *Am. J. Hypertens.*,

vol. 2, no. 7, pp. 575–585, Jul. 1989.

[27] G. Arturson, T. Groth, A. Hedlund, and B. Zaar, “Potential use of computer simulation in treatment of burns with special regard to oedema formation,” *Scand. J. Plast. Reconstr. Surg. Hand Surg.*, vol. 18, no. 1, pp. 39–48, 1984.

[28] A. Hedlund, B. Zaar, T. Groth, and G. Arturson, “Computer simulation of fluid resuscitation in trauma. I. Description of an extensive pathophysiological model and its first validation,” *Comput. Methods Programs Biomed.*, vol. 27, no. 1, pp. 7–21, 1988.

[29] G. Arturson, T. Groth, A. Hedlundy, and B. Zaar, “Computer simulation of fluid resuscitation in trauma: First pragmatic validation in thermal injury,” *J. Burn Care Rehabil.*, vol. 10, no. 4, pp. 292–299, 1989.

[30] L. Roa Romero and T. Gomez Cia, “Analysis of the extracellular protein and fluid shifts in burned patients,” *Burns*, vol. 12, no. 5, pp. 337–342, 1986.

[31] L. M. Roa, T. Gomez-Cia, and A. Cantero, “Analysis of burn injury by digital simulation,” *Burns*, vol. 14, no. 3, pp. 201–209, 1988.

[32] L. Roa and T. Gómez-Cia, “A burn patient resuscitation therapy designed by computer simulation (BET). Part 1: simulation studies,” *Burns*, vol. 19, no. 4, pp. 324–331, 1993.

[33] J. L. Bert, B. D. Bowen, R. K. Reed, and R. K. R. Microvascular, “Microvascular exchange and interstitial volume regulation in the rat: model validation.”

[34] J. L. Bert, B. D. Bowen, X. Gu, T. Lund, and R. K. Reed, “Microvascular exchange during burn injury: II. Formulation and validation of a mathematical

model.," *Circ. Shock*, vol. 28, no. 3, pp. 199–219, Jul. 1989.

[35] J. L. Bert, B. D. Bowen, R. K. Reed, and H. Onarheim, "Microvascular exchange during burn injury: IV. Fluid resuscitation model.," *Circ. Shock*, vol. 34, no. 3, pp. 285–97, Jul. 1991.

[36] R. T. Ampratwum, B. D. Bowen, T. Lund, R. K. Reed, and J. L. Bert, "A model of fluid resuscitation following burn injury: formulation and parameter estimation," *Comput. Methods Programs Biomed.*, vol. 47, no. 1, pp. 1–19, 1995.

[37] C. Chapple, B. D. Bowen, R. K. Reed, S. L. Xie, and J. L. Bert, "A model of human microvascular exchange: parameter estimation based on normals and nephrotics," *Comput. Methods Programs Biomed.*, vol. 41, no. 1, pp. 33–54, 1993.

[38] Q. Huang, M. Zhao, and K. Zhao, "Alteration of vascular permeability in burn injury," *Med. Express*, vol. 1, no. 2, pp. 62–76, 2014.

[39] T. Lund, H. Onarheim, and R. K. Reed, "Pathogenesis of edema formation in burn injuries," *World J. Surg.*, vol. 16, no. 1, pp. 2–9, 1992.

[40] G. Arabidarrehdor *et al.*, "Mathematical model of volume kinetics and renal function after burn injury and resuscitation," *Burns*, vol. 47, no. 2, pp. 371–386, Mar. 2021.

[41] G. Arabidarrehdor, A. Tivay, C. Meador, G. C. Kramer, J.-O. Hahn, and J. Salinas, "Mathematical Modeling, In-Human Evaluation, and Analysis of Volume Kinetics and Kidney Function after Burn Injury and Resuscitation," *IEEE Trans. Biomed. Eng.*, pp. 1–1, 2021.

[42] M. A. Swartz, “The physiology of the lymphatic system,” *Advanced Drug Delivery Reviews*. 2001.

[43] G. H. J. Guyton, Arthur C, Taylor A.E, “Dynamics and Control of the Body Fluids,” in *Circulatory Physiology II:*, vol. 2, no. 17, 1985, p. Chapter 9.

[44] E. H. Bresler and L. J. Groome, “On equations for combined convective and diffusive transport of neutral solute across porous membranes.,” *Am. J. Physiol.*, vol. 241, no. 5, pp. F469-76, Nov. 1981.

[45] A. H. Øien and H. Wiig, “Modeling In Vivo Interstitial Hydration-Pressure Relationships in Skin and Skeletal Muscle,” *Biophys. J.*, vol. 115, no. 5, pp. 924–935, 2018.

[46] H. Wiig and M. A. Swartz, “Interstitial fluid and lymph formation and transport: Physiological regulation and roles in inflammation and cancer,” *Physiological Reviews*, vol. 92, no. 3. pp. 1005–1060, 01-Jul-2012.

[47] Guyton and Hall, “The Urinary System: Functional Anatomy and Urine Formation by the Kidneys,” in *Medical Physiology*, .

[48] R. C. Blantz, A. Deng, C. M. Miracle, and S. C. Thomson, “Regulation of kidney function and metabolism: a question of supply and demand.,” *Trans. Am. Clin. Climatol. Assoc.*, vol. 118, pp. 23–43, 2007.

[49] W. R. Chenitz, B. A. Nevins, and N. K. Hollenberg, “Preglomerular resistance and glomerular perfusion in the rat and dog,” *Am. J. Physiol.*, vol. 231, no. 3, pp. 961–966, Sep. 1976.

[50] Guyton and Hall, “Urine Formation by the Kidneys: II. Tubular Reabsorption and Secretion,” in *Textbook of Medical Physiology*, .

[51] F. M. Toates and K. Oatley, “Computer simulation of thirst and water balance,” *Med. Biol. Eng.*, vol. 8, no. 1, pp. 71–87, 1970.

[52] F. M. Toates and K. Oatley, “Control of water-excretion by antidiuretic hormone: Some aspects of modelling the system,” *Med. Biol. Eng. Comput.*, vol. 15, no. 6, pp. 579–588, 1977.

[53] P. J. G. M. Voets and R. P. P. W. M. Maas, “Extracellular volume depletion and resultant hypotonic hyponatremia: A novel translational approach,” *Math. Biosci.*, vol. 295, no. May 2017, pp. 62–66, 2018.

[54] G. Baumann and J. F. Dingman, “Distribution, blood transport, and degradation of antidiuretic hormone in man,” *J. Clin. Invest.*, vol. 57, no. 5, pp. 1109–1116, 1976.

[55] H. HELLER and S. M. ZAIDI, “The metabolism of exogenous and endogenous antidiuretic hormone in the kidney and liver in vivo.,” *Br. J. Pharmacol. Chemother.*, vol. 12, no. 3, pp. 284–292, 1957.

[56] T. Lund, H. Onarheim, H. Wiig, and R. K. Reed, “Mechanisms behind increased dermal imbibition pressure in acute burn edema,” *Am. J. Physiol. - Hear. Circ. Physiol.*, vol. 256, no. 4, 1989.

[57] M. Lehnhardt *et al.*, “A qualitative and quantitative analysis of protein loss in human burn wounds,” *Burns*, vol. 31, no. 2, pp. 159–167, 2005.

[58] T. Lund, H. Wiig, and R. K. Reed, “Acute postburn edema: Role of strongly negative interstitial fluid pressure,” *Am. J. Physiol. - Hear. Circ. Physiol.*, vol. 255, no. 5, 1988.

[59] J. C. Ferguson, C. J. Martin, and C. Rayner, “Burn wound evaporation-

measurement of body fluid loss by probe evaporimeter and weight change," *Clin. Phys. Physiol. Meas.*, vol. 12, no. 2, pp. 143–155, May 1991.

[60] T. Namdar, P. L. Stollwerck, F. H. Stang, F. Siemers, P. Mailänder, and T. Lange, "Transdermal fluid loss in severely burned patients," *GMS Ger. Med. Sci.*, vol. 8, pp. 6–10, 2010.

[61] R. M. Pitt, J. C. Parker, G. J. Jurkovich, A. E. Taylor, and P. W. Curreri, "Analysis of altered capillary pressure and permeability after thermal injury," *J. Surg. Res.*, vol. 42, no. 6, pp. 693–702, 1987.

[62] J. Baudoin, P. Jafari, J. Meuli, L. A. Applegate, and W. Raffoul, "Topical negative pressure on burns: An innovative method for wound exudate collection," *Plast. Reconstr. Surg. - Glob. Open*, vol. 4, no. 11, 2016.

[63] R. X. Xu, X. Sun, and B. S. Weeks, *Burns regenerative medicine and therapy*. Karger, 2004.

[64] F.-R. Curry, C. Michel, E. Renkin, and S. Geiger, "Mechanics and thermodynamics of transcapillary exchange." 01-Jan-1984.

[65] M. Jarzynska and M. Pietruszka, "The application of the Kedem-Katchalsky equations to membrane transport of ethyl alcohol and glucose," *Desalination*, vol. 280, no. 1–3, pp. 14–19, 2011.

[66] G. I. Elgjo, D. L. Traber, H. K. Hawkins, and G. C. Kramer, "Burn resuscitation with two doses of 4 mL/kg hypertonic saline dextran provides sustained fluid sparing: A 48-hour prospective study in conscious sheep," *J. Trauma - Inj. Infect. Crit. Care*, vol. 49, no. 2, pp. 251–265, 2000.

[67] G. C. Kramer, R. A. Gunther, M. L. Nerlich, S. S. Zweifach, and R. H.

Demling, “Effect of dextran-70 on increased microvascular fluid and protein flux after thermal injury.,” *Circ. Shock*, vol. 9, no. 5, pp. 529–41, 1982.

[68] R. G. Hahn, “Volume Kinetics for Infusion Fluids,” *Anesthesiology*, vol. 113, no. 2, pp. 470–481, 2010.

[69] R. Bighamian, A. T. Reisner, and J. Hahn, “A Lumped-Parameter Subject-Specific Model of Blood Volume Response to Fluid Infusion,” *Front. Physiol.*, vol. 7, p. 390, 2016.

[70] B. K. Kataria *et al.*, “The Pharmacokinetics of Propofol in Children using Three Different Data Analysis Approaches,” *Anesthesiology*, vol. 80, pp. 104–122, 1994.

[71] A. Tivay, G. Arabi, D. Dor, R. Bighamian, G. C. Kramer, and J.-O. Hahn, “A Regularized System Identification Approach to Subject-Specific Physiological Modeling with Limited Data,” in *Proceedings of 2019 American Control Conference*, 2019, pp. 3468–3473.

[72] A. Tivay, X. Jin, A. Lo, C. G. Scully, and J.-O. Hahn, “Practical Use of Regularization in Individualizing a Mathematical Model of Cardiovascular Hemodynamics Using Scarce Data,” *Front. Physiol.*, 2020.

[73] Q. Luo *et al.*, “Modeling fluid resuscitation by formulating infusion rate and urine output in severe thermal burn adult patients: A retrospective cohort study,” *Biomed Res. Int.*, vol. 2015, 2015.

[74] V. K. Tiwari, “Burn wound: How it differs from other wounds,” *Indian Journal of Plastic Surgery*, vol. 45, no. 2. pp. 364–373, May-2012.

[75] and D. N. H. Kramer, George C., T. Lund, “Pathophysiology of burn shock

and burn edema.," in *Total Burn Care*, 2012, pp. 103–13.

[76] H. J. Zdolsek, B. Kågedal, B. Lisander, and R. G. Hahn, "Glomerular filtration rate is increased in burn patients," *Burns*, vol. 36, no. 8, pp. 1271–1276, Dec. 2010.

[77] M. B. Klein *et al.*, "The association between fluid administration and outcome following major burn: A multicenter study," *Ann. Surg.*, vol. 245, no. 4, pp. 622–628, Apr. 2007.

[78] M. E. Habib *et al.*, "Does Ringer Lactate Used in Parkland Formula for Burn Resuscitation Adequately Restore Body Electrolytes and Proteins?," *Mod. Plast. Surg.*, vol. 07, no. 01, pp. 1–12, Jan. 2017.

[79] S. L. Xie, R. K. Reed, B. D. Bowen, and J. L. Bert, "A Model of Human Microvascular Exchange," *Microvascular Research*, vol. 49, no. 2. pp. 141–162, 1995.

[80] D. J. Gillett and D. F. J. Halmagyi, "Results and limitations of blood volume measurements in sheep," *J. Surg. Res.*, vol. 6, no. 5, pp. 211–214, May 1966.

[81] J. P. Coghlan, J. S. Fan, B. A. Scoggins, and A. A. Shulkes, "Measurement of extracellular fluid volume and blood volume in sheep.," *Aust. J. Biol. Sci.*, vol. 30, no. 1–2, pp. 71–84, Apr. 1977.

[82] G. C. Kramer, B. A. Harms, R. A. Gunther, E. M. Renkin, and R. H. Demling, "The Effects of Hypoproteinemia on Blood-to-Lymph Fluid Transport in Sheep Lung," 1981.

[83] Guyton and Hall, "Urine Formation by the Kidneys: I. Glomerular Filtration, Renal Blood Flow, and Their Control," in *Medical Physiology*, .

[84] M. Nesje, A. Flåøyen, and L. Moe, “Estimation of glomerular filtration rate in normal sheep by the disappearance of iohexol from serum,” *Vet. Res. Commun.*, vol. 21, no. 1, pp. 29–35, 1997.

[85] Guyton and Hall, “The Body Fluid Compartments: Extracellular and Intracellular Fluids; Edem,” in *Medical Physiology*, .

[86] J. W. Bennett, “Regional body surface area of sheep,” *J. agric. Sci., Camb*, vol. 81, pp. 429–432, 2020.

[87] L. Kongstad, A. D. Möller, and P. O. Grände, “Reflection coefficient for albumin and capillary fluid permeability in cat calf muscle after traumatic injury,” *Acta Physiol. Scand.*, vol. 165, no. 4, pp. 369–377, Apr. 1999.

[88] M. J. Muller, S. P. Pegg, and M. R. Rule, “Determinants of death following burn injury,” *Br. J. Surg.*, vol. 88, no. 4, pp. 583–587, 2001.

[89] R. L. George *et al.*, “The association between sex and mortality among burn patients as modified by age,” *J. Burn Care Rehabil.*, vol. 26, no. 5, pp. 416–421, 2005.

[90] G. McGwin, R. L. George, J. M. Cross, D. A. Reiff, I. H. Chaudry, and L. W. Rue, “Gender differences in mortality following burn injury,” *Shock*, vol. 18, no. 4, pp. 311–315, 2002.

[91] G. E. O’Keefe, J. L. Hunt, and G. F. Purdue, “An evaluation of risk factors for mortality after burn trauma and the identification of gender-dependent differences in outcomes,” *J. Am. Coll. Surg.*, vol. 192, no. 2, pp. 153–160, 2001.

[92] J. Salinas, M. Serio-Melvin, C. Fenrich, K. Chung, G. Kramer, and L. Cancio,

"225," *Crit. Care Med.*, vol. 40, pp. 1–328, Dec. 2012.

[93] D. L. McGee, "Weight-height relationships and body mass index: Some observations from the diverse populations collaboration," *Am. J. Phys. Anthropol.*, vol. 128, no. 1, pp. 220–229, Sep. 2005.

[94] S. Meshulam-Derazon, S. Nachumovsky, D. Ad-El, J. Sulkes, and D. J. Hauben, "Prediction of morbidity and mortality on admission to a burn unit," *Plast. Reconstr. Surg.*, vol. 118, no. 1, pp. 116–120, Jul. 2006.

[95] R. E. Barrow, M. G. Jeschke, and D. N. Herndon, "Early fluid resuscitation improves outcomes in severely burned children," *Resuscitation*, vol. 45, no. 2, pp. 91–96, 2000.

[96] P. Wurzer, D. Culnan, L. C. Cancio, and G. C. Kramer, "Pathophysiology of burn shock and burn edema," in *Total Burn Care: Fifth Edition*, Elsevier Inc., 2018, pp. 66-76.e3.

[97] I. Kaddoura, G. Abu-Sittah, A. Ibrahim, R. Karamanoukian, and N. Papazian, "Burn injury: review of pathophysiology and therapeutic modalities in major burns.," *Ann. Burns Fire Disasters*, vol. 30, no. 2, pp. 95–102, Jun. 2017.

[98] G. D. Warden, "Fluid resuscitation and early management," in *Total Burn Care*, 4th ed., Elsevier (2012), pp. 115–124.

[99] B. H. BOWSER-WALLACE, J. B. CONE, and F. T. CALDWELL, "Hypertonic Lactated Saline Resuscitation of Severely Burned Patients Over 60 Years of Age," *J. Trauma Inj. Infect. Crit. Care*, vol. 25, no. 1, pp. 22–26, Jan. 1985.

[100] N. T. Dai *et al.*, "The comparison of early fluid therapy in extensive flame

burns between inhalation and noninhalation injuries," *Burns*, vol. 24, no. 7, pp. 671–675, 1998.

[101] M. Rani and M. G. Schwacha, "Aging and the pathogenic response to burn," *Aging Dis.*, vol. 3, no. 2, pp. 171–180, 2012.

[102] R. Oakley and B. Tharakan, "Vascular hyperpermeability and aging," *Aging Dis.*, vol. 5, no. 2, pp. 114–125, 2014.

[103] J. A. Farina, M. J. Rosique, and R. G. Rosique, "Curbing inflammation in burn patients," *Int. J. Inflam.*, vol. 2013, 2013.

[104] R. H. Demling, "Smoke inhalation lung injury: an update.," *Eplasty*, vol. 8, p. e27, May 2008.

[105] S. Rehou, S. Shahrokhi, J. Thai, M. Stanojcic, and M. G. Jeschke, "Acute Phase Response in Critically Ill Elderly Burn Patients," *Crit. Care Med.*, vol. 47, no. 2, pp. 201–209, Feb. 2019.

[106] M. S. Gregory, D. E. Faunce, L. A. Duffner, and E. J. Kovacs, "Gender difference in cell-mediated immunity after thermal injury is mediated, in part, by elevated levels of interleukin-6," *J. Leukoc. Biol.*, vol. 67, no. 3, pp. 319–326, 2000.

[107] J. D. Hoppe, P. C. Scriba, and H. Klüter, "Transfusion Medicine and Hemotherapy - Chapter 5. Human Albumin," in *Transfusion medicine and hemotherapy : offizielles Organ der Deutschen Gesellschaft fur Transfusionsmedizin und Immunhamatologie*, vol. 36, no. 6, Karger Publishers, 2009, pp. 399–407.

[108] M. Ellmerer *et al.*, "Measurement of interstitial albumin in human skeletal

muscle and adipose tissue by open-flow microperfusion," *Am. J. Physiol. - Endocrinol. Metab.*, vol. 278, no. 2 41-2, 2000.

[109] A. C. Guyton, A. E. Taylor, and H. J. Granger, "Dynamics and control of the body fluids, chapter 9-11," in *Circulatory physiology*, no. 2, Saunders, 1975, pp. vii, 397 p.

[110] J. Hall and A. Guyton, "Cardiac Failure," in *Textbook of Medical Physiology*, p. 276.

[111] J. Hall and A. Guyton, "Urine Formation by the Kidneys: I. Glomerular Filtration, Renal Blood Flow, and Their Control," in *Textbook of Medical Physiology*, .

[112] A. C. Gordon and J. A. Russell, "Should Vasopressin Be Used in Septic Shock?," in *Evidence-Based Practice of Critical Care*, Elsevier Inc., 2011, pp. 212–217.

[113] L. Meng, W. Hou, J. Chui, R. Han, and A. W. Gelb, "Cardiac Output and Cerebral Blood FlowThe Integrated Regulation of Brain Perfusion in Adult Humans," *Anesthesiology*, vol. 123, no. 5, pp. 1198–1208, Nov. 2015.

[114] A. Hasanin, A. Mukhtar, and H. Nassar, "Perfusion indices revisited," *J. Intensive Care*, vol. 5, no. 1, pp. 1–8, Mar. 2017.

[115] E. A. Carr, "Shock: Pathophysiology, Diagnosis, Treatment, and Physiologic Response to Trauma," in *Equine Surgery*, 4th ed., W.B. Saunders, 2012, pp. 1–13.

[116] J. D. Paratz *et al.*, "Burn resuscitation--hourly urine output versus alternative endpoints: a systematic review," *Shock*, vol. 42, no. 4, pp. 295–306, 2014.

[117] D. J. Dries and K. Waxman, “Adequate resuscitation of burn patients may not be measured by urine output and vital signs,” *Crit. Care Med.*, vol. 19, no. 3, pp. 327–329, 1991.

[118] D. M. Caruso and M. R. Matthews, “Monitoring End Points of Burn Resuscitation,” *Crit. Care Clin.*, vol. 32, no. 4, pp. 525–537, Oct. 2016.

[119] A. Quarteroni, “Modeling the Cardiovascular System: A Mathematical Challenge,” *Math. Unltd. — 2001 Beyond*, pp. 961–970, 2001.

[120] A. Quarteroni, A. Manzoni, and C. Vergara, “The cardiovascular system: Mathematical modelling, numerical algorithms and clinical applications*,” *Acta Numer.*, vol. 26, pp. 365–590, May 2017.

[121] F. Kappel and R. O. Peer, “Mathematical Biology A mathematical model for fundamental regulation processes in the cardiovascular system,” 1993.

[122] M. Abdolrazaghi, M. Navidbakhsh, and K. Hassani, “Mathematical Modelling and Electrical Analog Equivalent of the Human Cardiovascular System.”

[123] L. D’Orsi *et al.*, “A mathematical model of cardiovascular dynamics for the diagnosis and prognosis of hemorrhagic shock,” *Math. Med. Biol. A J. IMA*, vol. 38, no. 4, pp. 417–441, Dec. 2021.

[124] Y. V Kislova, A. V Bogomolov, and N. V Soloshenko, “Mathematical Modeling of Cardiovascular System in Patients with Hemorrhage and Hypothermia,” *Biomed. Eng. (NY).*, vol. 40, no. 4, p. 1013, 2006.

[125] A. S. Karavaev *et al.*, “Model of human cardiovascular system with a loop of autonomic regulation of the mean arterial pressure,” *J. Am. Soc. Hypertens.*, vol. 10, no. 3, pp. 235–243, Mar. 2016.

[126] S. Bozkurtid, “Mathematical modeling of cardiac function to evaluate clinical cases in adults and children,” 2019.

[127] R. J. Uttamsingh, M. S. Leaning, J. A. Bushman, E. R. Carson, and L. Finkelstein, “Mathematical model of the human renal system,” *Med. Biol. Eng. Comput.*, vol. 23, no. 6, pp. 525–535, 1985.

[128] A. C. Guyton, “Effect of blood volume, mean circulatory filling pressure, cardiac output, and autoregulation on arterial pressure,” in *Circulatory Physiology III Arterial Pressure and Hypertension*, Saunders W B Co, 1982, pp. 71–86.

[129] T. Q. RICHARDSON, J. O. STALLINGS, and A. C. GUYTON, “Pressure-volume curves in live, intact dogs,” *Am. J. Physiol.*, vol. 201, pp. 471–474, Sep. 1961.

[130] R. W. Lee, L. D. Lancaster, R. G. Gay, M. Paquin, and S. Goldman, “Use of acetylcholine to measure total vascular pressure-volume relationship in dogs,” *https://doi.org/10.1152/ajpheart.1988.254.1.H115*, vol. 254, no. 1, 1988.

[131] O. W, B. JJ, F. R, L. AF, M. JJ, and R. JI, “Sensitization of the adrenal cortex to angiotensin II in sodium-deplete man,” *Circ. Res.*, vol. 34, no. 1, pp. 69–77, Apr. 1974.

[132] A. C. Guyton, A. W. Lindsey, B. Abernathy, T. Richardson, and uf Ptbyriulogy, “Venous Return at Various Right Atria1 Pressures and the Normal Venous Return Curve’ School of &fed ihe, ABSTRACT.”

[133] K. Sunagawa, “Guyton’s venous return curves should be taught at medical schools (complete English translation of Japanese version),” *J. Physiol. Sci.*,

vol. 67, no. 4, pp. 447–458, Jul. 2017.

[134] A. C. GUYTON, “Determination of cardiac output by equating venous return curves with cardiac response curves,” *Physiol. Rev.*, vol. 35, no. 1, pp. 123–129, Jan. 1955.

[135] A. C. GUYTON, A. W. LINDSEY, B. ABERNATHY, and J. B. LANGSTON, “Mechanism of the increased venous return and cardiac output caused by epinephrine,” *Am. J. Physiol.*, vol. 192, no. 1, pp. 126–130, Jan. 1958.

[136] Y. A. Kara and Y. A. Kara, “Burn Etiology and Pathogenesis,” *Hot Top. Burn Inj.*, May 2018.

[137] S. Soussi, F. Dépret, M. Benyamina, and M. Legrand, “Early hemodynamic management of critically Ill burn patients,” *Anesthesiology*, vol. 129, no. 3, pp. 583–589, 2018.

[138] F. R. E. Curry and R. H. Adamson, “Vascular permeability modulation at the cell, microvessel, or whole organ level: towards closing gaps in our knowledge,” *Cardiovasc. Res.*, vol. 87, no. 2, pp. 218–229, Jul. 2010.

[139] B. J. Czerwin, S. Patel, C. M. Chiofolo, J. Yuan, and N. W. Chbat, “Modeling the Steady-State Effects of Mean Arterial Pressure on the Kidneys,” *IEEE Open J. Eng. Med. Biol.*, vol. 2, 2021.

[140] L. C. Moore, A. Rich, and D. Casellas, “Ascending myogenic autoregulation: interactions between tubuloglomerular feedback and myogenic mechanisms,” *Bull. Math. Biol.*, vol. 56, no. 3, pp. 391–410, May 1994.

[141] R. Moss and S. R. Thomas, “Hormonal regulation of salt and water excretion: A mathematical model of whole kidney function and pressure natriuresis,” *Am.*

J. Physiol. - Ren. Physiol., vol. 306, no. 2, pp. 183–185, 2014.

[142] B. M. Brenner, J. L. Troy, T. M. Daugharty, W. M. Deen, and C. R. Robertson, "Dynamics of glomerular ultrafiltration in the rat. II. Plasma-flow dependence of GFR," *https://doi.org/10.1152/ajplegacy.1972.223.5.1184*, vol. 223, no. 5, pp. 1184–1190, 1972.

[143] W. M. Deen, C. R. Robertson, and B. M. Brenner, "A model of glomerular ultrafiltration in the rat," *Am. J. Physiol.*, vol. 223, no. 5, pp. 1178–1183, 1972.

[144] B. M. Brenner, J. L. Troy, and T. M. Daugharty, "The Dynamics of Glomerular Ultrafiltration in the Rat," *J. Clin. Invest.*, vol. 50, no. 8, p. 1776, 1971.

[145] D. W. Good, "Nongenomic actions of aldosterone on the renal tubule," *Hypertension*, vol. 49, no. 4, pp. 728–739, Apr. 2007.

[146] S. A. Salyer *et al.*, "Aldosterone regulates Na+, K+ ATPase activity in human renal proximal tubule cells through mineralocorticoid receptor," *Biochim. Biophys. Acta - Mol. Cell Res.*, vol. 1833, no. 10, pp. 2143–2152, Oct. 2013.

[147] A. C. Guyton, "Role of Aldosterone in Fluid Volume and Electrolyte Control," in *Dynamics and Control of the Body Fluids, Circulatory Physiology II*, W.B. Saunders Company, 1975, p. 291.

[148] A. T. Layton and H. E. Layton, "A computational model of epithelial solute and water transport along a human nephron," *PLoS Comput. Biol.*, vol. 15, no. 2, Feb. 2019.

[149] A. Kurtz, "Control of renin synthesis and secretion," *Am. J. Hypertens.*, vol. 25, no. 8, pp. 839–847, Aug. 2012.

[150] K. M. Denton, W. P. Anderson, and R. Sinniah, “Effects of angiotensin II on regional afferent and efferent arteriole dimensions and the glomerular pole,” *Am. J. Physiol. - Regul. Integr. Comp. Physiol.*, vol. 279, no. 2 48-2, 2000.

[151] J. Bohlender, J. Ménard, D. Ganten, and F. C. Luft, “Angiotensinogen Concentrations and Renin Clearance,” *Hypertension*, vol. 35, no. 3, pp. 780–786, 2000.

[152] E. G. Schneider, H. H. Rostorfer, and F. D. Nash, “Distribution volume and metabolic clearance rate of renin in anesthetized nephrectomized dogs,” *https://doi.org/10.1152/ajplegacy.1968.215.5.1115*, vol. 215, no. 5, pp. 1115–1122, 1968.

[153] J. R. BLAIR-WEST *et al.*, “Humoral stimulation of adrenal cortical secretion,” *J. Clin. Invest.*, vol. 41, no. 8, pp. 1606–1627, 1962.

[154] E. M. Walters and R. S. Prather, “Advancing Swine Models for Human Health and Diseases,” *Mo. Med.*, vol. 110, no. 3, p. 212, 2013.

[155] A. Banstola and J. N. J. Reynolds, “The Sheep as a Large Animal Model for the Investigation and Treatment of Human Disorders,” *Biol. 2022, Vol. 11, Page 1251*, vol. 11, no. 9, p. 1251, Aug. 2022.

[156] J. Oda *et al.*, “Resuscitation fluid volume and abdominal compartment syndrome in patients with major burns,” *Burns*, vol. 32, no. 2, pp. 151–154, Mar. 2006.

[157] G. ArabiDarrehDor *et al.*, “The Potential of Arterial Pulse Wave Analysis in Burn Resuscitation: A Pilot In Vivo Study,” *J. Burn Care Res.*, Jul. 2022.

[158] J. King and D. R. Lowery, “Physiology, Cardiac Output,” *StatPearls*, Jul.

2022.

[159] P. Shah and M. Louis, “Physiology, Central Venous Pressure - PubMed.” [Online]. Available: https://pubmed.ncbi.nlm.nih.gov/30137777/. [Accessed: 25-Oct-2022].

[160] L. M. Davenport, G. P. Dobson, and H. L. Letson, “The role of invasive monitoring in the resuscitation of major burns: a systematic review and meta-analysis,” *Int. J. Burns Trauma*, vol. 9, no. 2, p. 28, 2019.

[161] Y. Peeters, M. Lebeer, R. Wise, and M. L. N. G. Malbrain, “An overview on fluid resuscitation and resuscitation endpoints in burns: Past, present and future. Part 2 - avoiding complications by using the right endpoints with a new personalized protocolized approach,” *Anaesthesiol. Intensive Ther.*, vol. 47 Spec No, no. 1, pp. s15–s26, Mar. 2015.

[162] P. Romagnani *et al.*, “Chronic kidney disease,” *Nat. Rev. Dis. Prim.*, vol. 3, Nov. 2017.

[163] S. S. Emara and A. A. Alzaylai, “Renal failure in burn patIents: A review,” *Annals of Burns and Fire Disasters*, vol. 26, no. 1. Euro-Mediterranean Council for Burns and Fire Disasters (MBC), pp. 12–15, 2013.

[164] K. M. Harper, D. J. Knapp, H. E. Criswell, and G. R. Breese, “Vasopressin and alcohol: A multifaceted relationship,” *Psychopharmacology (Berl).*, vol. 235, no. 12, p. 3363, Dec. 2018.

[165] M. J. L. J. Van Den Elsen, L. P. H. Leenen, and J. Kesecioglu, “Hemodynamic support of the trauma patient,” *Curr. Opin. Anaesthesiol.*, vol. 23, no. 2, pp. 269–275, Apr. 2010.

[166] J. Gillenwater and W. Garner, “Acute Fluid Management of Large Burns: Pathophysiology, Monitoring, and Resuscitation,” *Clin. Plast. Surg.*, vol. 44, no. 3, pp. 495–503, Jul. 2017.

[167] S. D. Hallisey and J. C. Greenwood, “Beyond Mean Arterial Pressure and Lactate: Perfusion End Points for Managing the Shocked Patient,” *Emerg. Med. Clin. North Am.*, vol. 37, no. 3, pp. 395–408, Aug. 2019.

[168] J. C. Greenwood and C. J. Orloski, “End Points of Sepsis Resuscitation,” *Emerg. Med. Clin. North Am.*, vol. 35, no. 1, pp. 93–107, Feb. 2017.

[169] M. Tokarik, F. Sjöberg, M. Balik, I. Pafcuga, and L. Broz, “Fluid Therapy LiDCO Controlled Trial—Optimization of Volume Resuscitation of Extensively Burned Patients through Noninvasive Continuous Real-Time Hemodynamic Monitoring LiDCO,” *J. Burn Care Res.*, vol. 34, no. 5, pp. 537–542, Sep. 2013.

[170] C. Gong *et al.*, “The Variation of Hemodynamic Parameters Through PiCCO in the Early Stage After Severe Burns,” *J. Burn Care Res.*, vol. 38, no. 6, pp. e966–e972, Nov. 2017.

[171] Y. Zhu, M. Yang, L. Ding, G. Chu, J. Cheng, and G. Lv, “Fluid resuscitation based on pulse contour cardiac output monitoring is associated with improved prognosis in adult severe burn patients: a retrospective cohort study,” *Ann. Palliat. Med.*, vol. 10, no. 10, pp. 10904–10912, Jan. 2021.

[172] J. M. Causbie, L. A. Sattler, A. P. Basel, G. W. Britton, and L. C. Cancio, “State of the Art: An Update on Adult Burn Resuscitation,” *Eur. Burn J. 2021, Vol. 2, Pages 152-167*, vol. 2, no. 3, pp. 152–167, Sep. 2021.

[173] A. L. Holder, G. Clermont, and M. R. Pinsky, “Early Identification of Occult Bleeding Through Hypovolemia Detection,” *Annu. Updat. Intensive Care Emerg. Med. 2014*, pp. 555–567, 2014.

[174] B. Tavernier, O. Makhotine, G. Lebuffe, J. Dupont, and P. Scherpereel, “Systolic Pressure Variation as a Guide to Fluid Therapy in Patients with Sepsis-induced Hypotension,” *Anesthesiology*, vol. 89, no. 6, pp. 1313–1321, Dec. 1998.

[175] F. Michard *et al.*, “Relation between respiratory changes in arterial pulse pressure and fluid responsiveness in septic patients with acute circulatory failure,” *Am. J. Respir. Crit. Care Med.*, vol. 162, no. 1, pp. 134–138, 2000.

[176] A. Perel, R. Pizov, and S. Cotev, “Systolic blood pressure variation is a sensitive indicator of hypovolemia in ventilated dogs subjected to graded hemorrhage,” *Anesthesiology*, vol. 67, no. 4, pp. 498–502, 1987.

[177] Q. Li, R. G. Mark, and G. D. Clifford, “Artificial arterial blood pressure artifact models and an evaluation of a robust blood pressure and heart rate estimator,” *Biomed. Eng. Online*, vol. 8, Jul. 2009.

[178] F. Cavallaro, C. Sandroni, and M. Antonelli, “Functional hemodynamic monitoring and dynamic indices of fluid responsiveness.,” *Minerva Anestesiol.*, vol. 74, no. 4, pp. 123–35, Apr. 2008.

[179] H. Sano *et al.*, “Evaluation of pulse pressure variation and pleth variability index to predict fluid responsiveness in mechanically ventilated isoflurane-anesthetized dogs,” *J. Vet. Emerg. Crit. Care*, vol. 28, no. 4, pp. 301–309, Jul. 2018.

[180] D. Jacques, K. Bendjelid, S. Duperret, J. Colling, V. Piriou, and J. P. Viale, "Pulse pressure variation and stroke volume variation during increased intra-abdominal pressure: an experimental study," *Crit. Care*, vol. 15, no. 1, Jan. 2011.

[181] M. K. Dahl, S. T. Vistisen, J. Koefoed-Nielsen, and A. Larsson, "Using an expiratory resistor, arterial pulse pressure variations predict fluid responsiveness during spontaneous breathing: An experimental porcine study," *Crit. Care*, vol. 13, no. 2, pp. 1–9, Mar. 2009.

[182] M. Cannesson *et al.*, "Assessing the Diagnostic Accuracy of Pulse Pressure Variations for the Prediction of Fluid ResponsivenessA 'Gray Zone' Approach," *Anesthesiology*, vol. 115, no. 2, pp. 231–241, Aug. 2011.

[183] M. R. Mathis *et al.*, "Arterial Pressure Variation in Elective Non-cardiac Surgery: Identifying Reference Distributions and Modifying Factors," *Anesthesiology*, vol. 126, no. 2, p. 249, Feb. 2017.

[184] A. J. Singer and S. A. McClain, "A porcine burn model," *Methods Mol. Med.*, vol. 78, pp. 107–120, Nov. 2003.

[185] B. I. Gómez, M. A. Dubick, E. P. Schmidt, J. W. Shupp, D. M. Burmeister, and D. Burmeister, "Plasma and Urinary Glycosaminoglycans as Evidence for Endotheliopathy in a Swine Burn Model Short Title: Glycocalyx Shedding Markers After Burns," 2019.

[186] D. M. Burmeister *et al.*, "Impact of Isolated Burns on Major Organs: A Large Animal Model Characterized," *Shock*, vol. 46, no. 3 Suppl 1, pp. 137–147, Sep. 2016.